2014

Experimental Realization of Slowly Rotating Modes of Light

Fangzhao A. An
Harvey Mudd College

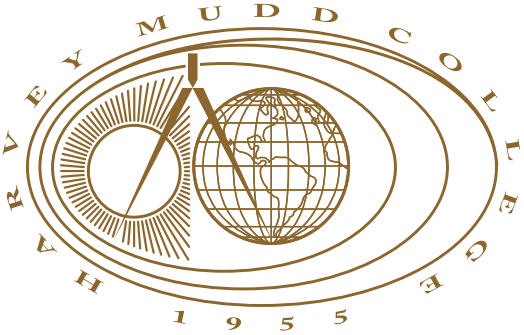

Experimental Realization of Slowly Rotating Modes of Light

Fangzhao Alex An

Theresa Lynn, Advisor

May, 2014

Department of Physics

Abstract

Beams of light can carry spin and orbital angular momentum. Spin angular momentum describes how the direction of the electric field rotates about the propagation axis, while orbital angular momentum describes the rotation of the field amplitude pattern. These concepts are well understood for monochromatic beams, but previous theoretical studies have constructed polychromatic superpositions where the connection between angular momentum and rotation of the electric field becomes much less clear. These states are superpositions of two states of light carrying opposite signs of angular momentum and slightly detuned frequencies. They rotate at the typically small detuning frequency and thus we call them slowly rotating modes of light. Strangely, some of these modes appear to rotate in the direction opposing the sign of their angular momentum, while others exhibit overall rotation with no angular momentum at all! These findings have been the subject of some controversy, and in 2012, Susanna Todaro (HMC '12) and I began work on trying to shed light on this "angular momentum paradox." In this thesis, I extend previous work in theory, simulation, and experiment. Via theory and modeling in Mathematica, I present a possible intuitive explanation for the angular momentum paradox. I also present experimental realization of slowly rotating spin superpositions, and outline the steps necessary to generate slowly rotating orbital angular momentum superpositions.

Contents

List of Figures

List of Tables

Acknowledgments

I would like to thank my parents for their love, help, and support. I would also like to thank my advisor, Professor Theresa Lynn, for several years of guidance. Professors John Townsend, Richard Haskell, and Peter Saeta have also been a great help, in addition to all of the other wonderful faculty members of the physics department. Finally, I would like to thank all of my friends, colleagues, and teachers here at Harvey Mudd for making these past four years the toughest and most enjoyable time of my life.

Chapter 1

Introduction

As with objects in classical mechanics, beams of light can carry spin angular momentum and orbital angular momentum. Spin angular momentum corresponds to rotation of the polarization vector about the propagation axis while orbital angular momentum corresponds to rotation of the intensity pattern of the beam. Both of these have been well studied in quantum optics applications. Superpositions of these states have also been studied. An equal superposition of states with opposite angular momenta produces no rotation, as the opposite components cancel.

What we do not fully understand, though, is the behavior of superpositions of angular momentum states with slightly detuned frequencies. In 2007, van Enk and Nienhuis published a paper constructing specific superpositions of two angular momentum states of light carrying opposite signs of angular momentum and slightly detuned frequencies. [1] The positive angular momentum state is frequency shifted up and the negative angular momentum state is frequency shifted down. When their slow rotation was modeled, these states exhibited rotation that did not appear to correspond to their angular momenta. Some of these states carry angular momentum with sign that matches the direction of their rotation, while others carry angular momentum with sign that opposes the direction of their rotation. Other states even exhibit overall rotation with zero angular momentum. These counterintuitive results have generated some controversy, and have led some to call this an "angular momentum paradox." [2]

This paradox challenges our conventional understanding of angular momentum of light. If the calculated angular momentum predicts rotation in one direction, why does the state rotate in an oppose manner? Why do some states rotate with zero angular momentum? We know angular mo-

mentum for monochromatic beams of light, but does or should this knowledge carry over to exotic polychromatic beams of light like these slowly rotating modes? Addressing questions like these will aid us in piecing together a more complete and thorough understanding of the angular momentum of light.

In this thesis, I follow up on the thesis work done by Susanna Todaro (HMC '12) [3], itself an extension of the work by Van Enk and Nienhuis. [1] In Chapter 2, I introduce the concepts of spin and orbital angular momentum of light, applied to monochromatic beams of light. I also simulate the real electric fields of these monochromatic, angular momentum carrying beams of light, introducing both mathematics and simulations that are a theme throughout this work.

From monochromatic beams, I move on to Chapter 3 where I introduce the polychromatic slowly rotating modes used by van Enk and Nienhuis. I will define them in ket notation, and calculate the angular momenta that each mode carries. To investigate the angular momentum paradox, we then calculate the real electric field of the modes. I simulate and plot these expressions for real electric field in Chapter 4, describing their rotational behavior. I compare their rotation to their angular momenta, and using the simulations, I provide possible explanations of the angular momentum paradox for some modes.

In Chapter 5, I detail how I experimentally generate and measure the spin equal superpositions. I describe past experimental hurdles and how I have overcome them. I present experimental results showing the rotation of the spin equal superpositions, and describe strange behavior in the amplitude of the data as a function of frequency. In Chapter 6, I describe the orbital angular momentum analog to this experimental work on the spin states. I provide several options to generate the incident beam necessary to create the slowly rotating orbital angular momentum modes, describe how the slowly rotating modes can be generated, and present a viable detection apparatus.

I conclude in Chapter 7 by summarizing my work and presenting future avenues of research.

Chapter 2

Angular Momentum of Light

To understand polychromatic, slowly rotating modes of light, we must first understand the concepts of spin and orbital angular momentum for monochromatic light and how they correspond to rotation. This will allow us to explore the specific superpositions of light that exhibit strange and unintuitive relations between their angular momentum and their rotation.

In classical mechanics, angular momentum is a measure of the physical rotation of an object about some axis. Similarly, the angular momentum of light is a measure of the rotation of some aspect of the $\vec{E}$ and $\vec{B}$ fields. When referring to optical angular momentum, we can consider the angular momentum of individual photons or the angular momentum carried by an entire beam of light like that output from a laser. In this thesis, we mainly deal with beams of light yet it is often helpful to consider the more fundamental angular momenta of photons.

2.1 Spin Angular Momentum of Light

In the case of spin angular momentum of a beam of light, the electric field direction or polarization vector rotates about the axis of propagation. The eigenvalue equation is expressed as

$$\hat{S}_z|s\rangle = s\hbar|s\rangle \tag{2.1}$$

where the spin angular momentum operator $\hat{S}_z$ acts on eigenstates $|s\rangle$ to produce the angular momentum eigenvalue $s\hbar$. The spin angular momentum quantum number s can take on the values of ± 1 with corresponding eigenstates $|R\rangle$ and $|L\rangle$, or right and left circularly polarized light. These

can be written as superpositions of linear polarization states $|H\rangle$ and $|V\rangle$,

$$|R\rangle \equiv |s=1\rangle \quad = \frac{1}{\sqrt{2}}|H\rangle + \frac{i}{\sqrt{2}}|V\rangle \tag{2.2}$$

$$|L\rangle \equiv |s=-1\rangle = \frac{1}{\sqrt{2}}|H\rangle - \frac{i}{\sqrt{2}}|V\rangle \tag{2.3}$$

where following the convention used in Townsend [4], we have defined these states from the point of view of the source.[1] Figure 2.1 shows a right circularly polarized beam of light propagating to the right along the positive z axis. The polarization vector may appear to rotate left-handedly as it moves down the z axis (traced by the solid red line), but in considering the handedness of the beam, we are concerned with the time evolution of the polarization. Taking a transverse slice of the electric field at the plane of the x-y axes, we note that the polarization vector must be rotating right-handedly to produce this overall shape.

This discussion has shown that it is useful to reformulate these kets as polarization vectors of the electric field. To do this, we introduce the complex electric field $\vec{E}$ of an electromagnetic wave propagating along the z axis,

$$\vec{E}(r,\phi,z,t) = E(r,\phi,z)e^{-i\omega t}\vec{e}_s. \tag{2.4}$$

Here, s and ℓ are the spin and orbital angular momentum quantum numbers, ω is the angular frequency, (r,ϕ,z) are standard cylindrical coordinates, and $E(r,\phi,z)$ is the complex field amplitude. Furthermore, the observed electric field $\vec{E}$ can be found by taking the real part of Equation 2.4. $\vec{e}_s$ is the polarization vector and gives the direction of the electric field. Writing Equations 2.2 and 2.3 as polarization vectors $\vec{e}_+$ and $\vec{e}_-$ gives

$$\vec{e}_+ \equiv \vec{e}_{s=1} \quad = \frac{1}{\sqrt{2}}\vec{e}_x + \frac{i}{\sqrt{2}}\vec{e}_y \tag{2.5}$$

$$\vec{e}_- \equiv \vec{e}_{s=-1} = \frac{1}{\sqrt{2}}\vec{e}_x - \frac{i}{\sqrt{2}}\vec{e}_y. \tag{2.6}$$

The complex field amplitude $E(r,\phi,z)$ of Equation 2.4 can take the form of a Bessel function or a Gaussian. The former is the exact solution to the Helmholtz equation for electromagnetic waves, and simplifies to the latter when the divergence of the beam is small (paraxial approximation). The

[1] This handedness convention is used within quantum physics, but optics textbooks and papers (and Wikipedia) use the point of view of the receiver. In that case, Equation 2.2 and Equation 2.3 are swapped.

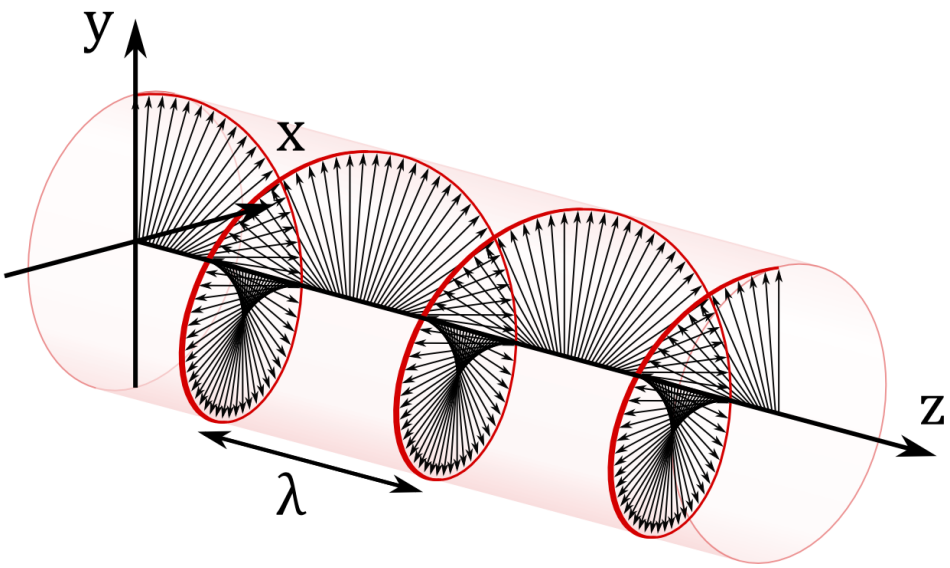

Figure 2.1 The polarization vector of a beam of light carrying spin angular momentum $+\hbar$ rotates around the propagation axis. Beam propagates from left to right in the $+\hat{z}$ direction and the polarization vector in black rotates in a right-handed manner. Adapted from [5].

choice between these two affects only the r dependence of the field and the curvature of phase fronts, but they exhibit the same qualitative rotation behavior, which is what we are really interested in. Thus our choice of whether to use a Bessel or Gaussian transverse mode comes down to previous literature. In talking about the basics of spin and orbital angular momentum of monochromatic light, we adopt a Gaussian convention to match our lab's other projects with angular momentum. However, in later chapters of this thesis, we deal with polychromatic modes where the convention is to use Bessel functions. Following previous literature in the field, we choose to use Bessel functions there.

The complex field amplitude of a Gaussian beam can be written as

$$E(r,\phi,z) = E_0\, f(\phi)\frac{w_0}{w(z)}\exp\left(\frac{-r^2}{w(z)^2} - ikz - ik\frac{r^2}{2R(z)} + i\zeta(z)\right) \tag{2.7}$$

where k is the wavevector, w_0 is the beam waist, E_0 is the magnitude of the electric field at $r = 0$ and $z = 0$, and $f(\phi)$ is some function of ϕ which is 1 for zero orbital angular momentum.[6] Included in this expression are many factors that vary depending on the z position, including the Gouy

phase shift $\zeta(z)$, the radius of curvature $R(z)$, and the beam width $w(z)$.

While Equation 2.7 is useful when dealing with the entire beam, here we simply want to know how the direction of the electric field rotates as a function of time. The intricacies of how the mode profile changes as a function of distance z do not affect the time dependence. A simpler expression would be to approximate this beam as a "collimated Gaussian beam," with the same transverse Gaussian shape at all values of z. This approximation allows us to focus on the time dependence. Mathematically, this is expressed as

$$E(r,\phi,z) \approx E(r,\phi)e^{ikz} \tag{2.8}$$

where $E(r,\phi)$ is a Gaussian, and real for zero orbital angular momentum. Substituting this expression into Equation 2.4, we get

$$\vec{E}(r,\phi,z,t) = E(r,\phi)e^{i(kz-\omega t)}\vec{e}_s. \tag{2.9}$$

Now if we consider a right circularly polarized beam of light, we can use Equation 2.5 for the polarization vector, yielding

$$\vec{E}(r,\phi,z,t) = E(r,\phi)e^{i(kz-\omega t)}\left(\frac{1}{\sqrt{2}}\vec{e}_x + \frac{i}{\sqrt{2}}\vec{e}_y\right) \tag{2.10}$$

$$= E(r,\phi)\Big[\big(\cos(kz-\omega t)\vec{e}_x - \sin(kz-\omega t)\vec{e}_y\big) + i\left(\sin(kz-\omega t)\vec{e}_x + \cos(kz-\omega t)\vec{e}_y\right)\Big] \tag{2.11}$$

$$\mathrm{Re}\left[\vec{E}(r,\phi,z,t)\right] = E(r,\phi)\left[\cos(kz-\omega t)\vec{e}_x - \sin(kz-\omega t)\vec{e}_y\right] \tag{2.12}$$

where in the last step we have taken the real part of the complex field to obtain the field pattern we would actually observe in the lab. This procedure will remain a theme in this thesis, as we are concerned with the physical, real electric field. Figure 2.1 shows Equation 2.12 in a three dimensional scheme, but it is hard to gauge the behavior of the beam as a function of time. Following our argument for using the collimated Gaussian beam approximation, here we want to focus solely on the time dependence. Thus in visualizing rotation in this thesis, we examine the behavior of a transverse slice of the beam at $z = 0$. This allows us to simplify Equation 2.12 becomes

$$\mathrm{Re}\left[\vec{E}(r,\phi,0,t)\right] = E(r,\phi)\left[\cos(\omega t)\vec{e}_x + \sin(\omega t)\vec{e}_y\right] \tag{2.13}$$

which corresponds to right-handed rotation as time increases. Figure 2.2 shows the E field pattern of a transverse slice of a beam carrying spin angular momentum of $+\hbar$ at $z = 0$. As time increases from Figure 2.2(a) to

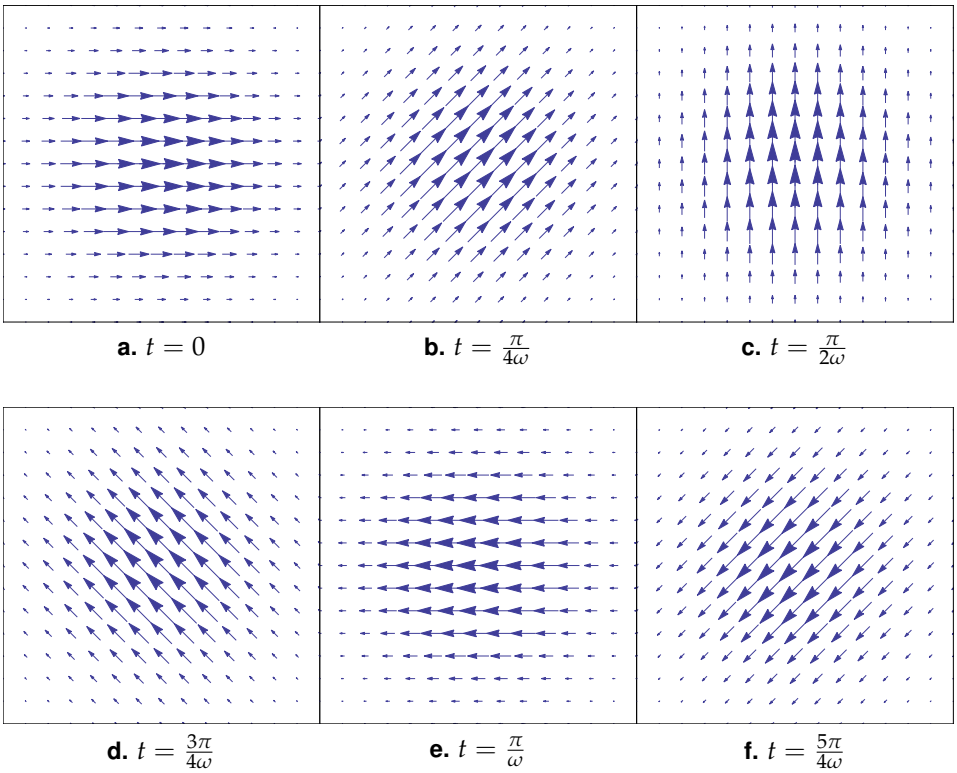

Figure 2.2 Cross-sectional vector pattern of E field given by Equation 2.13. Cross-sectional view of Figure 2.1 at $z = 0$, with the beam propagating out of the page. Arrows are electric field lines, where length of the arrow represents strength of the E field. Dimensions of frame are three beam waists on each side.

(f), the electric field vectors rotate counter-clockwise about the propagation axis pointing out of the page. Thus as expected, these vectors rotate right-handedly.

2.2 Orbital Angular Momentum of Light

Beams of light also carry orbital angular momentum (OAM), where the field amplitude distribution of the beam rotates about the axis of propagation. From quantum mechanics, we have the eigenvalue equation for OAM

$$\hat{L}_z|\ell\rangle = \ell\hbar|\ell\rangle \tag{2.14}$$

where the angular momentum operator $\hat{L}_z$ acts on an eigenstate $|\ell\rangle$ to produce the OAM eigenvalue $\ell\hbar$, where ℓ is an integer. The complex electric field from Equation 2.4 is now given by

$$\vec{E}(r,\phi,z,t) = E(r,\phi,z)e^{-i\omega t}\vec{e}_s \tag{2.15}$$

$$\approx E(r,\phi)e^{i(kz-\omega t)}\vec{e}_s \tag{2.16}$$

$$= E(r)e^{i(kz+\ell\phi-\omega t)}\vec{e}_s \tag{2.17}$$

where in the second step we have assumed the collimated Gaussian beam that we introduced in our treatment of spin angular momentum in Section 2.1. Again, this changes the shape of the mode as a function of z, but in our investigation into the rotation of the electric field, this has no effect. In the last step we have written out the ϕ dependence explicitly for a beam carrying nonzero OAM. $E(r)$ is the transverse mode of the beam, which, as mentioned before, can be a Bessel mode (exact solution) or a Gaussian (paraxial approximation). Here, we choose this to be Gaussian to match our lab's conventions, but again this does not have an effect on the rotation that we are interested in.

To take out any rotation contribution from the spin angular momentum and examine solely the effect of nonzero OAM, we take the beam to be horizontally polarized. Then, we expand Equation 2.17 to obtain

$$\vec{E}(r,\phi,z,t) = E(r)\left[\cos(kz+\ell\phi-\omega t) + i\sin(kz+\ell\phi-\omega t)\right]\vec{e}_x. \tag{2.18}$$

As with spin angular momentum in the previous section, we take the real part to obtain the electric field we would observe in the lab,

$$\mathrm{Re}\left[\vec{E}(r,\phi,z,t)\right] = E(r)\cos(kz+\ell\phi-\omega t)\vec{e}_x \tag{2.19}$$

where we see that our choice of a linear polarization has forced all of the vectors of this vector field to point horizontally. Positive regions of electric field cause the vectors to point right while negative regions flip the vectors to point left. Nonzero OAM adds a transverse-position-dependent phase

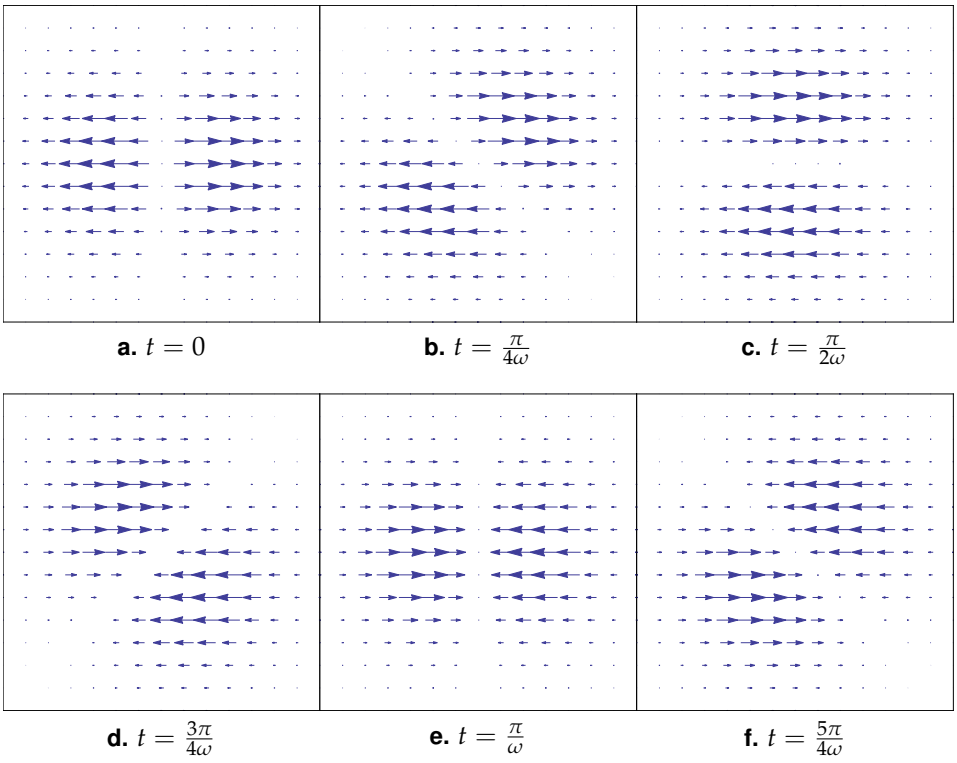

Figure 2.3 Cross-sectional vector pattern of E field given by Equation 2.19 at $z = 0$. Beam propagates out of the page and arrow length represents the magnitude of the field. Adapted from simulations by Neal Pisenti (HMC '11). Dimensions of frame are three beam waists on each side.

shift to the wave's sinusoidal motion along z and t, so that different positions about the propagation axis now have different phase.

Note that if we take $z = 0$ and $t = 0$, this electric field reduces down to a single $\cos(\ell\phi)$ term multiplying the mode profile $E(r)$. As we go around the z axis from $\phi = 0$ and $\phi = 2\pi$, the magnitude of the field is dictated by this cosine and thus exhibits (positive) maxima and (negative) minima. Figure 2.3 depicts the time evolution of a transverse slice of Equation 2.19 at $z = 0$. Here, we have modeled a Gaussian beam with OAM quantum number $\ell = 1$, so there are two areas of nonzero E field magnitude: a maximum and a minimum. Note that this transverse profile rotates right handedly, as expected of a beam carrying positive OAM.

These plots also show a singularity at the center $r = 0$, a hallmark of

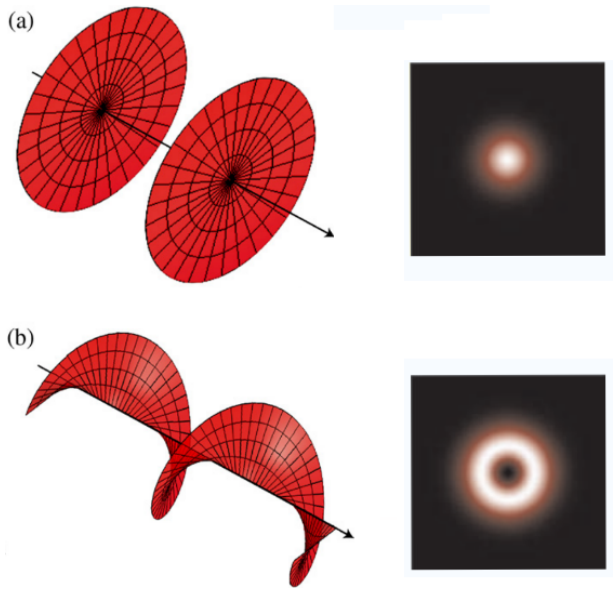

Figure 2.4 Phase surfaces (left) and cross-sectional time-averaged intensity profiles (right) for beams of light carrying (a) zero OAM and (b) OAM $\ell\hbar$. Adapted from [7] and [8].

nonzero OAM. From Equation 2.19, we see that for a surface of constant phase, $\ell\phi + kz - \omega t$ must equal a constant. But at the origin, $r = 0$, ϕ can take on any number of values and thus is ill-defined. As a result, the phase can take on any number of values so it, too, becomes ill-defined. The only solution, then, is to have zero magnitude $E = 0$ at $r = 0$ to avoid choosing any one phase value.

The time-averaged intensity of a beam of light with OAM quantum number $\ell = 1$ is shown on the right in Figure 2.4(b). The regions of nonzero field form a "donut" shape around the singularity in the center. In contrast, the time-averaged intensity profile of a beam with zero OAM is shown on the right in part (a), and exhibits a Gaussian shape.

The left side of Figure 2.4 shows surfaces of constant phase for light with (a) zero OAM and (b) OAM $+\hbar$. For the zero OAM beam, these phase surfaces are approximately disks (pictured) in the case where the waist of the beam is much greater than the wavelength. That is, the electric field has the same phase all across the transverse plane at some z value. But for nonzero OAM, the phase of the light acquires an extra $\ell\phi$ term. As discussed above, this causes the surface of constant phase to obey the relation $\ell\phi + kz - \omega t$, producing a helical surface of constant phase.

For a more in-depth discussion of the orbital angular momentum of light, see the thesis of David Spierings (HMC '14). [9]

The rest of this thesis will be concerned with polychromatic beams of light. In the next chapter, we will introduce these beams of light and calculate the angular momenta they carry. Just as we have done in this chapter, we will derive expressions for the electric fields and model them, comparing the observed rotation to what we would expect from the calculated values of angular momenta.

Chapter 3

Slowly Rotating Mode Theory

Our discussion of spin and orbital angular momentum in Chapter 2 has focused on monochromatic beams of light. We have now a basic understanding of what angular momentum means for light with a single frequency, and how this manifests physically in the transverse electric field vector pattern and field amplitude distribution.

Initial work by Bekshaev [10], Alexeyev [11], and Nienhuis [12] applied these angular momentum concepts to various polychromatic modes. In a 2007 paper, van Enk and Nienhuis [1] refined these arguments, presenting superpositions of two different modes of light carrying angular momentum of opposite sign. Moreover, they detuned the frequencies of these modes by Δ, and found that the overall superpositions exhibit slow rotation at the low detuning frequency just as in beat behavior. Thus these modes earn the name **slowly rotating modes of light**.

Previous studies have claimed that some slowly rotating modes exhibit rotation that does not appear to be correlated with the angular momentum that they carry. Some modes may carry positive angular momentum corresponding to right-handed rotation while rotating in a left-handed direction, while others exhibit rotation even in the absence of angular momentum. These unintuitive results have been quite controversial, with researchers presenting classical, quantum, and relativistic arguments [1, 2, 10] attempting to explain away this "paradox." To tackle this problem ourselves, we wish to compare the angular momenta of these modes with the physical rotation of their electric field. To do so, we derive expressions for the angular momenta of these modes and expressions for the real electric fields that these modes would actually produce in the lab. We will use ket notation for the former, and for the latter we will use the procedure used to derive

Equations 2.12 and 2.19 in the previous chapter.

In her 2011-2012 thesis, Susanna Todaro (HMC '12) derived these expressions and modeled them within Mathematica. [3] However, her work in deriving the electric field expressions produced behavior that did not match the results of van Enk and Nienhuis or with our subsequent experimental observations (discussed in Chapter 5). In this chapter, we will derive the electric field expressions from the ground up, and in the following chapter we will show updated Mathematica simulations, some of which hint at resolving the angular momentum paradox.

In this thesis we are concerned with a subset of the family of slowly rotating modes constructed by van Enk and Nienhuis. While van Enk and Nienhuis cover superpositions of both spin and orbital angular momentum, here we examine spin and OAM separately for simplicity. This allows us to separate the effects coming from spin and OAM. Specifically, we construct a set of spin superpositions with a detuning frequency of $\Delta = s\Omega$ so that the constituent mode with higher frequency $\omega + s\Omega$ carries $+s\hbar$ of spin angular momentum and the mode with lower frequency $\omega - s\Omega$ carries $-s\hbar$ of spin angular momentum. We also construct a set of OAM superpositions with detuning frequency $\Delta = \ell\Omega$ between the constituent modes. Here, the mode with higher frequency $\omega + \ell\Omega$ carries $+\ell\hbar$ of OAM and the mode with lower frequency $\omega - \ell\Omega$ carries $-\ell\hbar$ of OAM. In the following section on ket notation, we present concise mathematical descriptions of these slowly rotating modes and explain where the slowly-rotating behavior comes from.

3.1 Ket Notation: Angular Momentum of Slowly Rotating Modes

In this section, we present specific slowly rotating modes of light and derive expressions for their angular momenta. In later sections we will derive and model the rotation of these modes and compare the direction of rotation to the sign of the angular momentum derived here.

We can write the state of a monochromatic beam of light carrying angular momentum as $|\omega, \ell, s\rangle$. Then under this convention, Equation 2.1 and Equation 2.14 become

$$\hat{S}_z|\omega, \ell, s\rangle = s\hbar|\omega, \ell, s\rangle \tag{3.1}$$

$$\hat{L}_z|\omega, \ell, s\rangle = \ell\hbar|\omega, \ell, s\rangle. \tag{3.2}$$

A monochromatic beam with frequency ω carrying no angular momentum can be represented as $|\omega, 0, 0\rangle$. Circularly polarized beams with no OAM are given by $|R\rangle = |\omega, 0, 1\rangle$ and $|L\rangle = |\omega, 0, -1\rangle$, and OAM modes may be written by adjusting the OAM quantum number ℓ.

3.1.1 General Modes

The most general states we consider contain arbitrary amplitude differences between the two constituent angular momentum eigenstates. In creating these states, we detune the frequencies of the constituent states by Δ. We shift the frequency upwards for the positive angular momentum state and downwards for the negative angular momentum state. For spin angular momentum, we can construct the $|q_\pm\rangle$ modes with detuning frequency $\Delta = s\Omega$,

$$|q_+\rangle = \sin\zeta|\omega + s\Omega, \ell, s\rangle + \cos\zeta|\omega - s\Omega, \ell, -s\rangle \tag{3.3}$$
$$|q_-\rangle = \cos\zeta|\omega + s\Omega, \ell, s\rangle - \sin\zeta|\omega - s\Omega, \ell, -s\rangle \tag{3.4}$$

and for OAM superpositions, we can construct the analogous $|r_\pm\rangle$ modes with detuning frequency $\Delta = \ell\Omega$,

$$|r_+\rangle = \sin\zeta|\omega + \ell\Omega, \ell, s\rangle + \cos\zeta|\omega - \ell\Omega, -\ell, s\rangle \tag{3.5}$$
$$|r_-\rangle = \cos\zeta|\omega + \ell\Omega, \ell, s\rangle - \sin\zeta|\omega - \ell\Omega, -\ell, s\rangle \tag{3.6}$$

where in all of these states we have introduced an arbitrary angle ζ that can vary from 0 to 2π, causing differences in amplitude between the positive and negative angular momentum states. The sine and cosine terms result from normalizing these superpositions. Because ζ can be tuned to an arbitrary value, we call these states the **general modes**.

Starting from these general modes, we wish to construct modes that rotate slowly at the detuning frequency Δ, as presented in the work of van Enk and Nienhuis. To do so, we first find the angular momenta of these superpositions. Then, we will tune ζ to some value that matches those of van Enk and Nienhuis in order to investigate the paradoxical behavior they report.

For the $|q_+\rangle$ mode,

$$\begin{aligned}\langle S_z\rangle_{q_+} &= \langle q_+|\hat{S}_z|q_+\rangle \\ &= \sin^2\zeta(s\hbar) + \cos^2\zeta(-s\hbar) \\ &= \boxed{-s\hbar\cos 2\zeta}\end{aligned} \tag{3.7}$$

Table 3.1 Angular momentum expectation values for the general states described by Equations 3.3, 3.4, 3.5, and 3.6.

State	$\langle S_z \rangle$	$\langle L_z \rangle$
$\|q_\pm\rangle$	$\mp s\hbar \cos 2\zeta$	$\ell\hbar$
$\|r_\pm\rangle$	$s\hbar$	$\mp \ell\hbar \cos 2\zeta$

$$\begin{aligned} \langle L_z \rangle_{q_+} &= \langle q_+ | \hat{L}_z | q_+ \rangle \\ &= \sin^2\zeta(\ell\hbar) + \cos^2\zeta(\ell\hbar) \\ &= \boxed{\ell\hbar} \end{aligned} \tag{3.8}$$

The angular momentum expectation values for all four general states are shown in Table 3.1. The spin superpositions have spin angular momenta dependent on ζ and the OAM superpositions have OAM dependent on ζ. We also note that for $\zeta < \pi/4$, the positive index modes $|q_+\rangle$ and $|r_+\rangle$ have negative angular momentum while the negative indexed modes $|q_-\rangle$ and $|r_-\rangle$ have positive angular momentum.

3.1.2 Frequency-Dependent Modes

As mentioned in the previous section, we wish to construct the slowly rotating modes presented by van Enk and Nienhuis. Following their work, we define the angle θ such that

$$\cos\theta = \sqrt{\frac{\omega + \Delta}{2\omega}} \tag{3.9}$$

$$\sin\theta = \sqrt{\frac{\omega - \Delta}{2\omega}} \tag{3.10}$$

where Δ is the detuning frequency. For the spin superpositions $|q_\pm\rangle$, we take $\zeta = \theta$ and let $\Delta = s\Omega$. Then, our spin superpositions become

$$\begin{aligned} |g_+\rangle &= \sin\theta|\omega + s\Omega, \ell, s\rangle + \cos\theta|\omega - s\Omega, \ell, -s\rangle \\ &= \sqrt{\frac{\omega - s\Omega}{2\omega}}|\omega + s\Omega, \ell, s\rangle + \sqrt{\frac{\omega + s\Omega}{2\omega}}|\omega - s\Omega, \ell, -s\rangle \end{aligned} \tag{3.11}$$

$$\begin{aligned} |g_-\rangle &= \cos\theta|\omega + s\Omega, \ell, s\rangle - \sin\theta|\omega - s\Omega, \ell, -s\rangle \\ &= \sqrt{\frac{\omega + s\Omega}{2\omega}}|\omega + s\Omega, \ell, s\rangle - \sqrt{\frac{\omega - s\Omega}{2\omega}}|\omega - s\Omega, \ell, -s\rangle. \end{aligned} \tag{3.12}$$

Table 3.2 Angular momentum expectation values for the frequency-dependent states described by Equations 3.11, 3.12, 3.13, and 3.14.

State	$\langle S_z \rangle$	$\langle L_z \rangle$
$\|g_\pm\rangle$	$\mp\hbar\Omega/\omega$	$\ell\hbar$
$\|h_\pm\rangle$	$s\hbar$	$\mp\ell^2\hbar\Omega/\omega$

Similarly, for the OAM superpositions $|r_\pm\rangle$, we take $\zeta = \theta$ and let $\Delta = \ell\Omega$. Then, our new OAM superpositions are

$$\begin{aligned} |h_+\rangle &= \sin\theta|\omega + \ell\Omega, \ell, s\rangle + \cos\theta|\omega - \ell\Omega, -\ell, s\rangle \\ &= \sqrt{\frac{\omega - \ell\Omega}{2\omega}}|\omega + \ell\Omega, \ell, s\rangle + \sqrt{\frac{\omega + \ell\Omega}{2\omega}}|\omega - \ell\Omega, -\ell, s\rangle \end{aligned} \tag{3.13}$$

$$\begin{aligned} |h_-\rangle &= \cos\theta|\omega + \ell\Omega, \ell, s\rangle - \sin\theta|\omega - \ell\Omega, -\ell, s\rangle \\ &= \sqrt{\frac{\omega + \ell\Omega}{2\omega}}|\omega + \ell\Omega, \ell, s\rangle - \sqrt{\frac{\omega - \ell\Omega}{2\omega}}|\omega - \ell\Omega, -\ell, s\rangle. \end{aligned} \tag{3.14}$$

We can now calculate the angular momentum expectation values. We have set up these modes so that these angular momentum values should depend on Ω. Taking the $|g_+\rangle$ mode as an example, the expectation values of the angular momenta are

$$\begin{aligned} \langle S_z \rangle_{g_+} &= \langle g_+|\hat{S}_z|g_+\rangle \\ &= \sin^2\theta(s\hbar) + \cos^2\theta(-s\hbar) \\ &= s\hbar\left(\frac{\omega - s\Omega}{2\omega} - \frac{\omega + s\Omega}{2\omega}\right) \\ &= -s^2\hbar\frac{\Omega}{\omega} \\ &= \boxed{-\hbar\frac{\Omega}{\omega}} \end{aligned} \tag{3.15}$$

$$\begin{aligned} \langle L_z \rangle_{g_+} &= \langle h_+|\hat{L}_z|h_+\rangle \\ &= \sin^2\theta(\ell\hbar) + \cos^2\theta(\ell\hbar) \\ &= \boxed{\ell\hbar} \end{aligned} \tag{3.16}$$

where in deriving $\langle S_z \rangle_{g_+}$ we have set $s^2 = 1$, as s can only take on values ± 1. The angular momentum expectation values for the four frequency-dependent states are given in Table 3.2. Note that as expected, we have

Table 3.3 Angular momentum expectation values for the equal superposition states described by Equations 3.17, 3.18, 3.19, and 3.20.

State	$\langle S_z \rangle$	$\langle L_z \rangle$
$\lvert b_\pm \rangle$	0	$\ell\hbar$
$\lvert c_\pm \rangle$	$s\hbar$	0

tuned $\zeta = \theta$ such that the angular momenta scale with the frequencies Ω and ω. Furthermore, the plus modes ($\lvert g_+ \rangle$ and $\lvert h_+ \rangle$) carry negative angular momentum while the minus modes ($\lvert g_- \rangle$ and $\lvert h_- \rangle$) carry positive angular momentum.

3.1.3 Equal Superpositions

The frequency-dependent modes carry paradoxical angular momentum, but in the optical regime they are nearly impossible to observe, and we simply cannot observe them in our lab. Because ω is an optical frequency, it is on the order of 100THz. We will show later in Chapter 5 that the detuning frequency Δ ($s\Omega$ for spin and $\ell\Omega$ for OAM) is typically a mechanical frequency that comes out of rotating a half-wave plate (for spin) or a Dove prism (for OAM). The maximum Ω values achievable are on the order of kHz, eleven orders of magnitude smaller than ω. Thus in experiments, we can always say that $\omega \gg \Omega$. Taking this experimental limit, the coefficients $\cos\theta$ and $\sin\theta$ of the frequency dependent modes reduce down to $\frac{1}{\sqrt{2}}$, resulting in equal coefficients preceding the two constituent modes. Thus, we call these modes **equal superpositions**. This final set of modes $\lvert b_\pm \rangle$ (spin) and $\lvert c_\pm \rangle$ (OAM) take the form

$$\lvert b_+ \rangle = \frac{1}{\sqrt{2}} \lvert \omega + s\Omega, \ell, s \rangle + \frac{1}{\sqrt{2}} \lvert \omega - s\Omega, \ell, -s \rangle \tag{3.17}$$

$$\lvert b_- \rangle = \frac{1}{\sqrt{2}} \lvert \omega + s\Omega, \ell, s \rangle - \frac{1}{\sqrt{2}} \lvert \omega - s\Omega, \ell, -s \rangle \tag{3.18}$$

$$\lvert c_+ \rangle = \frac{1}{\sqrt{2}} \lvert \omega + \ell\Omega, \ell, s \rangle + \frac{1}{\sqrt{2}} \lvert \omega - \ell\Omega, -\ell, s \rangle \tag{3.19}$$

$$\lvert c_- \rangle = \frac{1}{\sqrt{2}} \lvert \omega + \ell\Omega, \ell, s \rangle - \frac{1}{\sqrt{2}} \lvert \omega - \ell\Omega, -\ell, s \rangle. \tag{3.20}$$

The angular momentum expectation values are easy to see here. For $\lvert b_\pm \rangle$, the expectation value of spin angular momentum is zero and for $\lvert c_\pm \rangle$,

Table 3.4 The family of slowly rotating modes that we are interested in. Naming convention adopted from [3] but originally from [1].

	General ζ	Ω dependent $\zeta = \theta$	Equal sup. $\zeta = \pi/4$
Spin superpositions $\langle S_z \rangle$	$\lvert q_\pm \rangle$ $\mp s\hbar \cos 2\zeta$	$\lvert g_\pm \rangle$ $\mp \hbar\Omega/\omega$	$\lvert b_\pm \rangle$ 0
OAM superpositions $\langle L_z \rangle$	$\lvert r_\pm \rangle$ $\mp \ell\hbar \cos 2\zeta$	$\lvert h_\pm \rangle$ $\mp \ell^2\hbar\Omega/\omega$	$\lvert c_\pm \rangle$ 0

the expectation value of OAM is zero. Put another way, the spin superpositions $|b_\pm\rangle$ carry zero spin angular momentum, so the polarization vector should exhibit no net rotation. Similarly, the OAM superpositions $|c_\pm\rangle$ carry zero OAM, so the E field pattern should exhibit no net rotation.

Table 3.4 summarizes the twelve slowly rotating modes of light that we have introduced and discussed in previous sections. We note that slowly rotating modes are not limited to these twelve states. van Enk and Nienhuis discuss modes where both the polarization vector and the intensity pattern rotate at the same and at different frequencies. [1]

3.2 Electric Field and Rotation

The ket notation for the slowly rotating modes described in Section 3.1 gives an easy and compact description, yet it does not provide much physical information. Instead, as we did in Chapter 2 with circular polarization and OAM eigenstates, we want to derive expressions for the real electric field of these slowly rotating modes, and then model them. This will allow us to compare the actual physical behavior of the electric field of the modes with the angular momenta they carry.

We start at the complex electric field of a light beam given by Equation 2.17, where we chose not to explicitly write out the transverse mode $E(r)$. In our work, we follow van Enk and Nienhuis and choose to use the exact solutions to the Helmholtz equation, resulting in Bessel functions

$$E(r) = \sqrt{\frac{\hbar\omega}{4\pi\epsilon_0 c}} J_{|\ell|}(k_r r) \tag{3.21}$$

where $J_{|\ell|}(k_r r)$ is the Bessel function of the first kind and k_r is the transverse component of the wavevector $\vec{k}$. Then, plugging into Equation 2.17, we get

$$\vec{E}(r, \phi, z, t) = \sqrt{\frac{\hbar\omega}{4\pi\epsilon_0 c}} e^{i\ell\phi} e^{-i\omega t} e^{ik_z z} J_{|\ell|}(k_r r)\vec{e}. \tag{3.22}$$

We can express the complex electric fields of our slowly rotating modes by simply summing the electric field contributions from the two eigenstates. We seek to find out if our modes rotate, and in which direction. In Chapter 4 we show the simulations of the expressions we will derive below.

3.2.1 Spin superpositions

Our strategy for the spin superpositions is to first obtain an expression for the complex electric field of the slowly rotating modes. Then, we will take the real part of this complex field and let $z = 0$ to obtain the time dependent behavior of a transverse slice of the electric field. We will model this behavior and discuss the rotation of the modes in Chapter 4.

We note that this approach is vastly different from the approach that Susanna Todaro used in her thesis work. In her approach, Susanna took the square root of the complex electric field times its complex conjugate in order to "average out" the ω dependence. However, as we will see from

our derivation, it is not necessary to purposely remove the ω dependence. In fact, as we will see when we model the spin superpositions in the next chapter, retaining and analyzing this ω dependence may help us explain why a state can appear to rotate in the direction opposing its angular momentum.

We begin with the general state $|q_+\rangle$. Again, from Equation 3.3 we have

$$|q_+\rangle = \sin\zeta|\omega + s\Omega, \ell, s\rangle + \cos\zeta|\omega - s\Omega, \ell, -s\rangle$$

which in our electric field notation is described as

$$\begin{aligned}
\vec{E}_{q_+} &= \sin\zeta\, \vec{E}_{\omega+s\Omega,\ell,s} + \cos\zeta\, \vec{E}_{\omega-s\Omega,\ell,-s} \\
&= e^{i\ell\phi}e^{ik_z z}J_{|\ell|}(k_r r)\left(\sqrt{\frac{\hbar(\omega+s\Omega)}{4\pi\epsilon_0 c}}\sin\zeta e^{-i(\omega-s\Omega)t}\vec{e}_s \right. \\
&\qquad \left. + \sqrt{\frac{\hbar(\omega-s\Omega)}{4\pi\epsilon_0 c}}\cos\zeta e^{-i(\omega-s\Omega)t}\vec{e}_{-s}\right) \\
&= \sqrt{\frac{\hbar\omega}{2\pi\epsilon_0 c}}e^{ik_z z}e^{i\ell\phi}e^{-i\omega t}J_{|\ell|}(k_r r)\left(\sqrt{\frac{\omega+s\Omega}{2\omega}}\sin\zeta e^{-is\Omega t}\vec{e}_s \right. \\
&\qquad \left. + \sqrt{\frac{\omega-s\Omega}{2\omega}}\cos\zeta e^{is\Omega t}\vec{e}_{-s}\right) \\
&= \sqrt{2}\,E(r,z)e^{i\ell\phi}e^{-i\omega t}J_{|\ell|}(k_r r)\left(\cos\theta\sin\zeta e^{-is\Omega t}\vec{e}_s + \sin\theta\cos\zeta e^{is\Omega t}\vec{e}_{-s}\right)
\end{aligned}$$

where in the second step we have plugged in the base electric field from Equation 3.22. In the last step, we have substituted $\cos\theta$ and $\sin\theta$ as defined by Equation 3.9 and Equation 3.10 with $\Delta = s\Omega$. We have also plugged back in for

$$\begin{aligned}
E(r,z) &= E(r)e^{ik_z z} \\
&= \sqrt{\frac{\hbar\omega}{4\pi\epsilon_0 c}}e^{ik_z z}J_{|\ell|}(k_r r).
\end{aligned}$$

If we take $s = 1$, then we can plug in our expressions for the polarization vectors in the $\{\vec{e}_x, \vec{e}_y\}$ basis from Equations 2.5 and 2.6 to get

$$\begin{aligned}
\vec{E}_{q_+} = \sqrt{2}E(r,z)e^{i(\ell\phi-\omega t)}\Big[&\left(\cos\theta\sin\zeta e^{-i\Omega t} + \sin\theta\cos\zeta e^{i\Omega t}\right)\vec{e}_x \\
&+ i\left(\cos\theta\sin\zeta e^{-i\Omega t} - \sin\theta\cos\zeta e^{i\Omega t}\right)\vec{e}_y\Big].
\end{aligned} \tag{3.23}$$

Similarly, we can calculate the electric field for the $|q_-\rangle$ mode, yielding

$$\begin{aligned}\vec{E}_{q_-} = \sqrt{2}E(r,z)e^{i(\ell\phi-\omega t)}\Bigg[&\left(\cos\theta\cos\zeta e^{-i\Omega t} - \sin\theta\sin\zeta e^{i\Omega t}\right)\vec{e}_x \\ &+i\left(\cos\theta\cos\zeta e^{-i\Omega t} + \sin\theta\sin\zeta e^{i\Omega t}\right)\vec{e}_y\Bigg].\end{aligned} \tag{3.24}$$

Combining Equations 3.23 and 3.24, we can rewrite the electric field for the $|q_\pm\rangle$ modes as

$$\begin{aligned}\vec{E}_{q_\pm} =&\sqrt{2}\left(\mathrm{Re}\left[E(r,z)e^{i\ell\phi}\right] + i\,\mathrm{Im}\left[E(r,z)e^{i\ell\phi}\right]\right) \\ &\times\left(\cos\omega t - i\sin\omega t\right)\left(\mathrm{Re}\left[\vec{e}_{q_\pm}\right] + i\,\mathrm{Im}\left[\vec{e}_{q_\pm}\right]\right).\end{aligned}$$

So that when we take the real part to get the real electric field, we obtain

$$\begin{aligned}\mathrm{Re}\left[\vec{E}_{q_\pm}\right] =&\sqrt{2}\,\mathrm{Re}\left[E(r,z)e^{i\ell\phi}\right]\left(\cos\omega t\,\mathrm{Re}\left[\vec{e}_{q_\pm}\right] + \sin\omega t\,\mathrm{Im}\left[\vec{e}_{q_\pm}\right]\right) \\ &+\sqrt{2}\,\mathrm{Im}\left[E(r,z)e^{i\ell\phi}\right]\left(\sin\omega t\,\mathrm{Re}\left[\vec{e}_{q_\pm}\right] - \cos\omega t\,\mathrm{Im}\left[\vec{e}_{q_\pm}\right]\right)\end{aligned} \tag{3.25}$$

where we have defined $\vec{e}_{q_+}$ and $\vec{e}_{q_-}$ to be the terms in the brackets of Equations 3.23 and 3.24, respectively.

$$\begin{aligned}\vec{e}_{q_+} = \Bigg[&\left(\cos\theta\sin\zeta e^{-i\Omega t} + \sin\theta\cos\zeta e^{i\Omega t}\right)\vec{e}_x \\ &+i\left(\cos\theta\sin\zeta e^{-i\Omega t} - \sin\theta\cos\zeta e^{i\Omega t}\right)\vec{e}_y\Bigg]\end{aligned} \tag{3.26}$$

$$\begin{aligned}\vec{e}_{q_-} = \Bigg[&\left(\cos\theta\cos\zeta e^{-i\Omega t} - \sin\theta\sin\zeta e^{i\Omega t}\right)\vec{e}_x \\ &+i\left(\cos\theta\cos\zeta e^{-i\Omega t} + \sin\theta\sin\zeta e^{i\Omega t}\right)\vec{e}_y\Bigg].\end{aligned} \tag{3.27}$$

These polarization vectors have real and imaginary components

$$\mathrm{Re}\left[\vec{e}_{q_+}\right] = \left(\cos\theta\sin\zeta + \sin\theta\cos\zeta\right)\left(\cos\Omega t\,\vec{e}_x + \sin\Omega t\,\vec{e}_y\right) \tag{3.28}$$

$$\mathrm{Im}\left[\vec{e}_{q_+}\right] = \left(\cos\theta\sin\zeta - \sin\theta\cos\zeta\right)\left(-\sin\Omega t\,\vec{e}_x + \cos\Omega t\,\vec{e}_y\right) \tag{3.29}$$

$$\mathrm{Re}\left[\vec{e}_{q_-}\right] = \left(\cos\theta\cos\zeta - \sin\theta\sin\zeta\right)\left(\cos\Omega t\,\vec{e}_x + \sin\Omega t\,\vec{e}_y\right) \tag{3.30}$$

$$\mathrm{Im}\left[\vec{e}_{q_-}\right] = \left(\cos\theta\cos\zeta + \sin\theta\sin\zeta\right)\left(-\sin\Omega t\,\vec{e}_x + \cos\Omega t\,\vec{e}_y\right). \tag{3.31}$$

We can examine the **frequency-dependent modes** $|g_\pm\rangle$. To do so, we simply take $\zeta = \theta$, changing the polarization vector components to

$$\text{Re}\left[\vec{e}_{g_+}\right] = 2\cos\theta\sin\theta\left(\cos\Omega t\,\vec{e}_x + \sin\Omega t\,\vec{e}_y\right) \tag{3.32}$$

$$\text{Im}\left[\vec{e}_{g_+}\right] = 0 \tag{3.33}$$

$$\text{Re}\left[\vec{e}_{g_-}\right] = \left(\cos^2\theta - \sin^2\theta\right)\left(\cos\Omega t\,\vec{e}_x + \sin\Omega t\,\vec{e}_y\right) \tag{3.34}$$

$$\text{Im}\left[\vec{e}_{g_-}\right] = -\sin\Omega t\,\vec{e}_x + \cos\Omega t\,\vec{e}_y. \tag{3.35}$$

Recall from Section 2.1 that we visualized spin angular momentum by looking at the time evolution of a transverse slice of the E field at $z = 0$. We take the same approach here, and set $z = 0$. Furthermore, we set $\ell = 0$ to focus solely on spin angular momentum. Then, Equation 3.25 reduces down to

$$\text{Re}\left[\vec{E}_{g_\pm}\right] = \sqrt{2}\,E(r)\left(\cos\omega t\,\text{Re}\left[\vec{e}_{q_\pm}\right] + \sin\omega t\,\text{Im}\left[\vec{e}_{q_\pm}\right]\right). \tag{3.36}$$

Plugging in the polarization vector components from Equations 3.32 and 3.33, we get the real electric field of the $|g_+\rangle$ mode at $z = 0$,

$$\boxed{\text{Re}\left[\vec{E}_{g_+}\right] = 2\sqrt{2}\,E(r)\cos(\omega t)\cos\theta\sin\theta\left(\cos\Omega t\,\vec{e}_x + \sin\Omega t\,\vec{e}_y\right)} \tag{3.37}$$

Doing the same for the $|g_-\rangle$ mode, we substitute the polarization vector components from Equations 3.34 and 3.35 to obtain

$$\text{Re}\left[\vec{E}_{g_-}\right] = \sqrt{2}\,E(r)\Big[\cos(\omega t)\left(\cos^2\theta - \sin^2\theta\right)\left(\cos\Omega t\,\vec{e}_x + \sin\Omega t\,\vec{e}_y\right) + \sin(\omega t)\left(-\sin\Omega t\,\vec{e}_x + \cos\Omega t\,\vec{e}_y\right)\Big]$$

which can be simplified further by plugging in our expressions for $\cos\theta$ and $\sin\theta$ from Equations 3.9 and 3.10. This yields

$$\boxed{\text{Re}\left[\vec{E}_{g_-}\right] = \sqrt{2}\,E(r)\Big[\cos(\omega t)\frac{\Omega}{\omega}\left(\cos\Omega t\,\vec{e}_x + \sin\Omega t\,\vec{e}_y\right) + \sin(\omega t)\left(-\sin\Omega t\,\vec{e}_x + \cos\Omega t\,\vec{e}_y\right)\Big]} \tag{3.38}$$

We can also take $\zeta = \pi/4$ to examine the $|b_\pm\rangle$ **equal superpositions**. In this case, the polarization vector components become

$$\mathrm{Re}\left[\vec{e}_{b_+}\right] = \frac{1}{\sqrt{2}}\left(\cos\theta + \sin\theta\right)\left(\cos\Omega t\,\vec{e}_x + \sin\Omega t\,\vec{e}_y\right) \tag{3.39}$$

$$\mathrm{Im}\left[\vec{e}_{b_+}\right] = \frac{1}{\sqrt{2}}\left(\cos\theta - \sin\theta\right)\left(-\sin\Omega t\,\vec{e}_x + \cos\Omega t\,\vec{e}_y\right) \tag{3.40}$$

$$\mathrm{Re}\left[\vec{e}_{b_-}\right] = \frac{1}{\sqrt{2}}\left(\cos\theta - \sin\theta\right)\left(\cos\Omega t\,\vec{e}_x + \sin\Omega t\,\vec{e}_y\right) \tag{3.41}$$

$$\mathrm{Im}\left[\vec{e}_{b_-}\right] = \frac{1}{\sqrt{2}}\left(\cos\theta + \sin\theta\right)\left(-\sin\Omega t\,\vec{e}_x + \cos\Omega t\,\vec{e}_y\right). \tag{3.42}$$

We impose the experimental limit $\omega \gg \Omega$ and let $\ell = 0$. Again, we take a transverse slice of the real electric field at $z = 0$, yielding

$$\boxed{\begin{aligned}\mathrm{Re}\left[\vec{E}_{b_+}\right] &= E(r)\cos(\omega t)\left(\cos\Omega t\,\vec{e}_x + \sin\Omega t\,\vec{e}_y\right) \qquad (3.43)\\ \mathrm{Re}\left[\vec{E}_{b_-}\right] &= E(r)\sin(\omega t)\left(-\sin\Omega t\,\vec{e}_x + \cos\Omega t\,\vec{e}_y\right) \qquad (3.44)\end{aligned}}$$

3.2.2 OAM superpositions

We follow the same approach for the OAM superpositions that as we have already taken for the spin superpositions: take the real part of the complex electric field. Again, this stands in contrast to the method used by Susanna Todaro in her thesis work. Susanna multiplied the complex electric field by its complex conjugate, obtaining a time-dependent "intensity" which she then plotted and simulated. This approach eliminates dependence on ω, and loses all sign information, which Susanna then recovered by an ad hoc method. However, like in the case with the spin superpositions, retaining this ω dependence may in fact allow us to explain the paradoxical rotation of the OAM superpositions.

Starting with the general state $|r_+\rangle$, we can find the electric field just as we did with the spin superpositions above. Again, $|r_+\rangle$ is given by

$$|r_+\rangle = \sin\zeta|\omega + \ell\Omega, \ell, s\rangle + \cos\zeta|\omega - \ell\Omega, -\ell, s\rangle$$

so its electric field is given by

$$\begin{aligned}\vec{E}_{r_+} &= \sin\zeta\,\vec{E}_{\omega+\ell\Omega,\ell,s} + \cos\zeta\,\vec{E}_{\omega-\ell\Omega,-\ell,s}\\ &= \sqrt{2}\,E(r)\,e^{-i\omega t}\vec{e}_s\left(\cos\theta\sin\zeta e^{i\ell(\phi-\Omega t)} + \sin\theta\cos\zeta e^{-i\ell(\phi-\Omega t)}\right).\end{aligned}$$

Similarly, the $|r_-\rangle$ mode has a complex electric field

$$\vec{E}_{r_-} = \sqrt{2}\,E(r)\,e^{-i\omega t}\vec{e}_s\left(\cos\theta\cos\zeta e^{i\ell(\phi-\Omega t)} - \sin\theta\sin\zeta e^{-i\ell(\phi-\Omega t)}\right).$$

Now we can take the case where $\zeta = \theta$ to obtain expressions for the frequency-dependent modes $|h_\pm\rangle$. Beginning with the $|h_+\rangle$ mode,

$$\begin{aligned}\vec{E}_{h_+} &= \sqrt{2}\,E(r)\,e^{-i\omega t}\vec{e}_s\cos\theta\sin\theta\left(e^{i\ell(\phi-\Omega t)} - e^{-i\ell(\phi-\Omega t)}\right)\\ &= 2\sqrt{2}\,E(r)\,e^{-i\omega t}\cos\theta\sin\theta\cos\left[\ell\left(\phi-\Omega t\right)\right]\vec{e}_s.\end{aligned}$$

And so we can take the real part to obtain

$$\boxed{\mathrm{Re}\left[\vec{E}_{h_+}\right] = 2\sqrt{2}\,E(r)\,\cos\left(\omega t\right)\cos\theta\sin\theta\cos\left[\ell\left(\phi-\Omega t\right)\right]\vec{e}_s} \tag{3.45}$$

We can also derive the real electric field of the $|q_-\rangle$ mode in the same fashion, obtaining an expression that is much more complex,

$$\boxed{\begin{aligned}\mathrm{Re}\left[\vec{E}_{h_-}\right] = \sqrt{2}\,E(r)\,\vec{e}_s\Big(&\cos^2\theta\cos\left[\ell\phi-\left(\omega+\ell\Omega\right)t\right] &(3.46)\\ &-\sin^2\theta\cos\left[\ell\phi+\left(\omega-\ell\Omega\right)t\right]\Big) &(3.47)\end{aligned}}$$

And for the equal superpositions $|c_\pm\rangle$, we set $\zeta = \pi/4$, and take the experimental limit where $\omega \gg \Omega$, obtaining

$$I_{c_\pm} = \frac{1}{2}E(r)^2\left(\frac{1}{2} \pm \cos\theta\sin\theta\cos\left[2\ell\left(\phi-\Omega t\right)\right]\right) \tag{3.48}$$

which, in the limit where $\omega \gg \Omega$, reduces down to

$$\boxed{\begin{aligned}\mathrm{Re}\left[\vec{E}_{c_+}\right] &= \sqrt{2}\,E(r)\,\vec{e}_s\cos\left(\omega t\right)\cos\left[\ell\left(\phi-\Omega t\right)\right] &(3.49)\\ \mathrm{Re}\left[\vec{E}_{c_-}\right] &= \sqrt{2}\,E(r)\,\vec{e}_s\sin\left(\omega t\right)\sin\left[\ell\left(\phi-\Omega t\right)\right] &(3.50)\end{aligned}}$$

In this chapter, we first constructed the family of slowly rotating modes that van Enk and Nienhuis and others have presented in previous work. Then, we calculated the angular momenta carried by these modes. Finally, we have derived expressions for the real electric field for the spin and OAM superpositions. In the following chapter we will model these expressions in Mathematica in order to see the rotation of the modes. We will then compare their rotation with their angular momenta to examine and possibly explain the angular momentum "paradox."

Chapter 4

Mathematica Simulation and Modeling

In the previous chapter, we derived electric field expressions for the spin superpositions and intensity expressions for the OAM superpositions. We model these modes using Mathematica. Specifically, we are interested in simulating expressions of the form

$$\text{Re}\left[\vec{E}\right] = E_x\vec{e}_x + E_y\vec{e}_y \tag{4.1}$$

for the spin superpositions and

$$\text{Re}\left[\vec{E}\right] = E\vec{e}_s \tag{4.2}$$

for the OAM superpositions. To best view a vector field like Equation 4.1, we can use Mathematica's `VectorPlot` function, which we used to produce Figures 2.2 and 2.3 to show spin and orbital angular momentum of light. On the other hand, the field amplitude distribution given by Equation 4.2 is more or less a scalar field, so we can use `VectorPlot` again with some linear polarization $\vec{e}_s = \vec{e}_x$. In addition, we will use `ParametricPlot3D` which gives a surface across a transverse x-y plane. `VectorPlot` is better at visualizing rotation, while `ParametricPlot3D` is better at visualizing changes in amplitude. Thus, we need both in order to best examine these rotating amplitude distributions.

As an example, we plot the base Bessel mode $E(r) \propto J_{|\ell|}(k_r r)$ given by Equation 3.21 using each of these two plotting functions. Figure 4.1 shows the Bessel mode plotted as a surface using `ParametricPlot3D`. Note the maximum at the center, the minimum at a larger radius, and the secondary,

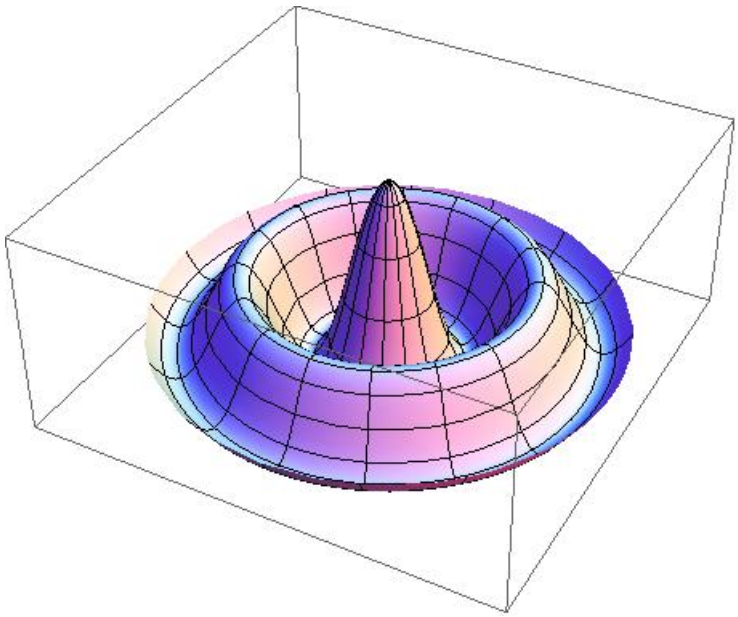

Figure 4.1 The base Bessel mode $E(r)$ given by Equation 3.21, visualized with `ParametricPlot3D`. Radius goes out to $11/k_r$, and the first three Bessel zeroes can be seen.

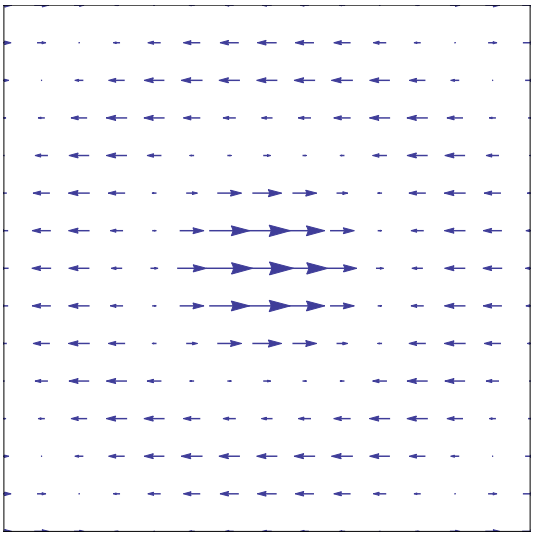

Figure 4.2 The base Bessel mode $E(r)$ given by Equation 3.21 with horizontal polarization, visualized with `VectorPlot`. Frame size is $12/k_r$ on a side, showing the first two Bessel zeroes at $r \approx 2.4/k_r$ and $r \approx 5.5/k_r$.

local maximum even further out. These features will be present within all of our simulations and plots since we choose to use the exact Bessel solutions for our electric field amplitude $E(r)$. Figure 4.2 shows the Bessel mode plotted using `VectorPlot` with horizontal polarization. Note that the middle shows the vectors pointing right, while at a larger radius, the Bessel function becomes negative so the vectors further out point to the left.

We are mostly interested in modeling modes with $\omega \gg \Omega$. In this experimental limit where we can only directly see the slow rotations at frequency close to Ω, our simulations should describe rotational behavior we can experimentally verify in the lab. However, in this chapter we simulate cases where ω is of the same order as Ω to see both fast and slow rotations, which gives us insight into where the 'missing' angular momentum is. The Mathematica code used here is included in Appendix A.

4.1 Simulating the $|g_-\rangle$ mode

In Section 3.2.1, we derived the following expression for the real electric field of $|g_-\rangle$ at $z = 0$:

$$\begin{aligned}\mathrm{Re}\left[\vec{E}_{g_-}\right] = \sqrt{2}\,E(r)\Bigg[&\cos(\omega t)\frac{\Omega}{\omega}\left(\cos\Omega t\,\vec{e}_x + \sin\Omega t\,\vec{e}_y\right)\\ &+ \sin(\omega t)\left(-\sin\Omega t\,\vec{e}_x + \cos\Omega t\,\vec{e}_y\right)\Bigg]\end{aligned} \tag{4.3}$$

where there are two terms that supplement one another. Both of the polarization vector components

$$\cos\Omega t\,\vec{e}_x + \sin\Omega t\,\vec{e}_y \tag{4.4}$$

$$-\sin\Omega t\,\vec{e}_x + \cos\Omega t\,\vec{e}_y \tag{4.5}$$

exhibit right-handed rotation, so the resulting electric field pattern should exhibit overall right-handed rotation. However, the behavior of the amplitude and angular velocity/frequency is more complicated. The two polarization vector components are offset in angle: at $t = 0$, Equation 4.4 is entirely horizontal while Equation 4.5 has only a $\vec{e}_y$ term. Further complicating the issue is the Ω/ω factor that makes the amplitude of the first term smaller than that of the second term. These two terms also are modulated by different $\cos(\omega t)$ and $\sin(\omega t)$ terms. Instead of trying to reason through all of this math, we simply model the electric field.

The nine plots in Figure 4.3 show the time-evolution of the electric field at the $z = 0$ transverse plane, for frequency values $\Omega = 1$ and $\omega = 2$. We

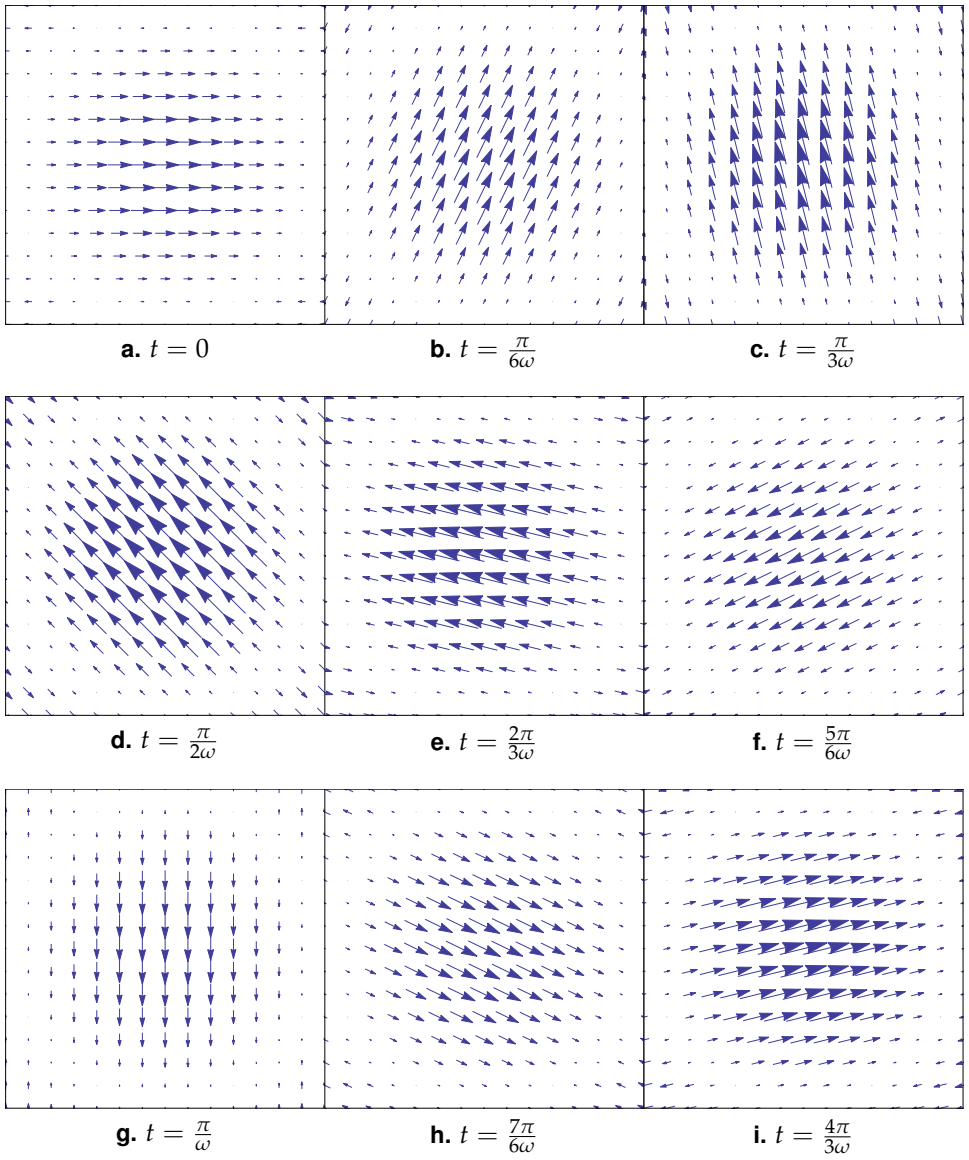

Figure 4.3 Cross-sectional electric vector field for the $|g_-\rangle$ mode at $z = 0$, with the beam propagating out of the page. Here, the frequencies used were $\Omega = 1$ and $\omega = 2$. The nine pictures are separated by equal timesteps of $\frac{\pi}{6\omega}$. Frame size is $5/k_r$ on each side.

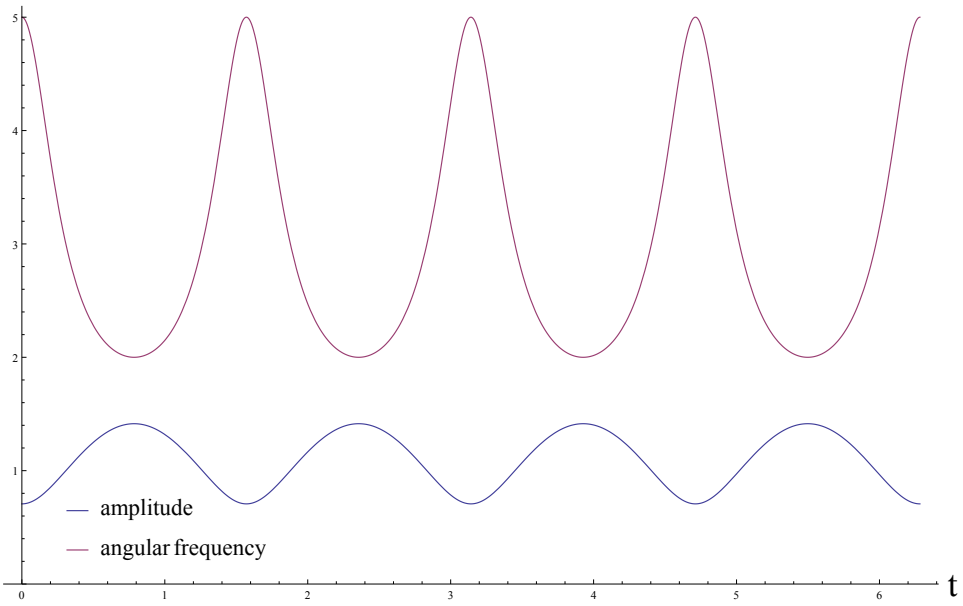

Figure 4.4 Magnitude (blue) and angular frequency/velocity (red) of the electric field of $|g_-\rangle$ at $r = 0$ and $z = 0$, plotted as functions of time. Frequencies used were $\Omega = 1$ and $\omega = 2$.

see that as expected, the vectors all rotate counterclockwise about the propagation axis pointing out of the page, exactly right-handed rotation. The amplitude oscillates between a large value and small value, but never goes to or below zero. However, it appears that the vectors rotate faster when the amplitude is smaller. Figures 4.3(a) through (c) show the vector field with low amplitude, and the vectors rotate by more than 90° in a time span of $\frac{\pi}{3\omega}$. Figures 4.3(c) through (e) show the vector field with high amplitude, and through the same time span of $\frac{\pi}{3\omega}$ the vectors clearly rotate less than 90°.

This relationship between angular frequency and amplitude is shown in Figure 4.4. The amplitude, marked by the blue curve, exhibits a maximum when the angular velocity of the vectors' rotation, marked in red, reaches a minimum. Similarly, the amplitude is at a minimum when the angular velocity is maximized.

Because this simulation does not use physical values for all of the constants, the numbers on the vertical axis in Figure 4.4 do not mean anything. However, we can still determine the functional dependence of the amplitude and angular velocity on the two frequencies ω and Ω.

The minimum and maximum values of the amplitude go as

$$\text{Max [Amplitude]} \propto \sqrt{\omega} \tag{4.6}$$

$$\text{Min [Amplitude]} \propto \frac{\Omega}{\sqrt{\omega}}. \tag{4.7}$$

Here, these values become somewhat obvious looking back at our electric field expression in Equation 4.3. Because the $\cos(\omega t)$ and $\sin(\omega t)$ terms are orthogonal, the minimum value should be where the smaller term is maximized and the larger term is minimized. In other words, because $\omega < \Omega$ always, the ratio $\frac{\Omega}{\omega}$ is less than one and the minimum value of the amplitude should scale as the coefficient preceding the $\cos \omega t$ term. Because $E(r)$ contains a $\sqrt{\omega}$ term, the resultant minimum is just $\frac{\Omega}{\sqrt{\omega}}$. Similarly, the maximum occurs when the $\sin(\omega t)$ term is the only nonzero term, so the maximum value of the amplitude is just $\sqrt{\omega}$.

The minimum and maximum values of the angular frequency go as

$$\text{Max [Frequency]} \propto \frac{\omega^2 + \Omega^2}{\Omega} \tag{4.8}$$

$$\text{Min [Frequency]} \propto 2\Omega. \tag{4.9}$$

These expressions are a lot less transparent compared to the amplitude values, and I did not find an intuitive explanation for why the frequency exhibits this dependence.

4.2 Simulating the $|g_+\rangle$ mode

From our derivation in Section 3.2.1, we arrived at Equation 3.37 describing the real electric field of the $|g_+\rangle$ mode,

$$\text{Re}\left[\vec{E}_{g_+}\right] = \frac{1}{\sqrt{2}} E(r) \cos(\omega t) 2 \cos\theta \sin\theta \left(\cos \Omega t \, \vec{e}_x + \sin \Omega t \, \vec{e}_y\right). \tag{4.10}$$

Figure 4.5 shows our Mathematica simulation of Equation 4.10, for frequency values $\Omega = 1$ and $\omega = 2$, expressed in radians per second. In this thesis, any numbers given for ω and Ω will always be expressed as rad/s unless stated explicitly otherwise. As time progresses, the amplitude of the vector field decreases and then turns negative, flipping the vector. Yet this is to be expected. The expression for $\text{Re}\left[\vec{E}_{g_+}\right]$ above has an overall $\cos(\omega t)$ term that makes these vectors point back and forth sinusoidally.

Yet what is most striking about our simulation is that the real electric field of $|g_m\rangle$ turns in a right-handed manner. Aside from the amplitude modulation by the $\cos(\omega t)$ term, Equation 4.10 also has a pure polarization vector term that goes as $\cos\Omega t\,\vec{e}_x + \sin\Omega t\,\vec{e}_y$. This is none other than counter-clockwise rotation. Since the beam propagation axis comes out of the page, this means that the polarization vector rotates in a right-handed manner about the propagation axis. To obtain this right-handed rotation we would expect the $|g_+\rangle$ mode to have a positive angular momentum. However, from Table 3.4, we know that the spin angular momentum expectation value is negative, or $\langle S_z\rangle_{g_+} = -\hbar\Omega/\omega$.

This difference in signs led Susanna Todaro HMC '12 and previous researchers to conclude that this mode is paradoxical, carrying negative spin angular momentum while rotating as if it had positive spin angular momentum. However, Susanna's calculations and Mathematica simulations did not include the $\cos(\omega t)$ term which modulates our vector amplitudes.

Figure 4.6 shows the same simulation, but the slices are chosen where the norm of the vector field is maximized (i.e. longest arrows). Successive maxima occur at time values that are integral multiples of $\frac{\pi}{2\omega}$. We notice how when we simply look at these images, it appears as though the vector field rotates clockwise, in a left-handed manner. It appears as though there is an overall rotational component that goes right-handedly while the amplitude modulation causes a less striking, but obvious left-handed rotation that may account for the overall negative spin angular momentum. However, this is simply a hunch and we have not found a way to quantify it.

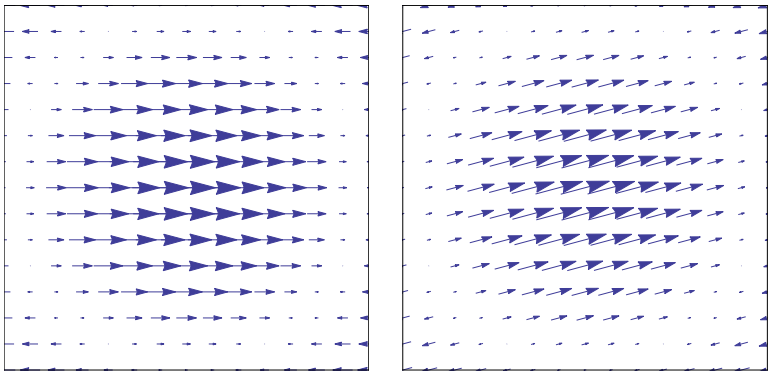

a. $t = 0$ **b.** $t = \frac{\pi}{6\omega}$

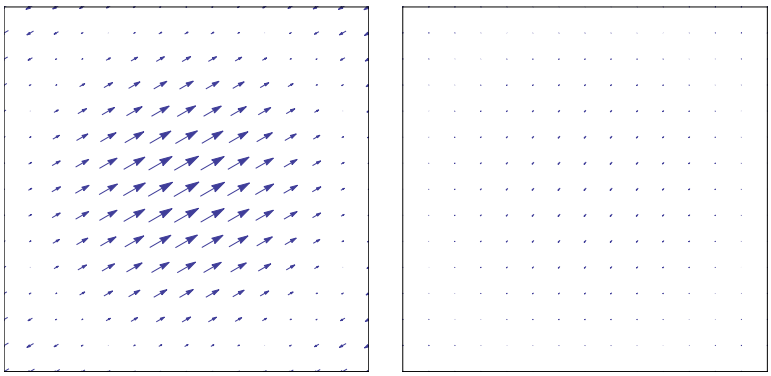

c. $t = \frac{\pi}{3\omega}$ **d.** $t = \frac{\pi}{2\omega}$

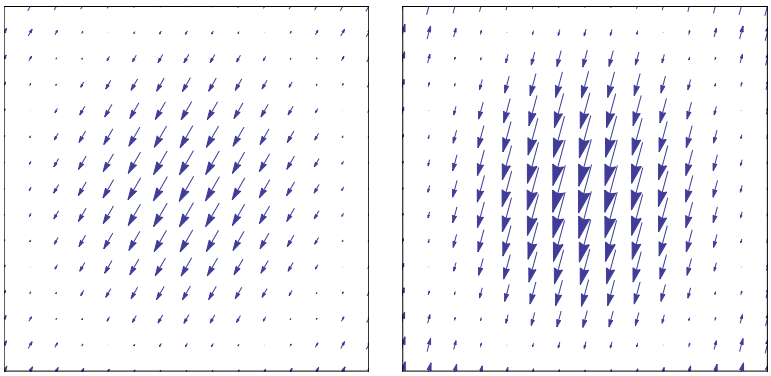

e. $t = \frac{2\pi}{3\omega}$ **f.** $t = \frac{5\pi}{6\omega}$

Figure 4.5 Cross-sectional electric vector field for the $|g_+\rangle$ mode, with the beam propagating out of the page. Length of an arrow represents strength of the E field at that position. Frequencies were $\Omega = 1$ and $\omega = 2$. Frame size is $5/k_r$ on a side, showing the first Bessel zero at $r \approx 2.4/k_r$.

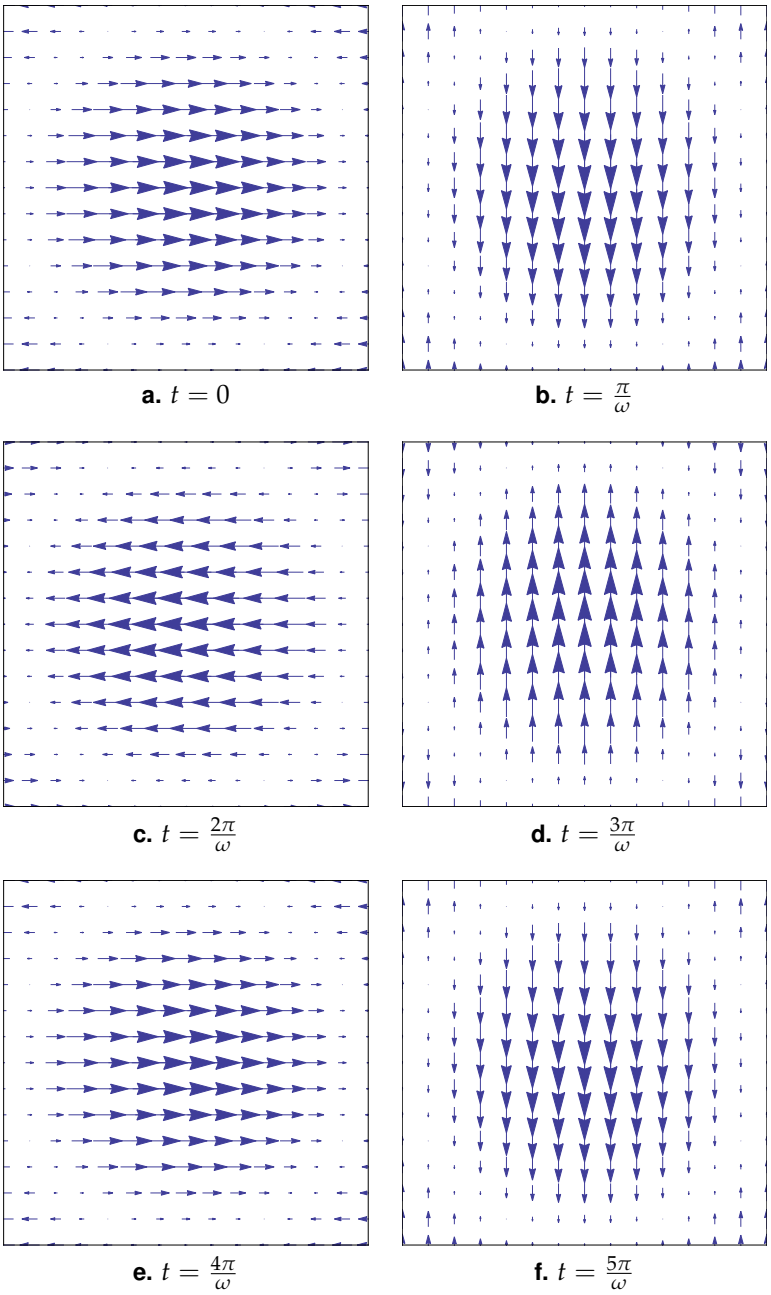

Figure 4.6 Cross-sectional electric vector field for the $|g_+\rangle$ mode, with the beam propagating out of the page. These pictures display successive maxima in the field magnitude (longest arrows). Frequencies were $\Omega = 1$ and $\omega = 2$. Frame size is $5/k_r$ on a side, showing the first Bessel zero at $r \approx 2.4/k_r$.

4.3 Simulating the $|b_{\pm}\rangle$ modes

In the experimental limit of $\omega \gg \Omega$, the $|g_{\pm}\rangle$ modes reduce down to $|b_{\pm}\rangle$,

$$\text{Re}\left[\vec{E}_{b_+}\right] = E(r)\cos(\omega t)\left(\cos\Omega t\,\vec{e}_x + \sin\Omega t\,\vec{e}_y\right) \tag{4.11}$$

$$\text{Re}\left[\vec{E}_{b_-}\right] = E(r)\sin(\omega t)\left(-\sin\Omega t\,\vec{e}_x + \cos\Omega t\,\vec{e}_y\right). \tag{4.12}$$

The $|b_+\rangle$ mode is qualitatively identical to the $|g_+\rangle$ mode, differing only in magnitude. However, for ω values that are much larger than Ω, we lose many of the details we discussed in Section 4.2. As Figure 4.7 shows, we retain the rotation at frequency Ω but the amplitude modulates so quickly that it should be undetectable. Here, we have used frequencies $\Omega = 1$ and $\omega = 20$, but in reality ω should be around 10^{14} Hz. So, to any measurement device (typically on the order of MHz to GHz), this fast modulation at ω looks like instantaneous reversal and the finer details are lost.

As shown in Figure 4.8, the $|b_-\rangle$ mode exhibits glaring differences from the $|g_-\rangle$ mode. This simulation exhibits none of the angular frequency modulation of the $|g_-\rangle$ mode, but it does exhibit amplitude modulation at ω, which, again, is simply rapid reversal in this large ω regime. This behavior is identical to that of the $|b_+\rangle$ mode, but offset by an angle $\pi/2$.

As we derived in Section 3.1.3, both of these modes carry zero spin angular momentum. Where, then, does their overall right-handed rotation come from? We draw inspiration from our discussion of the $|g_+\rangle$ mode, where we discovered that the amplitude modulation at ω caused a sort of left-handed rotation even though the overall polarization vector rotated right-handedly. The $|b_+\rangle$ mode is qualitatively identical to the $|g_+\rangle$ mode, so it should also experience a sort of left-handed rotation due to the amplitude modulation, albeit at much larger values of ω. Furthermore, we see that both of the $|b_{\pm}\rangle$ modes exhibit the same behavior.

In the case of the $|g_+\rangle$ mode, the left-handed rotation overpowered the right-handed rotation at Ω. It may not be that much of a stretch to infer that in the case of equal superpositions, the angular momentum contributions from the two competing rotations cancel out, resulting in zero angular momentum overall.

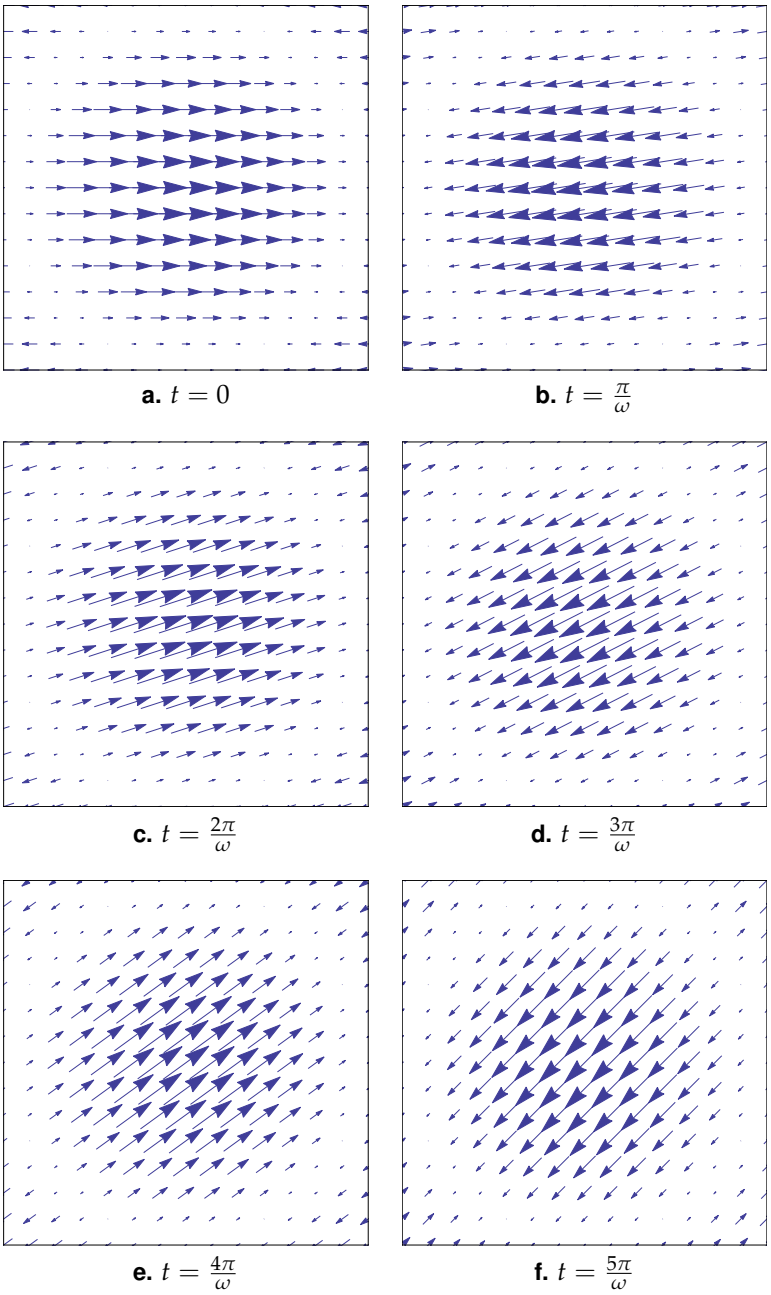

Figure 4.7 Cross-sectional electric vector field for the $|b_{+}\rangle$ mode, with the beam propagating out of the page. We show the field only at times when the magnitude is maximized. Frequencies used were $\Omega = 1$ and $\omega = 20$. Frame size is $5/k_r$ on a side, showing the first Bessel zero at $r \approx 2.4/k_r$.

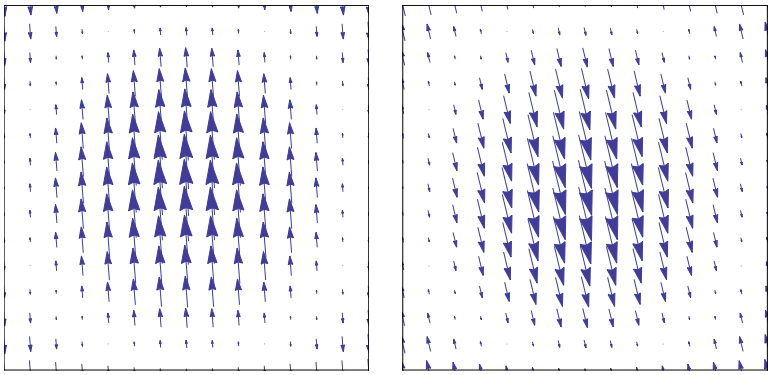

a. $t = \frac{\pi}{2\omega}$ **b.** $t = \frac{3\pi}{2\omega}$

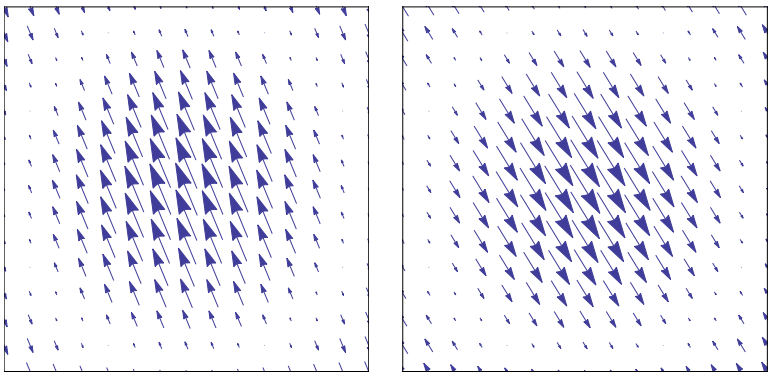

c. $t = \frac{5\pi}{2\omega}$ **d.** $t = \frac{7\pi}{2\omega}$

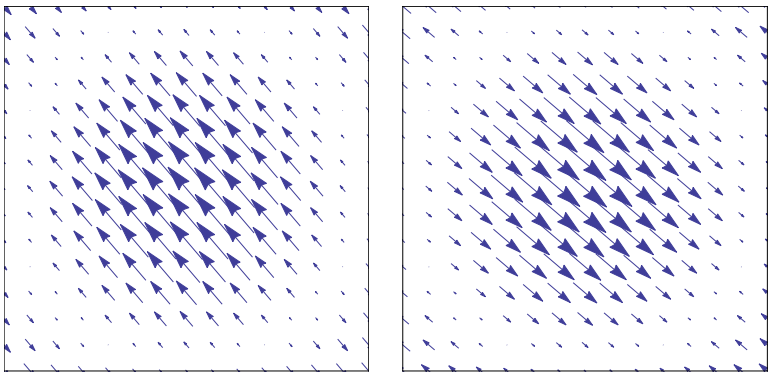

e. $t = \frac{9\pi}{2\omega}$ **f.** $t = \frac{11\pi}{2\omega}$

Figure 4.8 Cross-sectional electric vector field for the $|b_-\rangle$ mode, with the beam propagating out of the page. We show the field only at times when the magnitude is maximized. Frequencies used were $\Omega = 1$ and $\omega = 20$. Frame size is $5/k_r$ on a side, showing the first Bessel zero at $r \approx 2.4/k_r$.

4.4 Simulating the $|h_-\rangle$ mode

From Section 3.2.2, the real electric field expression for the $|h_-\rangle$ mode is given as

$$\begin{aligned}\mathrm{Re}\left[\vec{E}_{h_-}\right] = \sqrt{2}\,E(r)\,\vec{e}_s\big(&\cos^2\theta\cos\left[\ell\phi-(\omega+\ell\Omega)\,t\right]\\ &-\sin^2\theta\cos\left[\ell\phi+(\omega-\ell\Omega)\,t\right]\big).\end{aligned} \tag{4.13}$$

And from our calculations in Section 3.1.2, recall that the $|h_-\rangle$ mode carries positive orbital angular momentum, so its field distribution pattern should exhibit right-handed rotation. This equation is not very intuitive or transparent, so we jump straight into the modeling. We first simulate these equations with `VectorPlot`, forcing them to take on a horizontal polarization $\vec{e}_x$. The areas of positive electric field should point rightwards while negative electric field corresponds to leftwards-pointing vectors. Then, we will use `ParametricPlot3D` to visualize the same situation.

Figure 4.9 shows a transverse slice of the real electric field at $z = 0$, with frequencies $\Omega = 1$ and $\omega = 2$. The region of high positive field amplitude is colored red. The amplitude pattern revolves around the propagation axis in a right-handed manner, matching the sign of the OAM that the mode carries. Note that the amplitude modulates as well, as does the angular frequency. If we take for visual reference the line between the two lobes where $E = 0$, then we see that from (a) to (c), this zero field line rotates by just over $\pi/2$. Over the same time difference of $\frac{\pi}{2\omega}$ from (c) to (e), this line clearly rotates under $\pi/2$. We further note that over the section from (a) to (c), the magnitude of the field is low. In the section from (c) to (e), the magnitude of the field is high. Thus, times of high field magnitude correspond to low angular velocity, and vice versa.

This is the OAM analogue to what we saw for the $|g_-\rangle$ mode in Figure 4.3 and the corresponding discussion. However, unlike for the $|g_-\rangle$ mode, here it is much more difficult to track the angular frequency as a function of time, so we have not been able to produce a graph similar to Figure 4.4 for $|h_-\rangle$. For spin angular momentum, we take the derivative of the angle of the polarization vector to get the angular velocity/frequency. Here, we have to track the regions of high and low field as they revolve around the axis, which is significantly harder to do within Mathematica. Future work could finish this plot, and we predict it will look similar to Figure 4.4.

The field amplitude distribution is plotted using `ParametricPlot3D` in Figure 4.10, and it shows the same behavior. The positive amplitude lobe rising up near the center corresponds to the red lobe in Figure 4.9.

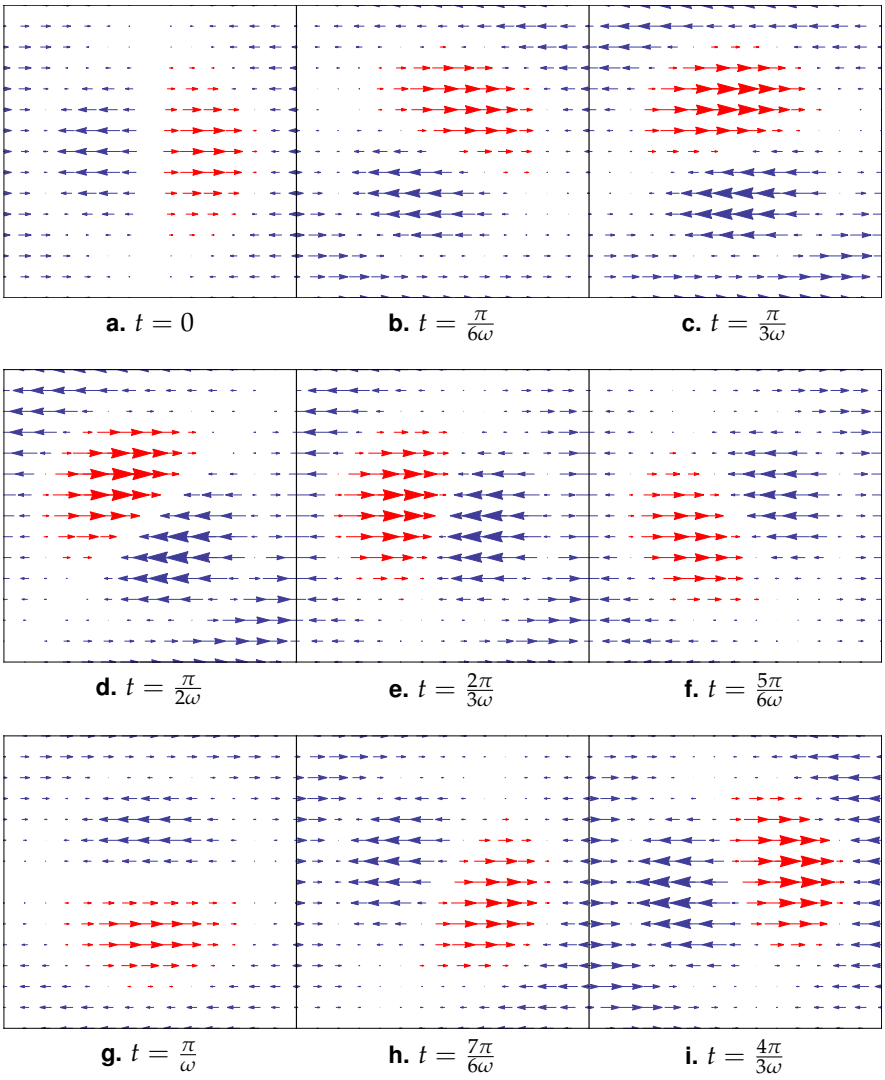

Figure 4.9 Cross-sectional electric vector field for the $|h_-\rangle$ mode at $z = 0$, with the beam propagating out of the page. Positive lobe ($E > 0$) is colored red. Frequencies used were $\Omega = 1$ and $\omega = 2$. The nine pictures are separated by equal timesteps of $\frac{\pi}{6\omega}$. Frame size is $5/k_r$ on each side.

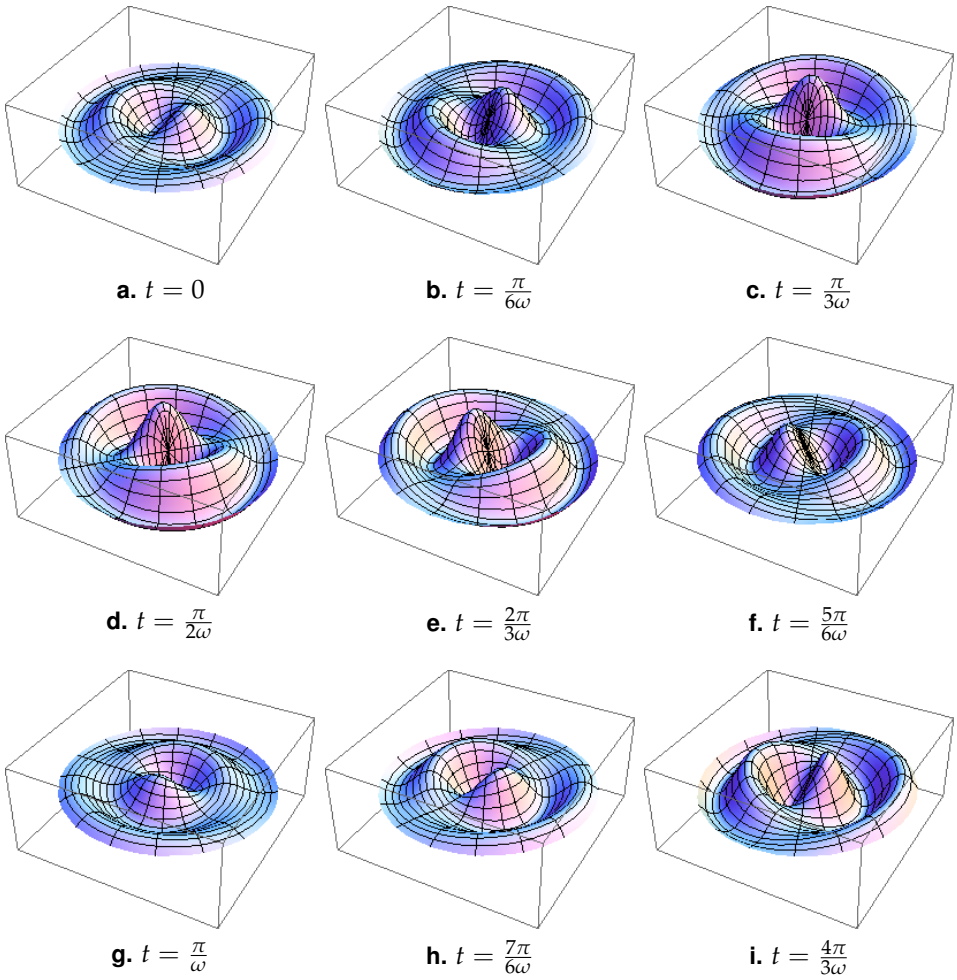

Figure 4.10 Plots of field amplitude distribution for the $|h_+\rangle$ mode, with the beam propagating upwards. Frequencies used were $\Omega = 1$ and $\omega = 2$. The nine pictures are separated by equal timesteps of $\frac{\pi}{6\omega}$. Radius goes out to $10/k_r$ so that the frame size is $20/k_r$ on a side.

4.5 Simulating the $|h_+\rangle$ mode

The real electric field expression we derived for the frequency-dependent $|h_+\rangle$ mode is given as

$$\mathrm{Re}\left[\vec{E}_{h_+}\right] = 2\sqrt{2}\, E(r)\, \vec{e}_s \cos(\omega t) \cos\theta \sin\theta \cos\left[\ell\,(\phi - \Omega t)\right]. \tag{4.14}$$

From this equation, we can see slow rotation at Ω, as well as an overall amplitude modulation at ω. The $\ell\phi$ term in the cosine serves to split up our transverse mode profile into two lobes. Recall that the orbital angular momentum carried by the $|h_+\rangle$ mode is negative, and thus the field amplitude distribution should rotate left handedly about the propagation axis.

Figure 4.11 shows the behavior of $|h_+\rangle$ for frequencies $\Omega = 1$ and $\omega = 2$. The field amplitude pattern rotates right-handedly at Ω, against the left-handed rotation that would be expected from the negative OAM that the state carries. We note that the amplitude oscillates at ω from the $\cos(\omega t)$ term in Equation 4.14. This sort of behavior is reminiscent of the amplitude modulation of the frequency-dependent spin superposition $|g_+\rangle$. Like with the $|g_+\rangle$ mode, here we see that the faster amplitude modulation produces a sort of left-handed rotation. In Figure 4.11(b), the positive lobe (red) is centered just about the horizontal axis on the right. After the amplitude modulation in Figure 4.11(f), the positive lobe is now located at an angle $\pi/2$ left rotated away from its position in (b).

Figure 4.12 shows this more clearly with successive maxima in the norm of the field. The positive field amplitude lobe is colored red, and we see that the fast amplitude oscillations cause this red lobe to revolve left-handedly. This is the OAM analogue of Figure 4.6 with the $|g_+\rangle$ mode, and our conclusions are the same. While the overall rotation of the field amplitude pattern is right handed, the motion of the individual positive/negative lobes exhibits some left-handed motion. It could be the case that this left-handed motion overpowers the slow right-handed motion at Ω, resulting in the overall negative orbital angular momentum.

Figures 4.13 and 4.14 show the analogous plots with `ParametricPlot3D`. Figure 4.13 shows plots of the amplitude of Equation 4.14 as a function of time. Like Figure 4.11, we see that the state rotates right-handedly at Ω while the amplitude varies at ω. Successive maxima in the field amplitude are shown in Figure 4.14. The highest lobe in the center of these plots is a positive region of high electric field amplitude, corresponding roughly to the red region marked in Figure 4.12. Tracking this lobe across several maxima, we see an overall left-handed rotation.

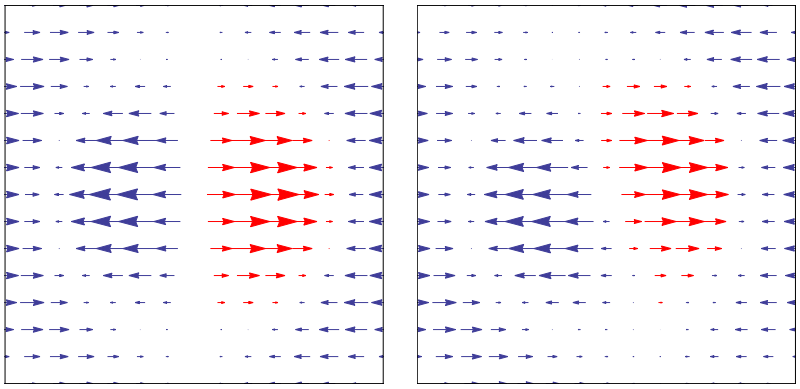

a. $t = 0$

b. $t = \frac{\pi}{6\omega}$

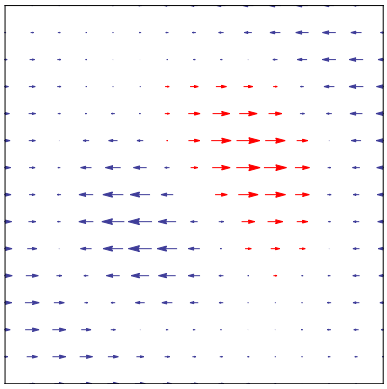

c. $t = \frac{\pi}{3\omega}$

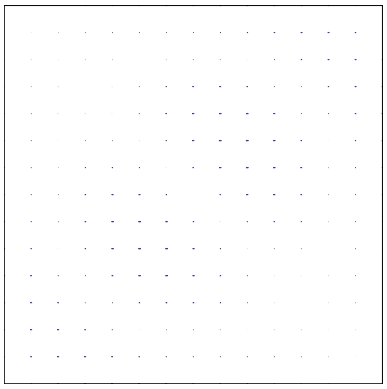

d. $t = \frac{\pi}{2\omega}$

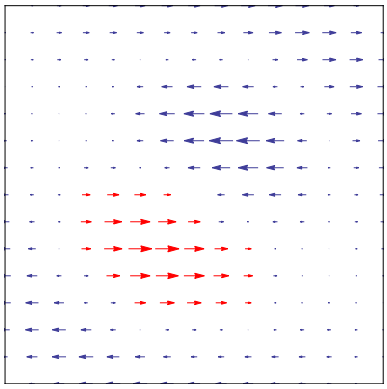

e. $t = \frac{2\pi}{3\omega}$

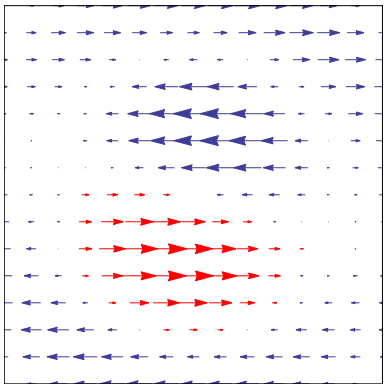

f. $t = \frac{5\pi}{6\omega}$

Figure 4.11 Cross-sectional electric vector field for the $|h_+\rangle$ mode, with the beam propagating out of the page. Length of an arrow represents strength of the E field at that position. Positive lobe ($E > 0$) is colored red. Frequencies were $\Omega = 1$ and $\omega = 2$. Frame size is $10/k_r$ on a side, showing the first Bessel zero for $\ell = 1$ at $r \approx 3.8/k_r$.

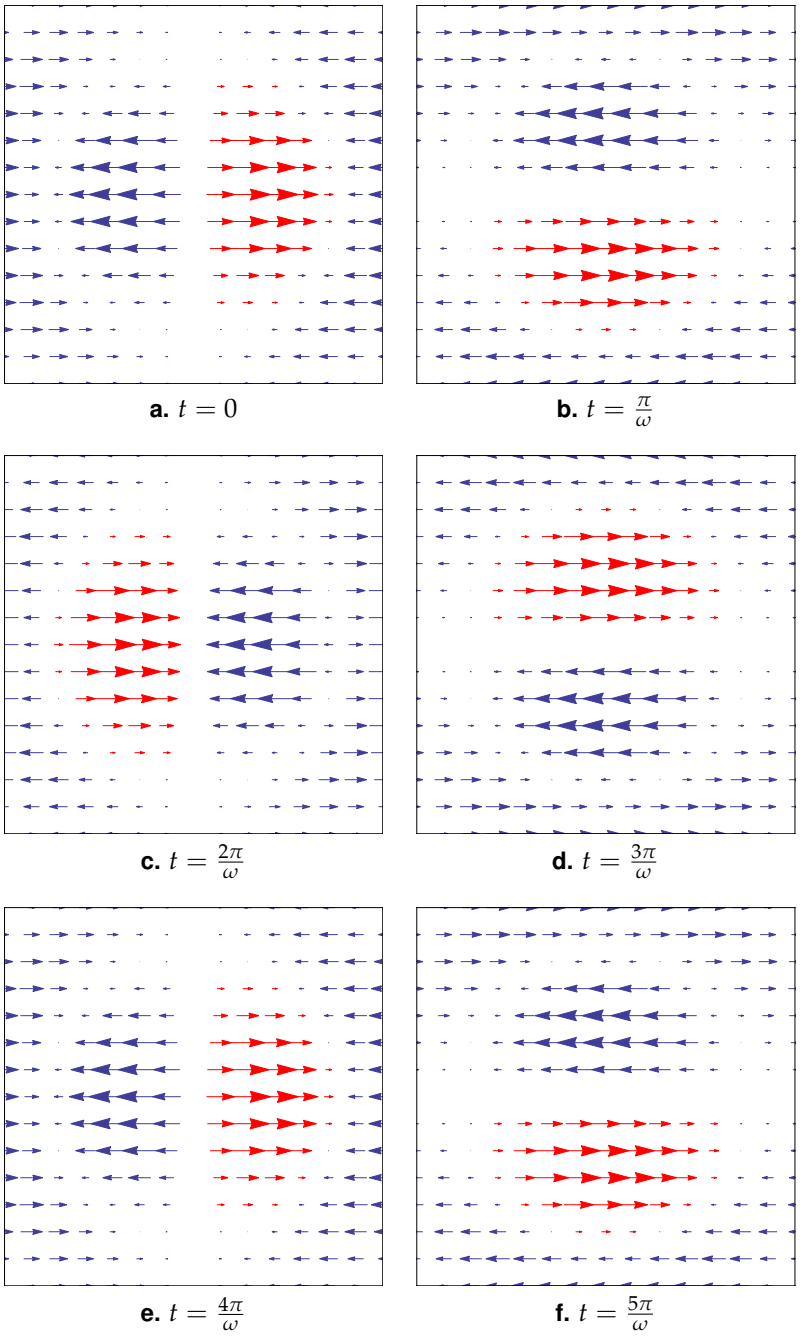

a. $t = 0$ **b.** $t = \frac{\pi}{\omega}$

c. $t = \frac{2\pi}{\omega}$ **d.** $t = \frac{3\pi}{\omega}$

e. $t = \frac{4\pi}{\omega}$ **f.** $t = \frac{5\pi}{\omega}$

Figure 4.12 Cross-sectional electric vector field for the $|h_+\rangle$ mode, with the beam propagating out of the page. These pictures display successive maxima in the field magnitude (longest arrows). Positive lobe ($E > 0$) is colored red. Frequencies were $\Omega = 1$ and $\omega = 2$, and frame size is $10/k_r$ on a side, showing the first Bessel zero for $\ell = 1$ at $r \approx 3.8/k_r$.

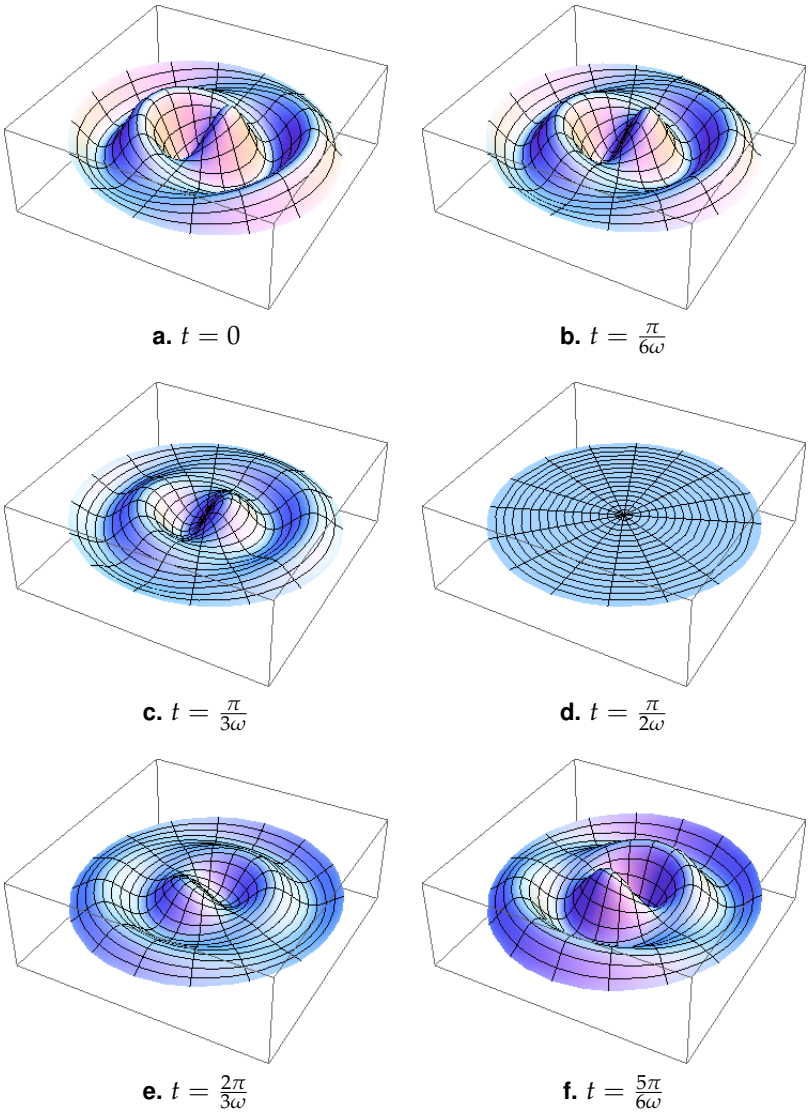

a. $t = 0$ **b.** $t = \frac{\pi}{6\omega}$

c. $t = \frac{\pi}{3\omega}$ **d.** $t = \frac{\pi}{2\omega}$

e. $t = \frac{2\pi}{3\omega}$ **f.** $t = \frac{5\pi}{6\omega}$

Figure 4.13 Plots of field amplitude distribution for the $|h_+\rangle$ mode, with the beam propagating upwards. Frequencies used were $\Omega = 1$ and $\omega = 2$. Radius extends out to $11/k_r$, showing the first three Bessel zeroes for $\ell = 1$.

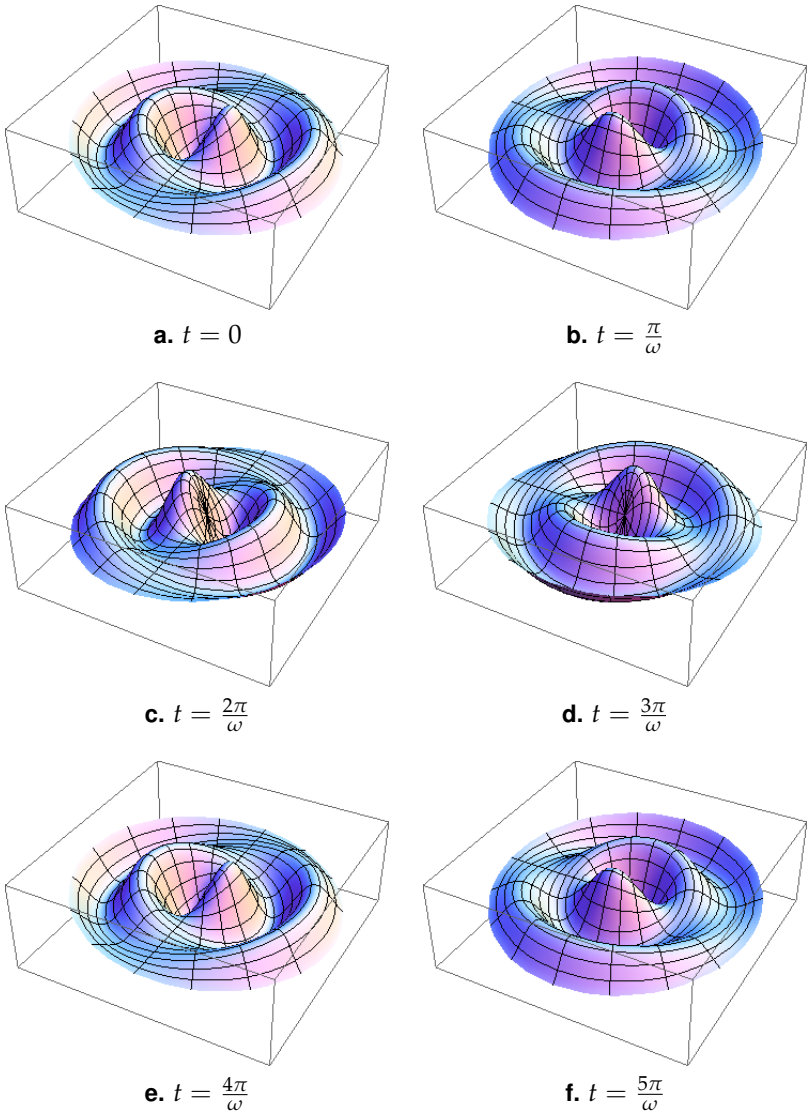

a. $t = 0$ **b.** $t = \frac{\pi}{\omega}$

c. $t = \frac{2\pi}{\omega}$ **d.** $t = \frac{3\pi}{\omega}$

e. $t = \frac{4\pi}{\omega}$ **f.** $t = \frac{5\pi}{\omega}$

Figure 4.14 Plots of field amplitude distribution for the $|h_+\rangle$ mode, with the beam propagating upwards. These pictures display successive maxima in the field magnitude. Frequencies used were $\Omega = 1$ and $\omega = 2$. Radius extends out to $11/k_r$, showing the first three Bessel zeroes for $\ell = 1$.

4.6 Simulating the $|c_\pm\rangle$ modes

In the experimental limit of $\omega \gg \Omega$, the $|h_\pm\rangle$ OAM superpositions become $|c_\pm\rangle$, with real electric field expressions

$$\mathrm{Re}\left[\vec{E}_{c_+}\right] = \sqrt{2}\, E(r)\, \vec{e}_s \cos(\omega t) \cos\left[\ell\,(\phi - \Omega t)\right] \tag{4.15}$$

$$\mathrm{Re}\left[\vec{E}_{c_-}\right] = \sqrt{2}\, E(r)\, \vec{e}_s \sin(\omega t) \sin\left[\ell\,(\phi - \Omega t)\right]. \tag{4.16}$$

As with the $|b_\pm\rangle$ modes, we expect to see both $|c_+\rangle$ and $|c_-\rangle$ rotating in the same direction, and only offset by some phase. Figure 4.15 shows a transverse slice of the real electric field of $|c_+\rangle$ at $z = 0$, where the polarization is forced to be horizontal. Frequencies used were $\Omega = 1$ and $\omega = 20$. Here, we show successive maxima, as the $\cos(\omega t)$ term causes extremely fast oscillation that makes it hard to tell what is going on. We can see that the pattern rotates right-handedly, and the positive lobe starts on the right side.

Figure 4.16 shows the same situation, but for the $|c_-\rangle$ mode. We see that it, too, rotates right-handedly. However, the positive amplitude lobe reaches its first maximum at $\frac{\pi}{2\omega}$, and here it is at the top. Thus we clearly see that $|c_-\rangle$ is simply the $|c_+\rangle$ mode, but with a phase shift of $\frac{\pi}{2\omega}$. This is analogous to the behavior of the $|b_\pm\rangle$ modes.

Figures 4.18 and 4.17 show the same behavior, but as a 3D surface using `ParametricPlot3D`.

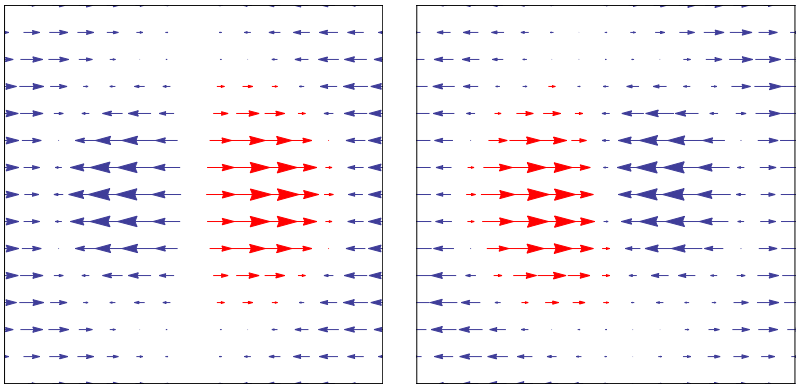

a. $t = 0$

b. $t = \frac{\pi}{\omega}$

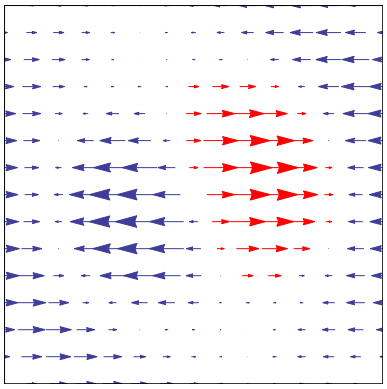

c. $t = \frac{2\pi}{\omega}$

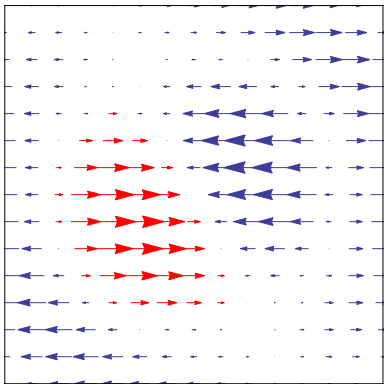

d. $t = \frac{3\pi}{\omega}$

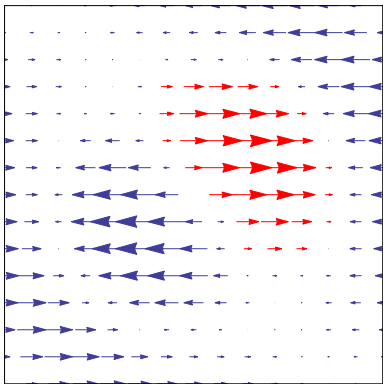

e. $t = \frac{4\pi}{\omega}$

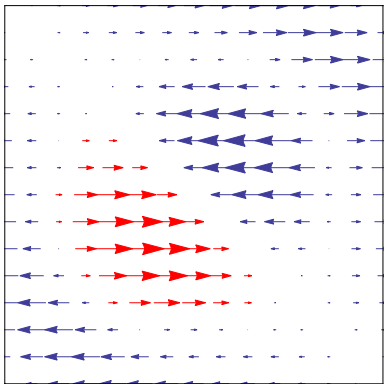

f. $t = \frac{5\pi}{\omega}$

Figure 4.15 Cross-sectional electric vector field for the $|c_+\rangle$ mode, with the beam propagating out of the page. We show the field only at times when the magnitude is maximized. Positive lobe ($E > 0$) is colored red. Frequencies used were $\Omega = 1$ and $\omega = 20$. Frame size is $5/k_r$ on a side, showing the first Bessel zero at $r \approx 2.4/k_r$.

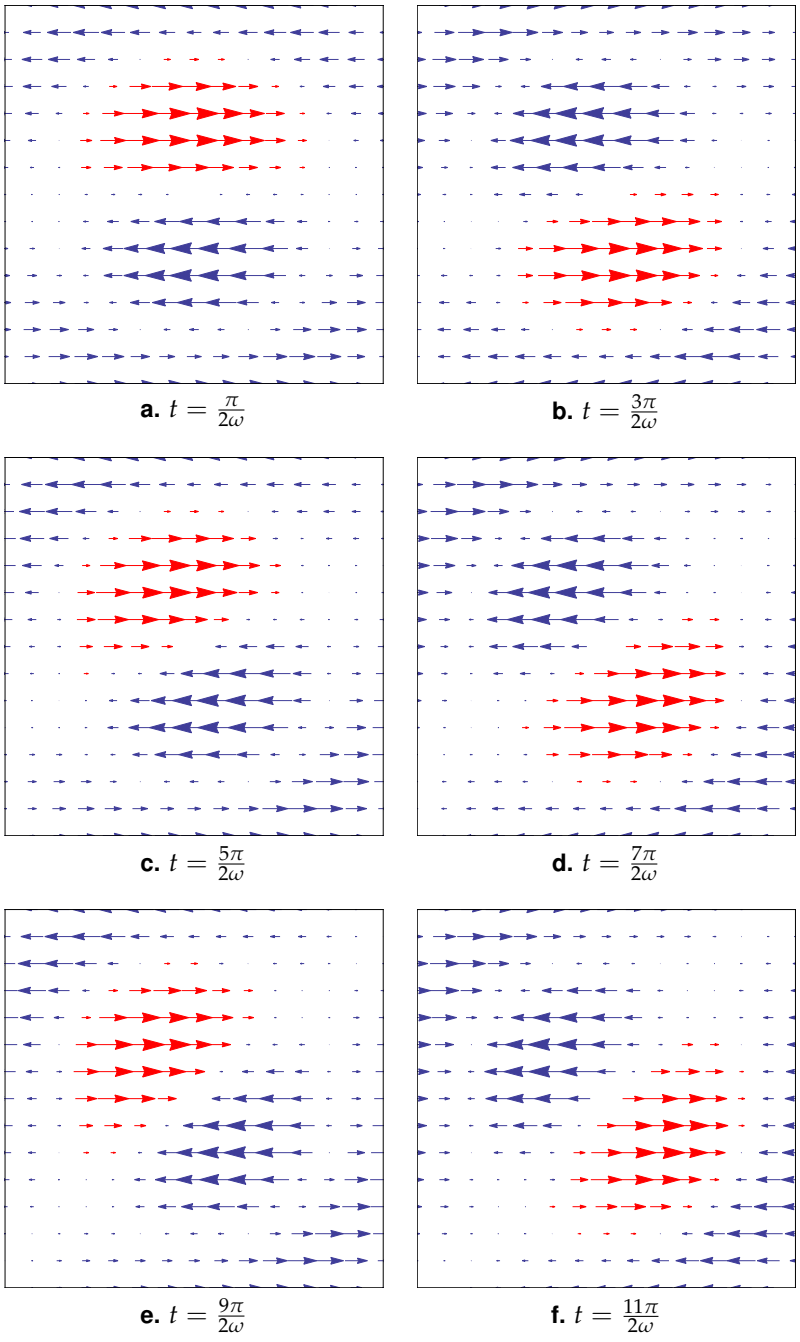

Figure 4.16 Cross-sectional electric vector field for the $|c_{-}\rangle$ mode, with the beam propagating out of the page. We show the field only at times when the magnitude is maximized. Positive lobe ($E > 0$) is colored red. Frequencies used were $\Omega = 1$ and $\omega = 20$. Frame size is $5/k_r$ on a side, showing the first Bessel zero at $r \approx 2.4/k_r$.

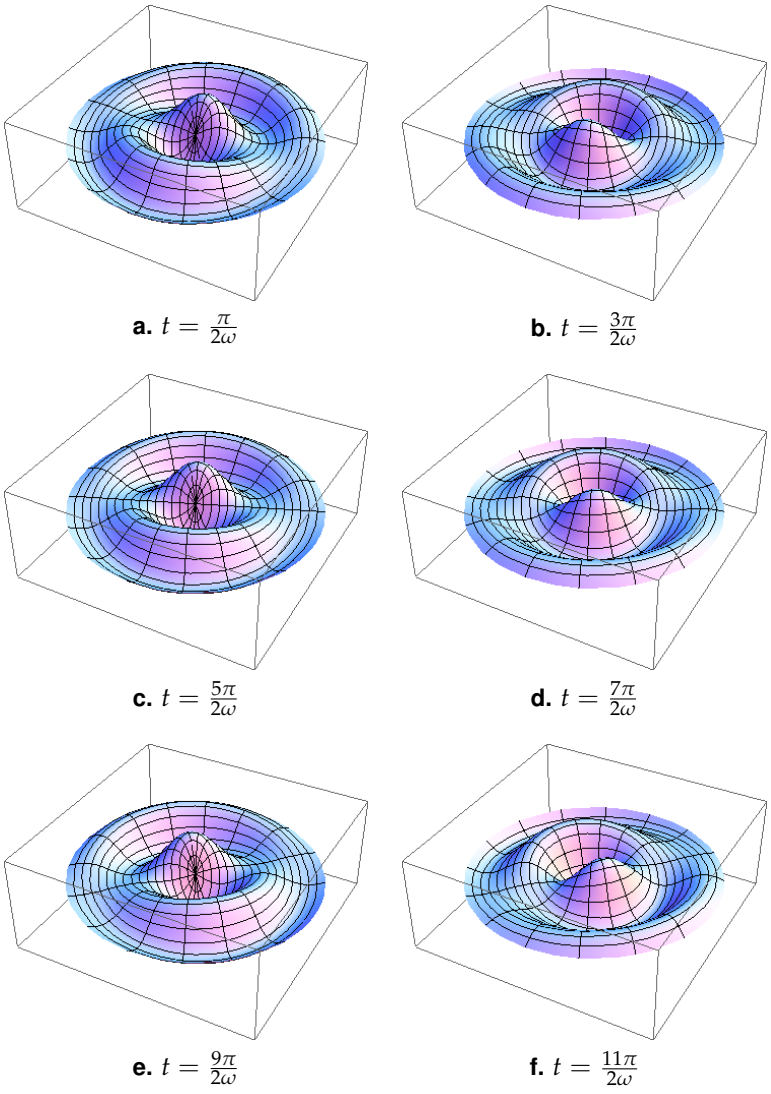

a. $t = \frac{\pi}{2\omega}$ **b.** $t = \frac{3\pi}{2\omega}$

c. $t = \frac{5\pi}{2\omega}$ **d.** $t = \frac{7\pi}{2\omega}$

e. $t = \frac{9\pi}{2\omega}$ **f.** $t = \frac{11\pi}{2\omega}$

Figure 4.17 Plots of field amplitude distribution for the $|c_+\rangle$ mode, with the beam propagating upwards. We show the field only at times when the magnitude is maximized. Frequencies used were $\Omega = 1$ and $\omega = 20$. Radius extends out to $10/k_r$, showing the first two Bessel zeroes for $\ell = 1$.

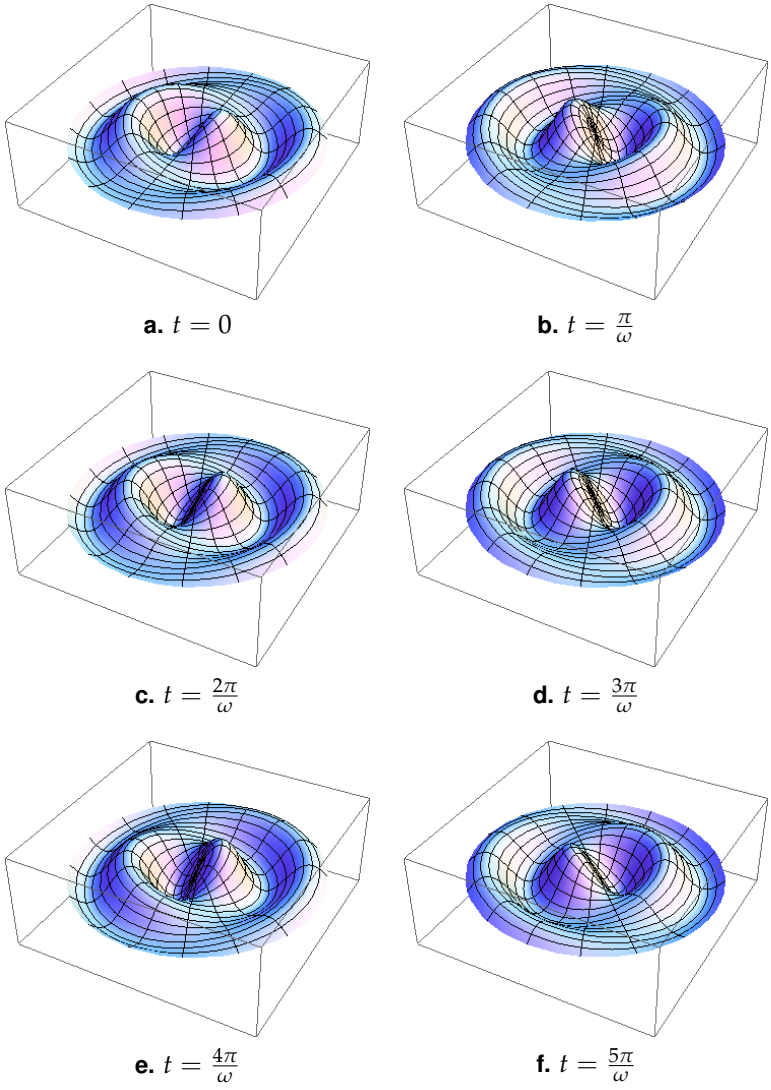

a. $t = 0$ **b.** $t = \frac{\pi}{\omega}$

c. $t = \frac{2\pi}{\omega}$ **d.** $t = \frac{3\pi}{\omega}$

e. $t = \frac{4\pi}{\omega}$ **f.** $t = \frac{5\pi}{\omega}$

Figure 4.18 Plots of field amplitude distribution for the $|c_{+}\rangle$ mode, with the beam propagating upwards. We show the field only at times when the magnitude is maximized. Frequencies used were $\Omega = 1$ and $\omega = 20$. Radius extends out to $10/k_r$, showing the first two Bessel zeroes for $\ell = 1$.

Chapter 5

Experimental Work

Susanna Todaro (HMC '12) began work on experimental generation and observation of the $|b_{\pm}\rangle$ mode with a rotating half-wave plate (HWP). In this chapter, we will derive how this rotating HWP can generate one of these equal spin superpositions. Then, we will go on to review results from Susanna's work, and present results from an updated experimental setup.

Creating the $|c_{\pm}\rangle$ modes requires more sophisticated optics and laser modes, and in this year of research we did not acquire these tools necessary to make these OAM superpositions. We will discuss multiple methods of generating and measuring the $|c_{\pm}\rangle$ modes in Chapter 6.

5.1 Generation of $|b_{\pm}\rangle$

Figure 5.1 depicts a simplified version of the experimental setup used to create and detect the $|b_{+}\rangle$ mode. Our Helium-Neon laser output has wavelength 633nm and is horizontally polarized. We send this beam through

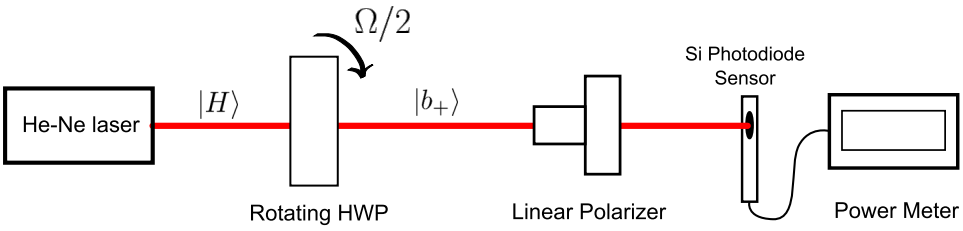

Figure 5.1 Experimental setup used to create and detect the $|b_{+}\rangle$ mode.

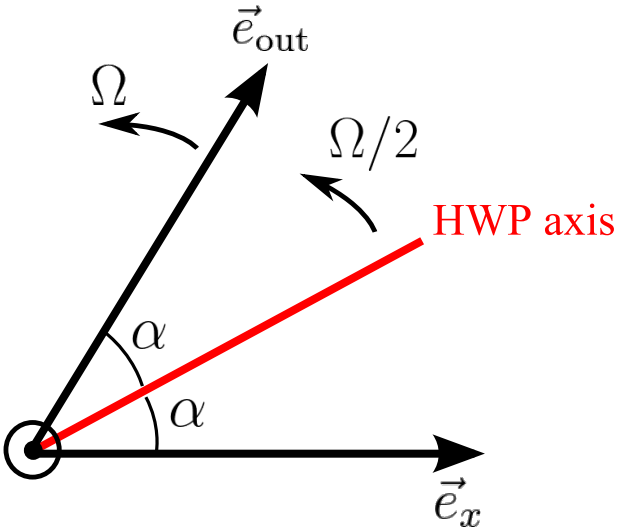

Figure 5.2 Face of half-wave plate showing input and output polarization vectors on top of the HWP axis. Beam propagates out of the page.

a rotating 633nm HWP, as shown in Figure 5.2. This figure shows the polarization directly before and after the HWP, with the beam propagating out of the page (as indicated by the circle with a dot). On this plot, a right circularly polarized beam would rotate counterclockwise. Here, we set the HWP to rotate counterclockwise/right-handedly at angular frequency $\Omega/2$.

The input horizontal polarization is given in polarization vector notation as

$$\vec{e}_x = \frac{1}{\sqrt{2}} \left(\vec{e}_+ + \vec{e}_- \right). \tag{5.1}$$

A half-wave plate provides a π phase shift between the polarization components aligned along its axis and perpendicular to its axis. For an input linear polarization, this has the effect of flipping the polarization vector across the HWP axis. Thus if the HWP were stationary and its axis were at an angle α above the horizontal, the output state would be flipped to 2α,

$$\vec{e}_{\text{out}} = \cos(2\alpha)\vec{e}_x + \sin(2\alpha)\vec{e}_y. \tag{5.2}$$

To insert HWP rotation, we simply let $\dot{\alpha} = \Omega/2$ so that $\alpha = \frac{1}{2}\Omega t$. Then, the output state becomes

$$\vec{e}_{\text{out}} = \cos(\Omega t)\vec{e}_x + \sin(\Omega t)\vec{e}_y \tag{5.3}$$

where we can draw from Equations 2.5 and 2.6 to write out $\vec{e}_x$ and $\vec{e}_y$ in the ($\vec{e}_+$,$\vec{e}_-$) basis. This yields

$$\vec{e}_{\text{out}} = \cos(\Omega t)\frac{1}{\sqrt{2}}\left(\vec{e}_+ + \vec{e}_-\right) + \sin(\Omega t)\left(-\frac{i}{\sqrt{2}}\right)\left(\vec{e}_+ - \vec{e}_-\right) \tag{5.4}$$

$$= \frac{1}{\sqrt{2}}\left(e^{-i\Omega t}\vec{e}_+ + e^{i\Omega t}\vec{e}_-\right). \tag{5.5}$$

This expression by itself may not immediately resemble the $|b_+\rangle$ mode, but if we plug this into Equation 3.22, then we get the complex electric field of the beam output from the rotating HWP. Here, as always, we take $\ell = 0$ to focus solely on spin angular momentum and we take $z = 0$ to get the behavior at a transverse slice, yielding

$$\vec{E}_{\text{out}} = E(r)e^{-i\omega t}\vec{e}_{\text{out}} \tag{5.6}$$

$$= \frac{1}{\sqrt{2}}E(r)e^{-i(\omega+\Omega)t}\vec{e}_+ + \frac{1}{\sqrt{2}}E(r)e^{-i(\omega-\Omega)t}\vec{e}_- \tag{5.7}$$

$$= \frac{1}{\sqrt{2}}\vec{E}_{\omega+\Omega,\,\ell=0,\,s=1} + \frac{1}{\sqrt{2}}\vec{E}_{\omega-\Omega,\,\ell=0,\,s=-1} \tag{5.8}$$

where in the last step we have noticed that the two terms are simply complex electric fields themselves with opposite values of spin angular momentum. The right circularly polarized term ($s = 1$) is frequency shifted upwards by Ω and the left circularly polarized term ($s = -1$) is frequency shifted down by Ω. But this is simply the definition of the $|b_+\rangle$ mode we constructed, so we have created the $|b_+\rangle$ mode.

Similarly, the $|b_-\rangle$ mode can be created with an incident vertical polarization instead of the horizontal polarization used here. Because the methods used to generate the $|b_+\rangle$ and $|b_-\rangle$ modes are so similar, we can see that the two must essentially be the same, separated by only a phase shift. [1]

5.2 Detection of $|b_\pm\rangle$

To detect the rotating spin superpositions, we use a linear polarizer followed by a silicon photodiode sensor (Thorlabs S130C) hooked up to a power meter (Thorlabs PM100D), as shown in Figure 5.1. This projects the polarization vector onto a specific linear polarization, and then measures the power/intensity averaged over some small time bin.

If we rotate the linear polarizer to transmit only horizontally polarized light, then we can easily calculate the expected intensity as a function of

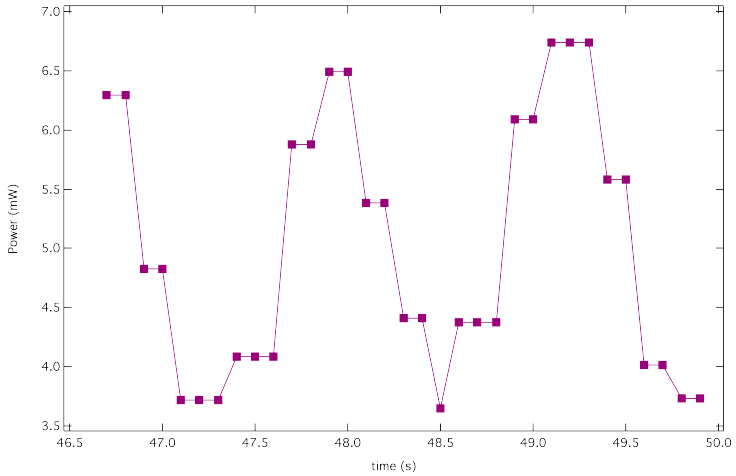

Figure 5.3 Data taken by Susanna Todaro HMC '12 of the $|b_+\rangle$ mode, with the HWP rotating at 0.33Hz within the Newport Rotator.

time. We can project the output polarization state of Equation 5.3 onto the horizontal, yielding

$$\vec{E}_{\text{after polarizer}} \propto \vec{e}_{\text{after HWP}} \cdot \vec{e}_x = \cos(\Omega t).$$

Then, we obtain the intensity by simply squaring this,

$$I_{\text{after polarizer}} \propto \cos^2(\Omega t).$$

If we have a HWP rotating at a frequency f (where $2\pi f = \frac{1}{2}\Omega$), then the function we should use to fit the resultant curve is given by

$$I_{\text{fit}}(t) = A * \cos^2(4\pi f t + \varphi) + y_0. \tag{5.9}$$

5.2.1 Discrete Steps: Revising the Setup

Initially, Susanna tried using the software that came with our power meter. That is, the silicon photodiode sensor directly measured the power, outputting a current that transferred to the power meter. The power meter then converted the analog current signal to a digital signal which it could manipulate and send on to the computer via USB. And for reference, Susanna was using a Newport motor attached to a rotating mount (Newport NSR-1 Rotator), in which we placed the HWP.

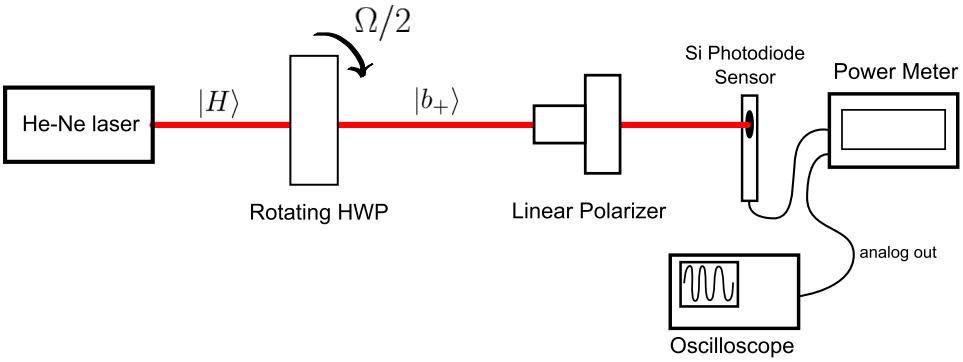

Figure 5.4 Revised experimental setup used to create and detect the $|b_+\rangle$ mode, without discrete steps in resultant data.

Figure 5.3 shows power data that Susanna took for the $|b_+\rangle$ mode, a far cry from the continuous signal we would have expected. Clearly, some aspect of the setup was at fault. In her thesis, Susanna argues that "the discrete nature of the wave plate rotation makes it impossible to produce a smoothly rotating mode." [3] She argues that because the rotation mount was designed for precision optics and not continuous rotation, the HWP is rotated between discrete steps, producing the discrete signal of Figure 5.3. Furthermore, the Newport rotating mount was limited to frequencies under 1 Hz. Thus, Susanna and I decided to get the Harvey Mudd machinist, Paul Stovall, to help us build a rotation mount that could achieve faster, continuous rotation. A photo of this mount and motor, which we will call the Stovall Rotator, is shown in Figure 5.5. Because the HWP needed to be in the center of the mount, I designed the mount so that the motor would be on the side, and a belt would drive the rotation of the HWP. The motor can spin the HWP at dozens of Hz, but is controlled by a dial with arbitrary numbers. Thus to figure out the rotation frequency compared to the dial values, we measured the rotation of the $|b_+\rangle$ mode as described above. Results from these measurements are described in Section 5.3.

However, it turns out that the Newport Rotator was not at fault. Instead, the Analog-Digital Converter (ADC) within the power meter sampled too slowly, producing discrete results. To circumvent this, we took the "Analog Out" port of the power meter and hooked that up to an oscilloscope (Agilent DSO 3102) to see the current output from the silicon photodiode directly. This signal was then obtained from the oscilloscope using the corresponding software (3000 Series Connect Software). This new setup is depicted in Figure 5.4, and results using it are discussed below.

Figure 5.5 A photo of the new rotation mount and motor designed by me and built by Paul Stovall. A half-wave plate is placed inside the mount, and rubber pads are placed beneath to isolate the motor-induced vibrations from the rest of the optics table.

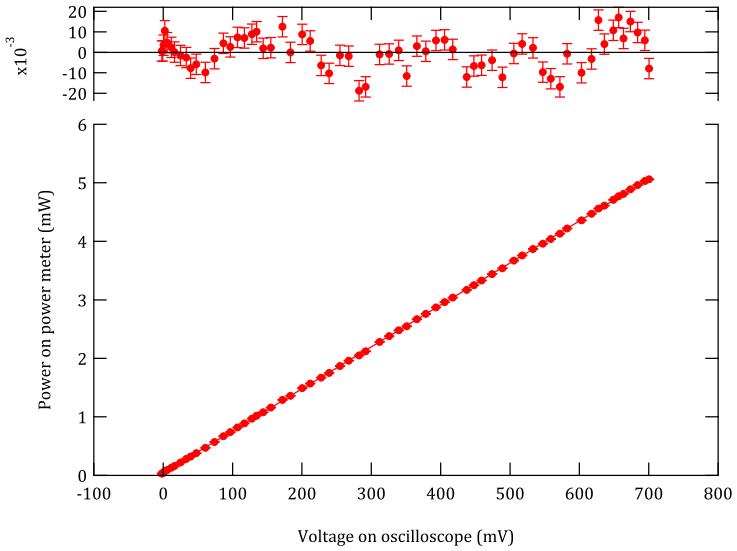

Figure 5.6 Power measured on power meter versus voltage measured on oscilloscope, fit to a line. Fitted equation is $P = 0.044 + \frac{1}{139.4}V$ with a χ^2 per degree of freedom of 2.72.

5.2.2 Correcting the Analog Output

With the new experimental setup, the oscilloscope receives the analog output from the power meter, which is the unaltered signal from the Si photodiode sensor. While we avoid the ADC of the power meter, we also lose the power meter's ability to convert from the photodiode output into power. Thus, the oscilloscope shows a voltage reading from 0V to 0.7V for the power meter's reading of 0mW to just over 5mW for our laser.

The power meter documentation provides the Analog Output Gain (pg. 68 of the PM 100D manual) in units of volts per amp. For our current range, this value is $4 \times 10^2 \text{V/A}$. The Si photodiode sensor documentation provides a plot of the responsitivity as a function of wavelength in units of amps per watt. A rough estimation gives $3.5 \times 10^{-1} \text{A/W}$. Then, we can write the relation between the voltage measured on the oscilloscope and the power observed on the power meter as

$$\begin{aligned} \text{Measured Power (W)} &= \frac{\text{Measured Voltage (V)}}{(4 \times 10^2\,\text{V/A})(3.5 \times 10^{-1}\,\text{A/W})} \\ &= \frac{1}{140}\,\text{Measured Voltage (V)}. \end{aligned} \tag{5.10}$$

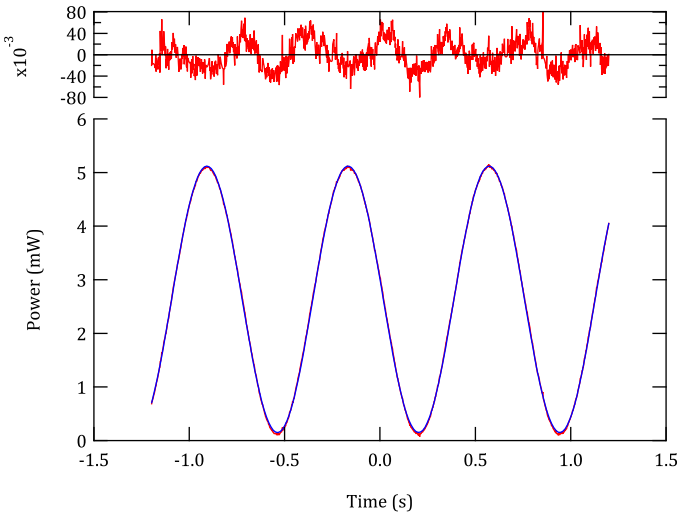

Figure 5.7 Power data measured from the $|b_+\rangle$ mode with the HWP inside the Newport Rotator, rotating at 0.338Hz (150 full-steps/s). The fit used to determine this frequency is described by Equation 5.9. The fit is in blue, on top of the red data. Residuals are plotted above.

However, because of the inaccurate reading of the responsivity, experimentally measuring the voltage and corresponding power gives a more accurate relation. Figure 5.6 shows a plot of power on power meter vs. voltage on oscilloscope. The intensity of the beam incident on the Si sensor was varied with a linear polarizer. The C parameter in the fit is very close to the value 140 we calculated in Equation 5.10.

5.3 Results

5.3.1 Newport Rotator Data: Exploring the $|b_\pm\rangle$ Modes

Using the new setup and recording data through the oscilloscope, we ran this experiment using both the Newport Rotator and the new "Stovall rotator." Figure 5.7 shows data taken using the Newport Rotator, set to rotate at "150 full-steps per second," which is Newport's own unit system. To

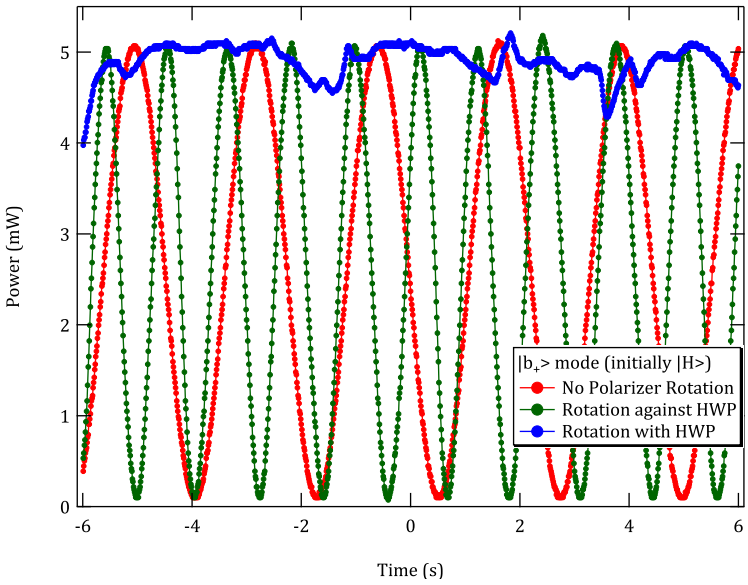

Figure 5.8 Power data for $|b_+\rangle$ mode, with HWP in Newport Rotator rotating at ~ 0.112Hz. The linear polarizer was stationary (red), rotated right-handedly (blue), and rotated left-handedly (green). Linear polarizer was rotated by hand near the target frequency of 0.224Hz. Red and green curves are fitted to $\sin^2$, giving frequencies 0.224Hz (red) and 0.425Hz (green).

determine this frequency, I fit the data to Equation 5.9, which produced the frequency value 0.338Hz. This is the data set that Susanna was trying to produce in Figure 5.3. Here we see that whatever reservations we had about the Newport Rotator going in discrete steps were more or less undeserved. The output curve is smooth, and the residuals are small.

Because the data fits well with our expected curve, we have shown that the $|b_+\rangle$ mode does, indeed, rotate. But because we used the fit to determine the rotation frequency of the HWP, we don't yet know that the $|b_+\rangle$ mode rotates at twice the frequency of the HWP. A simple observation by eye, though, verifies that the motor does indeed make one revolution once every 3 seconds, matching the frequency from our fit, 0.338Hz. Now because the observed frequency matches the result from the fit, we can conclude that the $|b_+\rangle$ mode rotates at twice the frequency of the HWP, or 0.676Hz.

None of this has yet shown that the $|b_+\rangle$ mode rotates right-handedly, however. To make this measurement, we should rotate the linear polar-

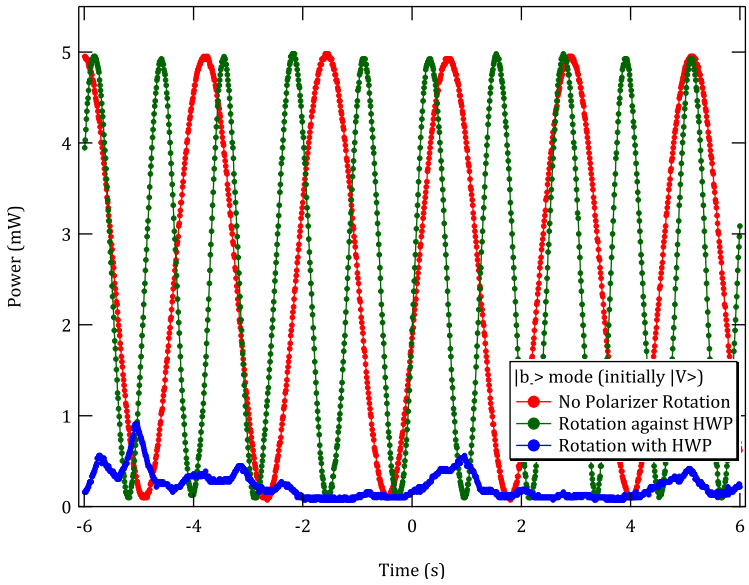

Figure 5.9 Power data for $|b_-\rangle$ mode, with HWP in Newport Rotator rotating at ~ 0.112Hz. The linear polarizer was stationary (red), rotated right-handedly (blue), and rotated left-handedly (green). Linear polarizer was rotated by hand near the target frequency of 0.224Hz. Red and green curves are fitted to $\sin^2$, giving frequencies 0.225Hz (red) and 0.410Hz (green).

izer both left and right-handedly, at twice the frequency of the HWP. Thus if the linear polarizer rotates in the same direction as the $|b_+\rangle$ mode, the resultant power should not vary with time. If the linear polarizer rotates against the $|b_+\rangle$ mode, then the resultant power should modulate at twice the frequency of the $|b_+\rangle$ mode, and four times the rotation frequency of the HWP.

Ideally, we would like to put the polarizer in a rotation mount, but our two rotation mounts (Newport and Stovall) operate in frequency ranges that do not overlap at all. The Newport Rotator can go up to 1Hz, while the Stovall Rotator, as we will see below, does not rotate smoothly below 3Hz. Thus we could not use two Rotators, so I put the HWP into the Newport Rotator and rotated the polarizer by hand. Because I had to maintain this rotation at twice the frequency of the HWP, I chose to use the lowest frequency we were working with. I set the Newport Rotator at 50 full-steps per second, corresponding to 0.112Hz. Thus I tried to rotate the polarizer at 0.224Hz.

Figure 5.8 shows the power data for the $|b_+\rangle$ mode, a HWP frequency of 0.112Hz, and a target frequency of 0.224Hz for the linear polarizer. We first kept the polarizer stationary (red curve) and fit the data to Equation 5.9, obtaining a HWP rotation frequency 0.112Hz. We see that the oscillations in the blue curve are significantly reduced in amplitude and appear close to our expected flat line. This was when the polarizer was rotated right-handedly, in the same direction as the HWP. This curve has magnitude that is close to the maximum, showing that I rotated the polarizer such that its axis was parallel to the $|b_+\rangle$ polarization vector. The green curve, where the polarizer was rotated against the rotation of the HWP, has about twice the frequency of the stationary polarizer data set, at 0.425Hz. These results show that the $|b_+\rangle$ mode does, indeed, rotate right-handedly.

Next, we do the same thing with the $|b_-\rangle$ mode. Recall from our simulations in Section 4.3 that this mode rotates right-handedly as well. Figure 5.9 shows the results from our rotating polarizer experiment. The red curve, where the polarizer was stationary, gave a HWP frequency of 0.112Hz. As expected, the blue curve, corresponding to right-handed polarizer rotation, is almost completely diminished. Here, the magnitude is low because I rotated the polarizer such that its axis was perpendicular to the $|b_-\rangle$ polarization vector. On the other hand, the green curve, corresponding to left-handed polarizer rotation, has twice the frequency of the red curve. These results show that the $|b_-\rangle$ mode, too, rotates right-handedly.

5.3.2 Calibrating the Stovall Rotator

As mentioned above, the Stovall Rotator has a motor controlled by a dial with arbitrary numbers representing some amount of current fed into the motor. However, this may or may not correspond linearly with the rotation frequency of the HWP within the rotation mount. To best check this, we take data following the same procedure we used to create Figure 5.7, but for dial values ranging from 5 to 50 in increments of 2.5. We note that the dial has values ranging from 0 to 100, but the HWP seems to rotate dangerously beyond 50 so here we don't go beyond dial values greater than 50.

Figures 5.10 and 5.11 show data for the Stovall Rotator at motor dial values of 5 and 50, respectively. The data are fit to Equation 5.9, and the resultant frequencies are listed in the captions of the figures. First, we note that Figure 5.10 simply does not fit well. At low dial values (< 10), the HWP does not rotate smoothly, generating data that varies in amplitude and frequency. Second, we notice that the data for the dial value of 50 has a much higher frequency and a much smaller amplitude than the data for

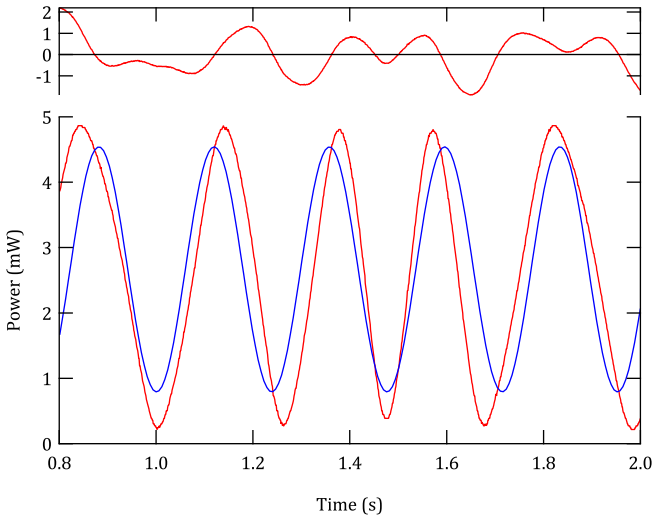

Figure 5.10 Power measured from the $|b_+\rangle$ mode with the HWP inside the Stovall Rotator, rotating at 1.05Hz (motor dial value of 5). The fit used to determine this frequency is shown in blue, described by Equation 5.9, with residuals above. The Stovall Rotator does not produce smooth rotation at low frequencies, as shown here by the poor fit.

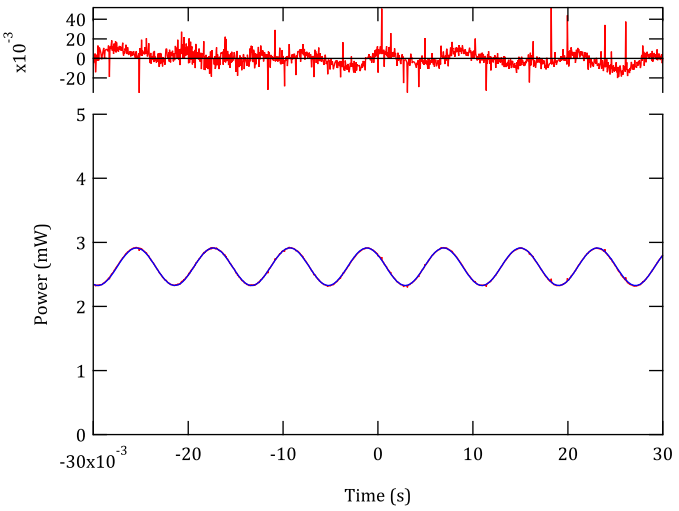

Figure 5.11 Power measured from the $|b_+\rangle$ mode with the HWP inside the Stovall Rotator, rotating at 30.9Hz (motor dial value of 50). The fit used to determine this frequency is shown in blue, described by Equation 5.9. Residuals are plotted above.

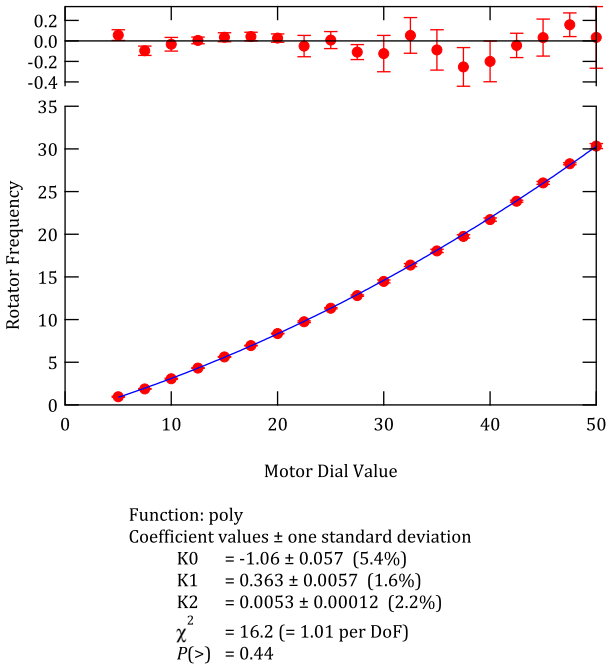

Figure 5.12 Data like in Figures 5.7, 5.10, and 5.11 were taken five times at each dial value, then fitted to obtain the rotation frequency of the HWP. Frequency of HWP is plotted against the dial value used. The data does not fit a line well, but it fits a polynomial function $K0 + K1 * (\text{dial}) + K2 * (\text{dial})^2$ relatively well, as shown above.

low dial values. The higher frequency is obvious: with higher dial values, the Stovall motor spins faster. However, the lower amplitude is concerning. Not only that, but the power seems to be converging on a single value as the frequency increases. We will return to this in Section 5.3.3.

We took data at each dial value, fit the data, and extracted the frequency of the fit. We repeated this five times and averaged to get good statistics and a measure of the error. Our results are shown in Figure 5.12. We tried fitting this data to a linear fit, but the residuals ranged as high as 2mW. Here, we show a quadratic fit that fits very well. We can use this fit when calculating the frequency at any value of the motor dial from 5 to 50.

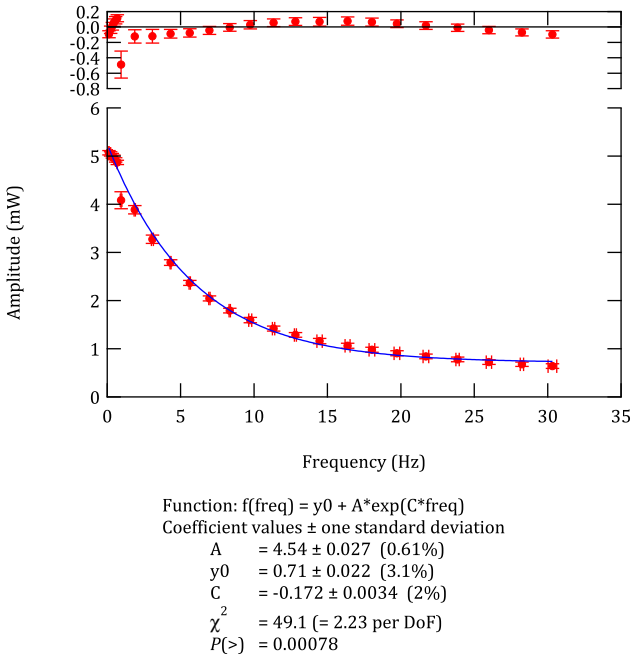

Figure 5.13 Data like in Figures 5.7, 5.10, and 5.11 were taken five times at each frequency, then fitted. Amplitude of fit is plotted against corresponding HWP frequency. Exponential fit shown in blue, fit equation is shown under the graph, and residuals are plotted above.

5.3.3 Amplitude Variation vs. Frequency

The difference in the amplitude of the curves in Figures 5.10 and 5.11 is almost certainly an artifact of our data acquisition system. It has not prevented us from performing meaningful measurements of slowly rotating light so far, but we would certainly like to eliminate this glitch in the future. Using the same data that we used to produce Figure 5.12, we took the amplitude and frequency from each fit of each curve, and plotted it. These results are shown in Figure 5.13.

To supplement the data from our Stovall Rotator, in this figure we have included six data points using the Newport Rotator (50 full-steps/s to 300 full-steps/s). These points seem to fall along a decaying exponential curve, so we fit the data to an exponential. However, this doesn't give much in the way of a physical explanation of the amplitude decrease.

From Figures 5.10 and 5.11, we see that the amplitude decreases, but it

does so by converging on a single value near 2.7mW. This seems to suggest some sort of time-averaging effect in our system for acquiring optical power measurements. The fact that this averaging occurs even over such long timescales ($\sim$ 0.1s) points to a design choice in software rather than a hardware limitation of our devices themselves.

The bandwidth limitations are clearly imposed within the power meter unit, and are present in the jagged data we obtain from the power meter itself. Figures 5.14 and 5.15 show data taken with the power meter software when the HWP rotates at 3.1Hz and 11.3Hz (dial values of 10 and 25), respectively. Looking past the poor quality of the data, we see a similar amplitude trend as in Figures 5.10 and 5.11. The curve in Figure 5.14 ranges from 1mW to 4mW, while the curve in Figure 5.15 ranges between 1.7mW and 3.2mW. Clearly, the amplitude decreases as the frequency increases in data from both the power meter and the oscilloscope. It is frustrating that the bandwidth-limiting effects carry over from the power meter to the analog out, though the analog out signal does not suffer from the sampling effects causing jagged data. Future work could be done to determine an alternate measurement scheme that bypasses this issue.

In this chapter, we have introduced the experimental setup necessary to generate the $|b_{\pm}\rangle$ modes in the lab. We then showed improvements we made specific to our lab and experimental setup that resolved the discrete nature of the data that Susanna observed. Finally, we presented experimental data showing that both of the spin equal superposition states $|b_{\pm}\rangle$ rotate in the same direction, and at twice the frequency of rotation of the HWP. We also presented, but did not resolve, an interesting issue about the amplitude of the measured curve dropping off with higher frequency.

This was the extent of our experimental work this year. However, we spent some time trying to expand into generating the OAM equal superposition states, $|c_{\pm}\rangle$. In the next chapter, we will outline how one could go about doing this.

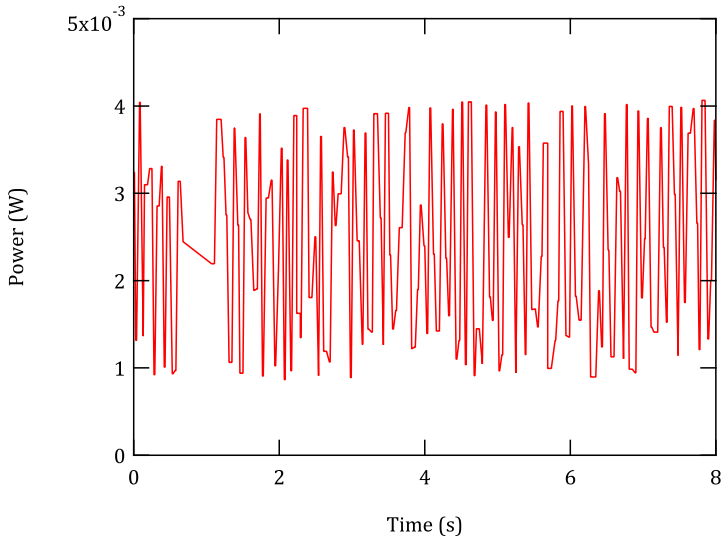

Figure 5.14 Data measured via power meter software, looking at the $|b_+\rangle$ mode with the HWP inside the Stovall Rotator rotating at 3.1Hz (motor dial value of 10).

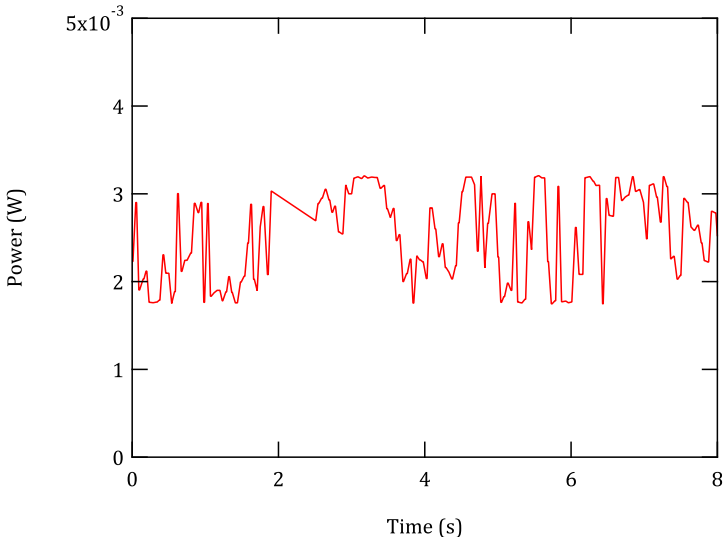

Figure 5.15 Data measured via power meter software, looking at the $|b_+\rangle$ mode with the HWP inside the Stovall Rotator rotating at 11.3Hz (motor dial value of 25).

Chapter 6

Future OAM Work

Our work in Chapter 5 has dealt with the generation and detection of the spin equal superpositions $|b_{\pm}\rangle$. We have mentioned before that we were limited to these superpositions because we did not obtain the equipment necessary for the generation and detection of the OAM superpositions $|c_{\pm}\rangle$. Here in this chapter we will outline the steps necessary to create and measure the $|c_{\pm}\rangle$ modes.

As with our treatment of the $|b_{\pm}\rangle$ modes, here we can divide this experimental setup into three parts:

1. Generation of initial OAM superpositions $HG_{0,1}$ and $HG_{1,0}$
2. Generation of slowly rotating light $|c_{\pm}\rangle$
3. Measurement of slowly rotating light $|c_{\pm}\rangle$

6.1 Generation of initial OAM superpositions

In the spin superposition case, the first step was given to us by the laser. Recall that our Helium-Neon laser outputs horizontally polarized light, which is simply an equal superposition of light with $s = 1$ and $s = -1$. We used this initial spin superposition to generate our $|b_{+}\rangle$ mode. Similarly, we argued that an initial state of vertically polarized light could generate the $|b_{-}\rangle$ mode. Vertically polarized light can easily be generated by sending horizontally polarized light through a half-wave plate oriented at 45° from the

horizontal. Using our notation $|\omega, \ell, s\rangle$, these initial states can be written as

$$|H\rangle = \frac{1}{\sqrt{2}}|\omega, \ell, 1\rangle + \frac{1}{\sqrt{2}}|\omega, \ell, -1\rangle \tag{6.1}$$

$$|V\rangle = \frac{1}{\sqrt{2}}|\omega, \ell, 1\rangle - \frac{1}{\sqrt{2}}|\omega, \ell, -1\rangle \tag{6.2}$$

where we have let $\ell = 0$ in order to focus solely on spin angular momentum. These states eventually become the spin equal superpositions

$$|b_+\rangle = \frac{1}{\sqrt{2}}|\omega + \Omega, \ell, 1\rangle + \frac{1}{\sqrt{2}}|\omega - \Omega, \ell, -1\rangle \tag{6.3}$$

$$|b_-\rangle = \frac{1}{\sqrt{2}}|\omega + \Omega, \ell, 1\rangle - \frac{1}{\sqrt{2}}|\omega - \Omega, \ell, -1\rangle. \tag{6.4}$$

Similarly, we want to make equal superpositions of OAM states carrying ℓ and $-\ell$. In other words, we want to create

$$|\psi\rangle = \frac{1}{\sqrt{2}}|\omega, \ell, 0\rangle + \frac{1}{\sqrt{2}}|\omega, -\ell, 0\rangle \tag{6.5}$$

$$|\psi_\perp\rangle = \frac{1}{\sqrt{2}}|\omega, \ell, 0\rangle - \frac{1}{\sqrt{2}}|\omega, -\ell, 0\rangle \tag{6.6}$$

where we have set $s = 0$ to eliminate any spin angular momentum effects and focus solely on OAM. These states, we will show below, can be made into our slowly rotating modes

$$|c_+\rangle = \frac{1}{\sqrt{2}}|\omega + \ell\Omega, \ell, 0\rangle + \frac{1}{\sqrt{2}}|\omega - \ell\Omega, -\ell, 0\rangle \tag{6.7}$$

$$|c_-\rangle = \frac{1}{\sqrt{2}}|\omega + \ell\Omega, \ell, 0\rangle - \frac{1}{\sqrt{2}}|\omega - \ell\Omega, -\ell, 0\rangle. \tag{6.8}$$

Just as $|\omega, 0, 1\rangle$ is described by right circularly polarized light, the state $|\omega, \ell, 0\rangle$ is described by the Laguerre-Gaussian (LG) mode LG_p^ℓ, where p is the radial order, denoting the number of radial nodes for $r > 0$. Furthermore, the equal superposition of two LG modes is described by Hermite-Gaussian (HG) modes $\mathrm{HG}_{m,n}$, where m and n denote the number of nodes in the horizontal and vertical directions, respectively. [14, 15] These HG and LG modes are OAM carrying Gaussian beams, and their electric fields are variants on the expression we introduced in Equation 2.7. The Gaussian beam expressed there was the solution to the wave equation under the

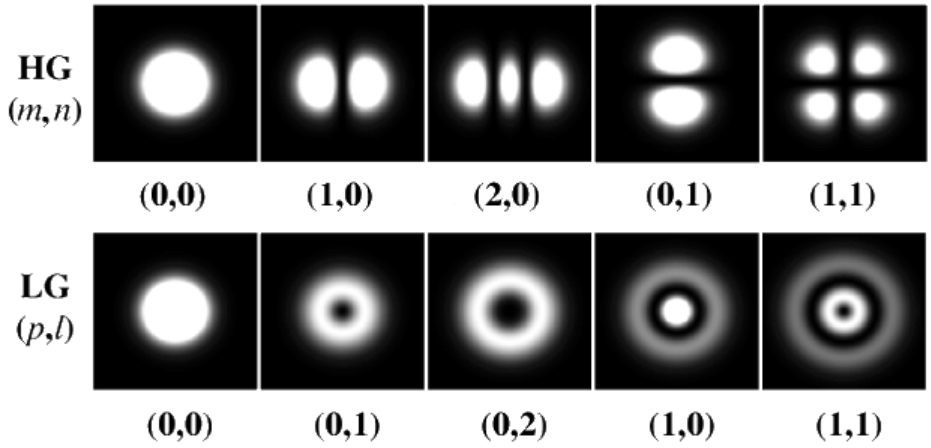

Figure 6.1 Time-averaged transverse intensity profiles of Gaussian modes. Top: Hermite-Gaussian modes labeled by (m, n). Bottom: Laguerre-Gaussian modes labeled by (ℓ, p). Adapted from [13].

paraxial approximation in cylindrical coordinates.[1] LG modes are also solutions to the paraxial wave equation in cylindrical coordinates, but they take into account OAM as well. HG modes are solutions to the paraxial wave equation in Cartesian coordinates.

Figure 6.1 shows the transverse intensity profiles of selected HG and LG modes. We note that our laser output can be described in both of these conventions as LG_0^0 and $\mathrm{HG}_{0,0}$. Furthermore, the LG_0^1 mode shown here is the same as that shown in Figure 2.4.

Here we have introduced a lot of notation and terminology, but for our purposes we can simply consider the lowest order of OAM ($\ell = 1$). Then, we rewrite our initial OAM superpositions as

$$\mathrm{HG}_{1,0} = \frac{1}{\sqrt{2}}\mathrm{LG}_0^1 + \frac{1}{\sqrt{2}}\mathrm{LG}_0^{-1} \tag{6.9}$$

$$= \frac{1}{\sqrt{2}}|\omega, 1, 0\rangle + \frac{1}{\sqrt{2}}|\omega, -1, 0\rangle \tag{6.10}$$

$$\mathrm{HG}_{0,1} = \frac{1}{\sqrt{2}}\mathrm{LG}_0^1 - \frac{1}{\sqrt{2}}\mathrm{LG}_0^{-1} \tag{6.11}$$

$$= \frac{1}{\sqrt{2}}|\omega, 1, 0\rangle - \frac{1}{\sqrt{2}}|\omega, -1, 0\rangle. \tag{6.12}$$

[1] Recall that the paraxial approximation holds when the divergence of the beam is small.

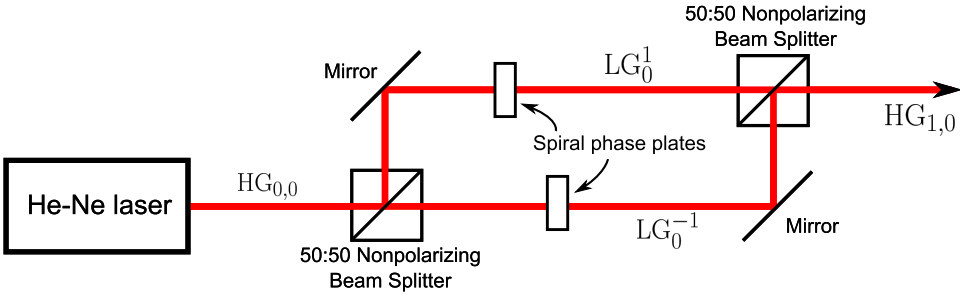

Figure 6.2 The schematic for a possible experiment to generate $HG_{1,0}$ and $HG_{0,1}$ by generating two separate $LG_0^{\pm 1}$ beams and interfering them.

In other words, we need an incident $HG_{1,0}$ to produce $|c_+\rangle$ and an incident $HG_{0,1}$ to produce $|c_-\rangle$. These HG modes can be put through a rotating Dove prism to generate the $|c_\pm\rangle$ modes, as we will cover in Section 6.2.

Over the course of this year, we have considered four possible methods to generate these modes from our base laser mode $HG_{0,0}$:

1. Build an open cavity laser with output $HG_{1,0}$ or $HG_{0,1}$.
2. Combine $LG_0^{\pm 1}$ modes with an interferometer.
3. Use a Spatial Light Modulator.
4. Use a few-mode fiber.

First, we can simply build an open cavity laser and set the cavity slightly off resonance such that the output light is directly $HG_{1,0}$ or $HG_{0,1}$. We did not consider this option very heavily, as we did not want to build a separate laser for this project.

Second, we can generate the two $LG_0^{\pm 1}$ modes separately, and then combine them with an interferometer. We can generate the LG modes by sending in our input beam though spiral phase plates. A phase plate gives a phase shift that scales with the azimuthal angle ϕ so that when properly tuned, the plate shifts the OAM of an incident beam by $\Delta\ell = \pm 1$. The schematic of a possible experimental setup for this conversion is shown in Figure 6.2. The incident beam in the $HG_{0,0}$ mode gets split up into two paths of equal intensity. One path goes through a spiral phase plate to turn it into LG_0^1 while the other path turns into LG_0^{-1}. Then, these are recombined and form the $HG_{1,0}$ mode if there is no phase difference. If we tune the path lengths of the two arms such that there is a π phase difference, then we produce the $HG_{0,1}$ mode.

This setup does not seem experimentally challenging, but we did not purchase or make the spiral phase plates necessary to implement it. Sasada and Okamoto performed a similar technique in [16], so there is some precedent for this experiment and it may be worth trying in the future.

Third, we can buy a spatial light modulator (SLM) and place a diffraction pattern on its surface that takes an incident $HG_{0,0}$ and outputs $HG_{1,0}$ or $HG_{0,1}$. This diffraction pattern is simply the interference pattern between the desired output state and the input $HG_{0,0}$, and the SLM acts as a hologram, producing the desired state by the principle of holography. Buying an SLM would also further our lab's research in entangling photons in OAM, a project in which we are using homemade glass holograms that achieve the same effect as an SLM. Maurer et al. describe an experimental setup to generate an arbitrary HG or LG mode in [14].

This SLM would need to work in the wavelength regime of this thesis (633nm) and our entanglement research (810nm). Furthermore, we would like the SLM to produce a full 2π phase shift range in order to produce the desired output state with high purity. We investigated SLMs that satisfy these criteria, and found one by Holoeye called the "LETO Phase Only SLM." This SLM has 1920×1080 pixel resolution and exhibits a phase shift of 2π for wavelengths up to 850nm. However, Holoeye gave us a quote for $\$17,100$, which is far outside our price range.

An alternative would be to buy and use a cheaper, lower quality SLM. Cambridge Correlators sells a 1024×768 pixel resolution SLM for \$1200, but it has a phase shift range that goes up to only 0.8π, resulting in a loss in diffraction efficiency. Bowman and Padgett describe a method to improve the results using this SLM in [17], which may be worth looking into.

Fourth, we can use a few-mode optical fiber which takes in our input beam, perhaps at some other linear polarization. Then, the modes allowed by the fiber shape this input beam into our desired HG beam. The exact details of this procedure are not very well explained in the literature, but the results of [18] show that various superpositions of $HG_{1,0}$ and $HG_{0,1}$ can be made using this technique. Other papers have also come to this result. [15] used a three-mode fiber to convert LG modes to HG modes, which can be run backwards to generate HG modes from LG modes, and [19] created $HG_{1,0}$ and $HG_{0,1}$ beams using a two-mode fiber. Although the experimental setups used in these papers are not complicated, this is likely quite challenging due to the need to couple light into a few-mode fiber. Furthermore, the modes made using this technique have rather questionable quality/purity. However, few-mode fibers are relatively cheap.

Thus we have outlined four different methods of producing the first-

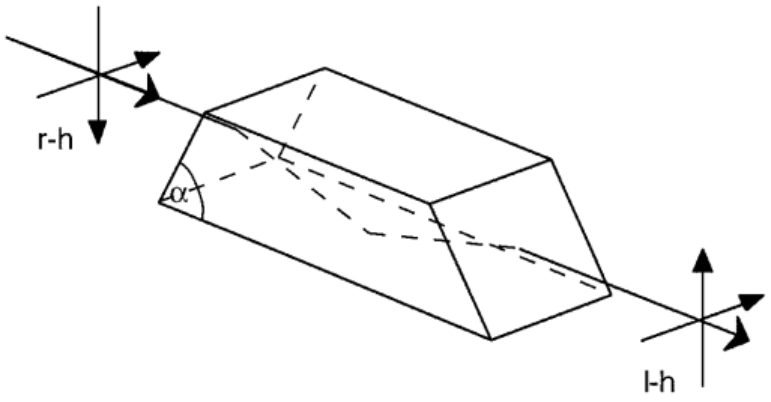

Figure 6.3 A Dove Prism flipping an input image. Taken from [20].

order Hermite-Gaussian modes $HG_{1,0}$ and $HG_{0,1}$ we need as the initial states in producing the slowly rotating modes $|c_{\pm}\rangle$. Using an SLM would likely be the easiest method, but the price is simply too high. Constructing an open cavity laser would be a significant amount of work for relatively little payoff, though it is a viable option. Few-mode optical fibers can also generate our desired modes, but the resultant modes may be of poor purity. Finally, building an interferometer setup would be rather easy experimentally, but we did not obtain the spiral phase plates required for such a setup.

6.2 Generation of $|c_{\pm}\rangle$ Modes

In the case of the spin superpositions, we proved that sending horizontally or vertically polarized light into a rotating HWP produced $|b_+\rangle$ or $|b_-\rangle$, respectively. Similarly for the OAM case, we can use a rotating Dove prism to convert incident $HG_{1,0}$ and $HG_{0,1}$ modes into $|c_+\rangle$ and $|c_-\rangle$, respectively.

Figure 6.3 shows the function of a Dove prism. The incident image comes into one face of the Dove prism and refracts downward to the bottom surface. Here, it experiences total internal reflection, flipping its vertical component from down to up. Then, it refracts and continues propagating outward, having experienced a flip about the horizontal axis. We can thus define the action of a Dove prism as flipping an input transverse amplitude pattern across its axis (which is horizontal here). This is analogous to a HWP flipping an input polarization across its axis for spin angular momentum.

We will not go through the derivation here, but the action of a rotating Dove prism for OAM is also analogous to the action of a rotating HWP for spin. In the case of spin, we saw that a HWP rotating right-handedly caused an input right circularly polarized beam into a left circularly polarized beam with a lower frequency. Similarly, if we let the Dove prism rotate right-handedly, then an input LG_0^1 beam ($\ell = 1$) will turn into an output LG_0^{-1} beam ($\ell = -1$) with lower frequency. Similarly, an incident LG_0^{-1} beam becomes a LG_0^1 beam at the output, with higher frequency.

Because the $HG_{1,0}$ and $HG_{0,1}$ modes are equal superpositions of LG modes with angular momenta of opposite sign, sending them through this rotating Dove prism would frequency shift up the positive OAM component and frequency shift down the negative OAM component. This results in the $|c_+\rangle$ and $|c_-\rangle$ modes, respectively.

Furthermore, we note that just as in the HWP and spin case, the state output from the Dove prism rotates at twice the frequency of the rotation of the Dove prism. [17].

6.3 Detection and Measurement of $|c_\pm\rangle$ Modes

Now that we have shown how to generate the OAM equal superpositions $|c_\pm\rangle$, our goal now is to somehow detect/measure their rotation. From our modeling of the $|c_\pm\rangle$ modes in Section 4.6, we saw that the field amplitude distribution has two lobes that rotate right-handedly at Ω. The radial distance scale in our modeling was determined by the properties of the Bessel function. However, in the lab, and in this chapter we use the Gaussian formalism. Here, the radial distance scale is limited by the beam waist of the input Gaussian beam.

Our Si photodiode sensor takes in a beam on a circular area that is about 1cm in diameter - far too large for our beam. We need to get a smaller aperture to take in power on one side of the field amplitude distribution. In my previous work in the lab (Summer 2011, see [21]), I used a setup similar to Figure 6.4 to acquire beam power profiles. Here, I stuck a thumbtack through a piece of duct tape to make a pinhole, and then placed it in front of the Si sensor to make a much smaller aperture. Previous beam profile measurements of the laser output, collected by translating the Si sensor across the beam, showed that the full width at half maximum of the beam was around 0.6mm. However, we need only make a pinhole that is relatively small and can measure power on one side of the singularity at $r = 0$. The exact dimensions we have not calculated.

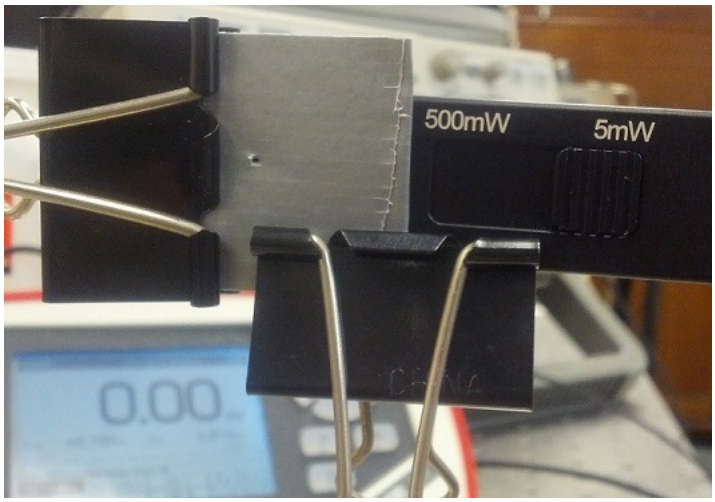

Figure 6.4 Apparatus that can be used to measure the rotation of the $|c_{\pm}\rangle$ modes. A piece of duct tape covers the entire Si sensor detection area except for one small pinhole.

Thus, in this chapter we have presented a complete procedure to create and measure the $|c_{\pm}\rangle$ modes. Using our spin angular momentum procedure as reference, we explained how to generate the initial states $HG_{1,0}$ and $HG_{0,1}$ from our laser output $HG0,0$. Then, we argued that a rotating Dove prism could generate the slowly rotating modes $|c_{\pm}\rangle$ from these initial Hermite-Gaussian modes. Finally, we outlined a procedure to measure these slowly rotating modes. This procedure appears quite challenging experimentally, so there is definitely room for future work.

Chapter 7

Conclusion

In this thesis, I have investigated slowly rotating modes of light that rotate in one direction, but may carry angular momentum that implies rotation in another direction. Others rotate according to the angular momentum, and even others rotate without angular momentum.

Using van Enk and Nienhuis as reference, I first redid the theory work of Susanna Todaro (HMC '12). Instead of using two different techniques to examine the spin and OAM superpositions separately, I used the simple method of taking the real part of the complex electric field for all of the modes, as shown in Chapter 3. This got rid of the minor errors in the old simulations, producing simulations exhibiting striking similarities between the spin and OAM superpositions. The key to our enhanced understanding was to deliberately look at both the fast and slow rotations, while Susanna's approach ignored the fast rotation component.

The simulations in Chapter 4 showed that the negatively indexed frequency dependent modes $|g_-\rangle$ and $|h_-\rangle$ rotate right-handedly, matching their angular momentum. However, they exhibit amplitude and frequency modulation: the frequency drops when the amplitude is high, and vice versa. I didn't explain this behavior intuitively, but I did track the maximum and minimum of this modulation for both amplitude and frequency.

The positively indexed modes $|g_+\rangle$ and $|h_+\rangle$ were found to also rotate right-handedly. However, they carry negative angular momentum opposing this direction of rotation. I found that in my derivation of the real electric field, I was able to retain a $\cos(\omega t)$ term that modulated the amplitude of these two positive index modes at the frequency ω. When examining only when the field amplitude was maximized, this amplitude modulation at ω made it seem like there was a component of left-handed rota-

tion. From here, I conjectured that this left-handed rotation component could contribute more negative angular momentum than the positive angular momentum contribution from the right-handed rotation at Ω. This would produce an overall negative value for angular momentum, which is what I calculated in Chapter 3. This intuition-based explanation of the angular momentum paradox is quite shaky. Future work could be done to make this argument truly quantitative.

The simulations also showed that the equal superposition states $|b_\pm\rangle$ and $|c_\pm\rangle$ rotate right-handedly while carrying zero angular momentum. Because the $|b_+\rangle$ and $|c_+\rangle$ modes are just the experimental limit ($\omega \gg \Omega$) of the $|g_+\rangle$ and $|h_+\rangle$ modes, they should exhibit similar behavior. Furthermore, drawing from van Enk and Nienhuis, I argued that the plus and minus modes are separated by just a phase shift. Thus, all of the experimental modes should share similar features with the $|g_+\rangle$ and $|h_+\rangle$ modes. In particular, they should exhibit some left-handed rotation component. But taken to the experimental limit, this left-handed rotation from amplitude modulation at ω simply balances out with the right-handed rotation at Ω. Then, the resultant angular momentum would be zero, which is what we observe. Again, this argument lacks quantitative results, which could be the subject for further study.

In Chapters 5 and 6, I described the experimental setup for generating and measuring both the spin and OAM equal superpositions. While I was unable to move on to OAM this year, I did investigate several possibilities for doing so in future endeavours. I did, however, overcome several experimental challenges to creating the spin superpositions $|b_\pm\rangle$. Figures 5.8 and 5.9 show data proving that both of the $|b_\pm\rangle$ modes rotate right-handedly at twice the frequency of the HWP used to generate them. Thus, they are indeed just a phase shift from each other.

In summary, I have developed new theory and corresponding simulations that match experimental results, and previous work in the field by van Enk and Nienhuis. Future work could focus on either theory, experiment, or both. My explanations for the angular momentum paradox are shaky and require numbers, or more obvious proof. On the experimental side, I have not even begun building an experimental setup to generate and measure the OAM superpositions $|c_\pm\rangle$. Even if that is done, future work on more exotic slowly rotating modes of light could be done. What about superpositions of modes that carry opposing signs of both spin and orbital angular momentum? What about the same sign? van Enk and Nienhuis introduce many modes that this thesis does not cover, but may be interesting to investigate.

Appendix A

Mathematica Code

```
(* base electric field *)
kT=1;
BaseE[CC_,r_,m_,\[Omega]_]:=CC Sqrt[\[Omega]]
                            BesselJ[Abs[m],kT*r];
CosTh[\[Omega]_,\[CapitalOmega]_]:=
    Sqrt[(\[Omega]+\[CapitalOmega])/(2 \[Omega])];
SinTh[\[Omega]_,\[CapitalOmega]_]:=
    Sqrt[(\[Omega]-\[CapitalOmega])/(2 \[Omega])];

Manipulate[
    ParametricPlot3D[
        {r*Cos[\[Theta]],r*Sin[\[Theta]],
        BaseE[scale,r,ll,1]},{r,0,range},{\[Theta],0,2*\[Pi]},
        PlotRange->All,Axes->False],
    {{scale,7},1,10},{{range,14},5,20},{ll,0,5}]

Manipulate[
    VectorPlot[
        {BaseE[scale,Sqrt[x^2+y^2],ll,1],0},
        {x,-range,range},{y,-range,range}, PlotRange->
        {{-range,range},{-range,range}},FrameTicks->None],
    {{scale,7},1,10},{{range,14},5,20},{ll,0,5}]

(* g+ mode *)
Egplusx[CC_,x_,y_,\[Omega]_,\[CapitalOmega]_,t_]:=
    BaseE[CC,Sqrt[x^2+y^2],0,\[Omega]]Cos[\[Omega] t]
    2 CosTh[\[Omega],\[CapitalOmega]]
    SinTh[\[Omega],\[CapitalOmega]]
    Cos[\[CapitalOmega] t];
Egplusy[CC_,x_,y_,\[Omega]_,\[CapitalOmega]_,t_]:=
```

```
    BaseE[CC,Sqrt[x^2+y^2],0,\[Omega]]Cos[\[Omega] t]
    2 CosTh[\[Omega],\[CapitalOmega]]
    SinTh[\[Omega],\[CapitalOmega]]
    Sin[\[CapitalOmega] t];

Manipulate[
    VectorPlot[
        {Egplusx[2,x,y,\[Omega],\[CapitalOmega],t],
        Egplusy[2,x,y,\[Omega],\[CapitalOmega],t]},
        {x,-range,range},{y,-range,range},
        VectorScale->{0.13/Sqrt[\[Omega]]
        Sqrt[(Egplusx[1,0,0,\[Omega],\[CapitalOmega],t])^2
        +(Egplusy[1,0,0,\[Omega],\[CapitalOmega],t])^2]},
        PlotRange->{{-range,range},{-range,range}}],
    {{range,2.5},0.1,10},{{\[Omega],2},0,20},
    {{\[CapitalOmega],1},0,5},{t,0,2*\[Pi]}]

(* g- mode *)
Egminusx[CC_,x_,y_,\[Omega]_,\[CapitalOmega]_,t_]:=
    BaseE[CC,Sqrt[x^2+y^2],0,\[Omega]](Cos[\[Omega] t]
    \[CapitalOmega]/\[Omega] Cos[\[CapitalOmega] t]
    -Sin[\[Omega] t]Sin[\[CapitalOmega] t]);
Egminusy[CC_,x_,y_,\[Omega]_,\[CapitalOmega]_,t_]:=
    BaseE[CC,Sqrt[x^2+y^2],0,\[Omega]](Cos[\[Omega] t]
    \[CapitalOmega]/\[Omega] Sin[\[CapitalOmega] t]
    +Sin[\[Omega] t]Cos[\[CapitalOmega] t]);


Manipulate[
    VectorPlot[
        {Egminusx[1,x,y,\[Omega],\[CapitalOmega],t],
        Egminusy[1,x,y,\[Omega],\[CapitalOmega],t]},
        {x,-range,range},{y,-range,range},
        VectorScale->{0.12/Sqrt[\[Omega]]
        Sqrt[(Egminusx[1,0,0,\[Omega],\[CapitalOmega],t])^2
        +(Egminusy[1,0,0,\[Omega],\[CapitalOmega],t])^2]},
        PlotRange->{{-range,range},{-range,range}}],
    {{range,2.5},0.1,4},{{\[Omega],2},0,20},
    {{\[CapitalOmega],1},0,5},{t,0,2*\[Pi]}]

(* get amplitude vs. angular velocity plot *)
omega=2;
OMEGA=1;
norm[t_]:=Sqrt[(Egminusx[1,0,0,omega,OMEGA,t])^2
             +(Egminusy[1,0,0,omega,OMEGA,t])^2];
```

```
angleM[t_]:=ArcTan[Egminusy[1,0,0,omega,OMEGA,t]
                   /Egminusx[1,0,0,omega,OMEGA,t]];
Plot[{norm[t],angleM'[t]},{t,0,(4\[Pi])/omega},
    AxesLabel->{Style["t",30],None},PlotRange->{0,5.1},
    PlotLegends->Placed[{"amplitude","angular frequency"},
                        {0.14,0.75}]]

(* b+ mode *)
Ebplusx[CC_,x_,y_,\[Omega]_,\[CapitalOmega]_,t_]:=
    BaseE[CC,Sqrt[x^2+y^2],0,\[Omega]]Cos[\[Omega] t]
    Cos[\[CapitalOmega] t];
Ebplusy[CC_,x_,y_,\[Omega]_,\[CapitalOmega]_,t_]:=
    BaseE[CC,Sqrt[x^2+y^2],0,\[Omega]]Cos[\[Omega] t]
    Sin[\[CapitalOmega] t];

Manipulate[
    VectorPlot[
        {Ebplusx[2,x,y,\[Omega],\[CapitalOmega],t],
        Ebplusy[2,x,y,\[Omega],\[CapitalOmega],t]},
        {x,-range,range},{y,-range,range},
        VectorScale->{0.1/Sqrt[\[Omega]]
        Sqrt[(Ebplusx[1,0,0,\[Omega],\[CapitalOmega],t])^2
        +(Ebplusy[1,0,0,\[Omega],\[CapitalOmega],t])^2]},
        PlotRange->{{-range,range},{-range,range}}],
    {{range,2.5},0.1,4},{{\[Omega],20},10,50},
    {{\[CapitalOmega],1},0,5},{t,0,2*\[Pi]}]

(* b- mode *)
Ebminusx[CC_,x_,y_,\[Omega]_,\[CapitalOmega]_,t_]:=
    -BaseE[CC,Sqrt[x^2+y^2],0,\[Omega]]Sin[\[Omega] t]
    Sin[\[CapitalOmega] t];
Ebminusy[CC_,x_,y_,\[Omega]_,\[CapitalOmega]_,t_]:=
    BaseE[CC,Sqrt[x^2+y^2],0,\[Omega]]Sin[\[Omega] t]
    Cos[\[CapitalOmega] t];

Manipulate[
    VectorPlot[
        {Ebminusx[1,x,y,\[Omega],\[CapitalOmega],t],
        Ebminusy[1,x,y,\[Omega],\[CapitalOmega],t]},
        {x,-range,range},{y,-range,range},
        VectorScale->{0.1/Sqrt[\[Omega]]
        Sqrt[(Ebminusx[1,0,0,\[Omega],\[CapitalOmega],t])^2
        +(Ebminusy[1,0,0,\[Omega],\[CapitalOmega],t])^2]},
        PlotRange->{{-range,range},{-range,range}}],
    {{range,2.5},0.1,4},{{\[Omega],20},10,50},
    {{\[CapitalOmega],1},0,5},{t,0.01,2*\[Pi]}]
```

```
(* h+ mode *)
EhpRphiz[CC_,r_,\[Phi]_,ell_,\[Omega]_,\[CapitalOmega]_,t_]:=
    BaseE[CC,r,ell,\[Omega]]CosTh[\[Omega],\[CapitalOmega]]
    SinTh[\[Omega],\[CapitalOmega]]Cos[\[Omega] t]
    Cos[ell(\[Phi]-\[CapitalOmega] t)];

zmax=4; (* fixes z-axis scale *)
Manipulate[
    ParametricPlot3D[
        {r*Cos[\[Phi]],r*Sin[\[Phi]],
          EhpRphiz[scale,r,\[Phi],ell,
            \[Omega],\[CapitalOmega],t]},
        {r,0,range},{\[Phi],0,2\[Pi]},
        PlotRange->{{-range,range},
          {-range,range},{-zmax,zmax}},
        AxesLabel->{Style["x",20],Style["y",20],
          Style["z",20]}],
    {{range,11},1,20},{{scale,10},1,20},{{\[Omega],2},1,20},
    {{\[CapitalOmega],1},1,10},{t,0,2*\[Pi]},{{ell,1,"m"},
    Table[i,{i,0,5}],ControlType->RadioButton}]

(* cartesian coordinates - produces a better vector plot *)
(* for cylindrical coordinates, vectors show up where it
  should be zero... so we use cartesian *)
Ehp[CC_,x_,y_,ell_,\[Omega]_,\[CapitalOmega]_,t_]:=
    BaseE[CC,Sqrt[x^2+y^2],ell,\[Omega]]
    CosTh[\[Omega],\[CapitalOmega]]
    SinTh[\[Omega],\[CapitalOmega]]
    Cos[\[Omega] t] Cos[ell(ArcTan[x,y]-\[CapitalOmega] t)];

Manipulate[
    VectorPlot[
        {Ehp[scale,x,y,ell,\[Omega],\[CapitalOmega],t],0},
        {x,-range,range},{y,-range,range},
        PlotRange->{{-range,range},{-range,range}},
        FrameTicks->None,
        VectorScale->{Abs[EhpRphiz[scale,1,\[CapitalOmega]t,
          ell,\[Omega],\[CapitalOmega],t]]}],
    {{scale,0.3},0.01,10},{{range,5},1,20},
    {{\[Omega],2},1,20},{{\[CapitalOmega],1},1,10},
    {t,0,2\[Pi]},{{ell,1,"ell"},
    Table[i,{i,0,5}],ControlType->RadioButton}]

(* h- mode *)
EhmRphiz[CC_,r_,\[Phi]_,ell_,\[Omega]_,\[CapitalOmega]_,t_]:=
```

```
    BaseE[CC,r,ell,\[Omega]]((CosTh[\[Omega],
        \[CapitalOmega]])^2*Cos[ell*\[Phi]
        -(\[Omega]+ell*\[CapitalOmega]) t]
        -(SinTh[\[Omega],\[CapitalOmega]])^2
        *Cos[ell*\[Phi]+(\[Omega]-ell*\[CapitalOmega]) t]);

zmax=4.5; (* fixes z-axis scale *)
Manipulate[
    ParametricPlot3D[
        {r*Cos[\[Phi]],r*Sin[\[Phi]],
          EhmRphiz[scale,r,\[Phi],ell,\[Omega],
            \[CapitalOmega],t]},
        {r,0,range},{\[Phi],0,2\[Pi]},
        PlotRange->{{-range,range},{-range,range},
          {-zmax,zmax}},
        AxesLabel->{Style["x",20],Style["y",20],
          Style["z",20]}],
    {{range,10},1,20},{{scale,5},1,20},{{\[Omega],2},1,20},
    {{\[CapitalOmega],1},1,10},{t,0,2*\[Pi]},{{ell,1,"m"},
    Table[i,{i,0,5}],ControlType->RadioButton}]

Ehm[CC_,x_,y_,ell_,\[Omega]_,\[CapitalOmega]_,t_]:=
    BaseE[CC,Sqrt[x^2+y^2],ell,\[Omega]]
    ((CosTh[\[Omega],\[CapitalOmega]])^2
      *Cos[ell*ArcTan[x,y]-(\[Omega]+ell*
      \[CapitalOmega])t]-(SinTh[\[Omega],\[CapitalOmega]])^2
      *Cos[ell*ArcTan[x,y]+(\[Omega]-ell*\[CapitalOmega]) t]);

Manipulate[
    VectorPlot[
        {Ehm[scale,x,y,ell,\[Omega],\[CapitalOmega],t],0},
        {x,-range,range},{y,-range,range},
        PlotRange->{{-range,range},{-range,range}},
        FrameTicks->None,
        VectorScale->{MaxValue[EhmRphiz[scale,1,\[Phi],ell,
          \[Omega],\[CapitalOmega],t],\[Phi]]}],
    {{scale,0.17},0.01,10},{{range,5},1,20},
    {{\[Omega],2},1,20},{{\[CapitalOmega],1},1,10},
    {t,0,2\[Pi]},{{ell,1,"ell"},
    Table[i,{i,0,5}],ControlType->RadioButton}]

(* c+ mode *)
EcpCy[CC_,r_,\[Phi]_,ell_,\[Omega]_,\[CapitalOmega]_,t_]:=
    BaseE[CC,r,ell,\[Omega]]Cos[\[Omega] t]
    Cos[ell(\[Phi]-\[CapitalOmega] t)];
```

```
(* parametric plot 3D*)
zmax=4; (* fixes z-axis scale *)
Manipulate[
    ParametricPlot3D[
        {r*Cos[\[Phi]],r*Sin[\[Phi]],
        EcpCy[scale,r,\[Phi],ell,\[Omega],\[CapitalOmega],t]},
        {r,0,range},{\[Phi],0,2\[Pi]},
        PlotRange->{{-range,range},{-range,range},
          {-zmax,zmax}},
        AxesLabel->{Style["x",20],Style["y",20],
          Style["z",20]}],
    {{range,10},1,20},{{scale,1},1,20},{{\[Omega],20},1,20},
    {{\[CapitalOmega],1},1,10},{t,0,2*\[Pi]},
    {{ell,1,"m"},Table[i,{i,0,5}],ControlType->RadioButton}]
(* vector plot *)
Manipulate[
    VectorPlot[
        {EcpCy[scale,Sqrt[x^2+y^2],ArcTan[x,y],ell,\[Omega],
          \[CapitalOmega],t],0},
        {x,-range,range},{y,-range,range},
        PlotRange->{{-range,range},{-range,range}},
        VectorScale->{Abs[EcpCy[scale,1.84118,\[CapitalOmega]
          t,ell,\[Omega],\[CapitalOmega],t]]}],
    {{scale,0.035},0.001,10},{{range,5},1,20},
    {{\[Omega],20},1,20},{{\[CapitalOmega],1},1,10},
    {t,0,2\[Pi]},{{ell,1,"ell"},
    Table[i,{i,0,5}],ControlType->RadioButton}]

(* c- mode *)
EcmCy[CC_,r_,\[Phi]_,ell_,\[Omega]_,\[CapitalOmega]_,t_]:=
    BaseE[CC,r,ell,\[Omega]]Sin[\[Omega] t]
    Sin[ell(\[Phi]-\[CapitalOmega] t)];

(* parametric plot 3D*)
zmax=4; (* fixes z-axis scale *)
Manipulate[
    ParametricPlot3D[
        {r*Cos[\[Phi]],r*Sin[\[Phi]],
        EcmCy[scale,r,\[Phi],ell,\[Omega],\[CapitalOmega],t]},
        {r,0,range},{\[Phi],0,2\[Pi]},
        PlotRange->{{-range,range},{-range,range},
          {-zmax,zmax}},
        AxesLabel->{Style["x",20],Style["y",20],
          Style["z",20]}],
```

```
    {{range,11},1,20},{{scale,1},1,20},{{\[Omega],20},1,20},
    {{\[CapitalOmega],1},1,10},{t,0,2*\[Pi]},{{ell,1,"m"},
    Table[i,{i,0,5}],ControlType->RadioButton}]
(* vector plot *)
Manipulate[
    VectorPlot[
        {EcmCy[scale,Sqrt[x^2+y^2],ArcTan[x,y],ell,\[Omega],
          \[CapitalOmega],t],0},
        {x,-range,range},{y,-range,range},
        PlotRange->{{-range,range},{-range,range}},
        VectorScale->{Abs[EcmCy[scale,1.84118,\[CapitalOmega]
          t+\[Pi]/2,ell,\[Omega],\[CapitalOmega],t]]}],
    {{scale,0.035},0.001,10},{{range,5},1,20},
    {{\[Omega],20},1,20},{{\[CapitalOmega],1},1,10},
    {t,0.0001,2\[Pi]},{{ell,1,"ell"},
    Table[i,{i,0,5}],ControlType->RadioButton}]
```

Bibliography

[1] S. van Enk and G. Nienhuis. Photons in polychromatic rotating modes. *Phys. Rev. A*, 76:053825, Nov 2007.

[2] S.C. Tiwari. Rotating light, the orbital angular momentum paradox and relativistic complex scalar fields. *J. Opt. A*, 11:065701, Mar 2009.

[3] Susanna Todaro. Angular momentum of slowly rotating modes of light. Senior thesis, May 2012.

[4] John Townsend. *A Modern Approach to Quantum Mechanics*. University Science Books, 2nd edition, 2012.

[5] Wikipedia. Circular polarization — wikipedia, the free encyclopedia, 2014. [Online; accessed 19-Jan-2014].

[6] Rudiger Paschotta. Gaussian beams.

[7] M. Padgett, J. Courtial, and L. Allen. Light's orbital angular momentum. *Physics Today*, 57(5):35–40, 2004.

[8] Alison M. Yao and Miles J. Padgett. Orbital angular momentum: origins, behavior and applications. *Adv. Opt. Photon.*, 3(2):161–204, Jun 2011.

[9] David Coby Spierings van der Wolk. Manipulating the orbital angular momentum of entangled photons from spontaneous parametric down-conversion. Senior thesis, May 2014.

[10] A.Y. Bekshaev, M.S. Soskin, and M.V. Vasnetsov. Angular momentum of a rotating light beam. *Opt. Comm.*, 249(4–6):313–316, May 2005.

[11] C.N. Alexeyev and M.A. Yavorsky. Angular momentum of rotating paraxial light beams. *J. Opt. A: Pure Appl. Opt*, 7(8):416–421, 2005.

[12] Gerard Nienhuis. Polychromatic and rotating beams of light. *J. Phys. B: At. Mol. Opt. Phys*, 39(15):S529–S544, 2006.

[13] Hiroyuki Sasada. Light possessing orbital angular momenta. Online, 2014.

[14] Christian Maurer, Alexander Jesacher, Severin Furhapter, Stefan Bernet, and Monika Ritsch-Marte. Tailoring of arbitrary optical vector beams. *New Journal of Physics*, 9(3):78, 2007.

[15] Henning Soller. Hg-lg mode conversion with stressed 3-mode fibers under polarization. *Open Journal of Applied Sciences*, 2:224–227, 2012.

[16] Hiroyuki Sasada and Megumi Okamoto. Transverse-mode beam splitter of a light beam and its application to quantum cryptography. *Phys. Rev. A*, 68:012323, Jul 2003.

[17] R. Bowman, V. D'Ambrosio, E. Rubino, O. Jedrkiewicz, P. Trapani, and M.J. Padgett. Optimisation of a low cost slm for diffraction efficiency and ghost order suppression. *The European Physical Journal Special Topics*, 199(1):149–158, 2011.

[18] G. Volpe and D. Petrov. Generation of cylindrical vector beams with few-mode fibers excited by laguerre-gaussian beams. *Optics Communications*, 237(1–3):89–95, 2004.

[19] Nirmal K. Viswanathan and V. V. G. Inavalli. Generation of optical vector beams using a two-mode fiber. *Opt. Lett.*, 34(8):1189–1191, Apr 2009.

[20] Miles J. Padgett and Paul J. Lesso. Dove prisms and polarized light. *J. Modern Optics*, 46(2):175–179, 1999.

[21] Fangzhao Alex An and Julien Barnabe Devin. Improving measurements of photon orbital angular momentum, 2011.

[22] Alois Mair, Alipasha Vaziri, Gregor Weihs, and Anton Zeilinger. Entanglement of the orbital angular momentum states of photons. *Nature*, 412(6844):313–316, July 2001.